3-D NUMERICAL SIMULATION OF DAM-BREAK FLOWS OVER MOVABLE BEDS

A Dissertation
Presented in partial fulfillment of requirements for the
Doctor of Philosophy
Degree
The University of Mississippi

By

REZA MARSOOLI

May 2013

UMI 3595529
Published by ProQuest LLC (2013). Copyright in the Dissertation held by the Author.

ProQuest LLC.
789 East Eisenhower Parkway
P.O. Box 1346
Ann Arbor, MI 48106 - 1346

ABSTRACT

This Ph.D. dissertation aims to develop a 3-D numerical model of dam-break flows on movable beds. Three tasks are defined to accomplish the goal of this study.

The first task is developing a 3-D hydrodynamic model to simulate dam-break flow on fixed beds with simple geometry and test the water surface tracking technique. This model solves the Reynolds-Averaged Navier-Stokes (RANS) equations using a finite-difference method on rectilinear, staggered grids. The Volume-of-Fluid (VOF) technique with SOLA-VOF advection scheme is used to capture the free surface motion. The developed model is tested using several experimental dam-break flows and the VOF technique is found to be able to effectively treat the rapidly-varying water surface boundary of dam-break flows.

As the second task of this dissertation, a 3-D finite-volume model is developed to simulate dam-break flows on irregular fixed beds. Developing this model is necessary to accomplish the major goal of this dissertation since the finite-difference model explained above, which uses the rectilinear staggered grid, is not convenient to extend to the case of irregular and movable beds and integrate with sediment transport calculations. This model solves the RANS equations using a finite-volume method on irregular hexahedral, collocated meshes and adopts the Compressive Interface Capturing Scheme for Arbitrary Meshes (CICSAM) as the VOF advection method. The model is tested by means of experimental dam-break flows on fixed beds with simple and irregular geometries.

The final task is extending the 3-D finite-volume model to a dam-break flow model applicable on movable beds. Therefore, it is integrated with a sediment transport model developed in this study. The sediment transport model solves the non-equilibrium transport equations of suspended load and bed load separately and in turn calculates the resulting bed change, based on the flow properties calculated by the hydrodynamic model. Since the time evolution of bed topography affects the hydrodynamic calculations, the model uses a moving grid technique to update the computational grid to fit on the calculated bed topography at every time step. The grid moving velocity and the computational cell volume change generated by the moving mesh are taken into consideration when the governing equations of the hydrodynamic and sediment transport models are discretized. The integrated model is tested using several experimental dam-break flows on movable beds. The calculated spatial and temporal variations of water and bed surfaces are generally in good agreement with the measured data.

Keywords: Numerical Modeling, Dam-Break Flow, Sediment Transport, Movable Bed, Moving Mesh, Water Surface Capturing, Volume of Fluid.

DEDICATION

My dissertation is dedicated to my loving parents, Parviz and Golzar, my sister, brother, and grandmothers for their endless love, support, and encouragement.

LIST OF ABBREVIATIONS

ABBREVIATION	DEFINITION
BFD	Box Finite Difference
CDG	Characteristic Dissipative Galerkin
CICSAM	Compressive Interface Capturing Scheme for Arbitrary Meshes
ELVIRA	Efficient Least-square Volume-of-fluid Interface Reconstruction Algorithm
GENSMAC	Generalized Simplified Marker And Cell
HLL	Harten, Lax, and van Leer
HRIC	High Resolution Interface Capturing
LVIRA	Least-square Volume-of-fluid Interface Reconstruction Algorithm
MAC	Marker and Cell
MUSCL	Monotone Upstream-centered Schemes for Conservation Laws
PISO	Pressure Implicit solution by Split Operator
PLIC	Piecewise Linear Interface Calculation

PVC	Polyvinyl Chloride
RANS	Reynolds-Averaged Navier-Stokes
SIMPLE	Semi-Implicit Method for Pressure Linked Equations
SIMPLEC	Semi-Implicit Method for Pressure Linked Equations-Consistent
SIMPLER	Semi-Implicit Method for Pressure Linked Equations-Revised
SLIC	Simple Line Interface Calculation
SOR	Successive-Over-Relaxation
SPH	Smooth Particle Hydrodynamics
TVD	Total Variation Diminishing
UCL	Université Catholique de Louvain
VOF	Volume-Of-Fluid

LIST OF SYMBOLS

ROMAN SYMBOL	DEFINITION
$\mathbf{A}$	Outward-pointing face area vector
C_{fb}	Bed friction coefficient
C_s	Constant coefficient in Smagorinsky turbulence model
c	Suspended-load volumetric concentration
c_b	Actual suspended-load concentration at the interface of the bed-load and suspended-load zones
c_{b*}	Equilibrium (capacity) suspended-load concentration at the interface of the bed-load and suspended-load zones
D_b	Deposition flux of sediment at the interface of bed-load and suspended-load zones
d	Sediment diameter
d_{50}	Median diameter of sediment particles
E_b	Entrainment flux of sediment at the interface of bed-load and suspended-load zones

F	F-function in VOF method
$\mathbf{f}$	External force vector
g	Acceleration of gravity
H	Wave height
H_s	Thickness of moving particles above the bed
h	Water depth
k	Turbulence kinetic energy
k_t	Correction factor of bed shear stress due to sediment concentration
L	Adaptation length of sediment particles
L_b	Bed load adaptation length
$\mathbf{m}$	Unit vector normal to water surface
$\mathbf{n}$	Unit vector normal to computational cell face
p	Pressure
p_d	Dynamic pressure
p'	Pressure correction in SOR method

p'_m	Porosity of sediment deposit
q_b	Actual transport rate of bed load
q_{b*}	Equilibrium (capacity) transport rate of bed load
$\mathbf{r}$	Coordinate vector of computational cell center
S	Surface boundary of control volume
T	Sediment transport stage number
t	Time
U	Velocity magnitude
u	Longitudinal velocity
u_b	Bed-load velocity
$\mathbf{u}_{mesh}$	Mesh velocity vector
V	Volume of control volume
v	Lateral velocity
w	Vertical velocity
x	Longitudinal coordinate

y	Lateral coordinate
z	Vertical coordinate
z_b	Bed elevation
z_s	Water surface elevation

GREEK SYMBOL	DEFINITION
α	Adaptation coefficient of suspended load
α_{bx}	x-direction cosine of bed-load movement
α_{by}	y-direction cosine of bed-load movement
γ	Specific weight of water
γ_s	Specific weight of sediment
Δt	Time step
Δx	Grid spacing in x direction
Δy	Grid spacing in y direction
Δz	Grid spacing in z direction

δ_b	Thickness of bed-load zone
δ_{j3}	Kronecker delta
ε	Turbulence dissipation
κ	von Karman constant
η	Interpolation coefficient of pressure
μ	Dynamic viscosity
μ_m	Molecular viscosity
μ_t	Turbulent viscosity
υ	Kinematic viscosity
ρ	Water density
ρ_s	Sediment density
τ	Stress
τ_b	Effective bed shear stress
τ_{bx}	Longitudinal bed shear stress

τ_{by}	Lateral bed shear stress
τ_{cr}	Critical shear stress
φ_r	Sediment repose angle
φ_x	Bed slope angle in x-direction
φ_y	Bed slope angle in y-direction
$\phi_{upwinding}$	Upwinding coefficient
ω_s	Settling velocity of sediment particles in clear water
ω_{sm}	Settling velocity of sediment particles in turbid water

ACKNOWLEDGMENTS

I would like to sincerely and heartily express my deepest appreciation to my advisor Prof. Weiming Wu for his valuable guidance, support and encouragement throughout my Ph.D. study at NCCHE in the past 4 years. I have been fortunate to have an advisor whose guidance has always provided a well-rounded experience consistent with my long-term career goals. I have been always inspired by his determination, hard working, and accuracy. I am blessed to have him as the role model for my academic life.

I am sincerely grateful to Prof. Mustafa Altinakar, the director of NCCHE, who always inspired me with his skills to transfer knowledge and expertise to students and researchers. I have been also amazed with his leadership skills, talents and academic achievements. I would like to thank Prof. Sam S. Y. Wang who found NCCHE and made this opportunity happen for many students and researchers from all over the world to pursue their academic goals at such an outstanding academic environment. In addition, I appreciate Prof. Yafei Jia and Prof. Yan Ding for their priceless knowledge transfer in the field of numerical modeling of fluid flows. I also express my sincere appreciation to Prof. Cristiane Q. Surbeck at the UM Department of Civil and Environmental Engineering for serving as a member of my dissertation committee and for providing valuable comments and suggestions for my study.

Furthermore I would also like to acknowledge the help I received from the staff of NCCHE, Mr. Paul Smith, Coordinator of Computing Facility Operations, Ms. Kathy McCombs, ex-administrative secretary, and Ms. Natalie Spencer, the administrative secretary of NCCHE. I would like to acknowledge the friendship and help from NCCHE other scientists and students.

At the end, I deeply would like to thank NCCHE to have provided the financial support for my PhD dissertation research. I also appreciate the Graduate School at the University of Mississippi for providing me dissertation and summer research scholarships.

TABLE OF CONTENTS

CHAPTER PAGE

CHAPTER 1 INTRODUCTION 1

1.1 Background 1

1.2 Numerical Study of Dam-Break Flows 3

1.3 Research Objectives 4

1.4 Dissertation Contents 5

CHAPTER 2 LITERATURE REVIEW 7

2.1 Dam-Break Flow Studies 7

2.2 Dam-Break Flow Models for Fixed Beds 8

2.3 Dam-Break Flow Models for Movable Beds 12

2.4 Water Surface Tracking Methods 14

CHAPTER 3 3-D FINITE-DIFFERENCE MODEL OF DAM-BREAK FLOW OVER FIXED BEDS 20

3.1 Governing Equations 20

3.2 Numerical Methods 21

3.3 Water Surface Tracking 23

    3.3.1 SOLA-VOF Advection Scheme 24

    3.3.2 Reconstruction Method 25

3.4 Boundary Conditions 29

    3.4.1 Inlet Boundary Condition 29

    3.4.2 Outlet Boundary Condition 29

    3.4.3 Solid Wall Boundary Condition 30

    3.4.4 Water Surface Boundary Condition 30

3.5 Model Stability 32

3.6 Computational Procedure 32

3.7 Model Test 34

    3.7.1 Initial Stage of Dam-Break Flow over a Wet Flat Bed 35

    3.7.2 Initial Stage of Dam-Break Flow over a Dry Flat Bed 36

3.7.3 Initial Stage of Dam-Break Flow over a Rectangular Obstacle 37

3.7.4 Partial Dam-Break Flow..39

3.7.5 Dam-Break Flow over a Rectangular Block 45

3.8 Summary 49

CHAPTER 4 3-D FINITE-VOLUME MODEL OF DAM-BREAK FLOW OVER FIXED BEDS...50

4.1 Governing Equations...50

4.2 Computational Grid..51

4.3 Numerical Solutions of Continuity and RANS Equations 53

4.3.1 Discretization of Momentum Equation 54

4.3.1.1 Convection Term 55

4.3.1.2 Diffusion Term 55

4.3.1.3 Temporal Term 56

4.3.1.4 Final Discretization Form..56

4.3.2 Pressure Equation 58

4.3.3 Gradient of Flow Properties 60

4.3.4 Pressure-Velocity Coupling Algorithm 61

4.4 Boundary Conditions 61

4.5 Surface Capturing Method 62

4.6 Model Stability 65

4.7 Model Test 65

4.7.1 Initial Stage of Dam-Break Flow over Wet and Dry Flat Beds 66

4.7.2 Breaking Solitary Wave on a Sloping Beach 67

4.7.3 Dam-Break Flow over a Trapezoidal Step 71

4.7.4 Dam-Break Flow over a Triangular Step 73

4.7.5 Dam-Break Flow over an Isolated Block 76

4.7.6 Dam-Break Flow Caused by Partial failure 78

4.8 Summary 81

CHAPTER 5 3-D FINITE-VOLUME MODEL OF SEDIMENT TRANSPORT UNDER DAM-BREAK FLOW OVER MOVABLE BEDS 83

5.1 General Concepts and Definitions........83

5.2 Governing Equations of Sediment Transport........85

5.3 Boundary Conditions........86

5.4 Numerical Solution Methods........87

    5.4.1 Discretization of Suspended-Load Transport Equation........88

    5.4.2 Discretization of Bed-Load Transport Equation........91

    5.4.3 Discretization of Bed Change Equation........92

    5.4.4 Computational Grid Adjustment........92

5.5 Model Parameters........95

    5.5.1 Equilibrium Transport Rate of Bed Load........95

    5.5.2 Near-Bed Equilibrium Concentration of Suspended Load........96

    5.5.3 Effective Bed Shear Stress........97

    5.5.4 Critical Shear Stress........98

    5.5.5 Sediment Turbulent Diffusivity........99

    5.5.6 Sediment Settling Velocity........99

5.5.7 Sediment Adaptation Length 100

5.5.8 Calibration Parameters 101

5.6 Model Test 101

5.6.1 Net Entrainment in a Straight Flume 102

5.6.2 Initial Stage of Dam-Break Flow over Movable Beds 103

5.6.3 Dam-Break Flow over Movable Bed in an Abruptly Expanded Channel 113

5.6.4 Partial Dam-Break Flow over Movable Bed 121

5.7 Summary 128

CHAPTER 6 SUMMARY, CONCLUSIONS, AND FUTURE RESEARCH 130

6.1 Summary and Conclusions 130

6.2 Future Research 133

BIBLIOGRAPHY 135

LIST OF FIGURES

FIGURE PAGE

2.1 Marker points on the interface: (a) height function; (b) line segments........................15

2.2 Mesh setup for volume tracking methods: (a) MAC and (b) VOF..............................18

3.1 3-D finite-difference computational cell (staggered grid) 21

3.2 (a) exact (b) piecewise linear and (c) piecewise constant 2-D reconstructed free surface..26

3.3 Normal vectors of vertices in a 3×3×3 Youngs' stencil 27

3.4 (a) Definition of parameters used in the pressure interpolation of the surface cells and (b) free surface velocity components (2-D view) 31

3.5 Solution steps of the present model 34

3.6 Measured and calculated water surface profiles caused by dam break over wet bed (measurements from Stansby et al., 1998)...36

3.7 Measured and calculated water surface profiles caused by dam break over dry bed (measurements from Ozmen-Cagatay and Kocaman, 2010) 37

3.8 Initial stages of dam-break wave over a rectangular obstacle (left: experimental images from Oertel and Bung, 2012 and right: present model results) 38

3.9 Plan view of the partial dam-break experiment 39

3.10 Photograph of the experimental dam-break carried out by Fraccarollo and Toro (1995) 40

3.11 3-D Snapshots of calculated waster surface elevation 42

3.12 2-D Snapshots of calculated bottom pressure and velocity (left: bottom pressure in m, and right: longitudinal velocity near the bed in m/s) 43

3.13 (a)-(d): Measured (–) and calculated (---) water surface levels; (e)-(h): measured (–) and calculated (---) pressures at the bottom (measurements from Fraccarollo and Toro, 1995) 44

3.14 Measured (–) and calculated (---) longitudinal velocities at 0.1, 0.2, and 0.35 m above the bed (measurements from Fraccarollo and Toro, 1995) 45

3.15 Sketch of the MARIN dam-break experiment (H4 and H2: water surface level measurement gages; P1, P3, P5, and P7: pressure measurement gages around the block) 46

3.16 3-D view of wave propagation process 47

3.17 Time evolution of water surface level: measured (–), calculated (---) (measurements from Kleefsman et al., 2005) 48

3.18 Time evolution of pressure: measured (–), calculated (---)(measurements from Kleefsman et al., 2005) 48

4.1 Sketch of a hexahedral computational cell (points P, N, and face centroid may not necessarily make a straight line) 52

4.2 Definition of donor, acceptor, and upstream cells (the arrow shows the flow direction at the face under consideration) 65

4.3 Measured and calculated water surface profiles caused by dam break over wet bed (measurements from Stansby et al., 1998) 66

4.4 Measured and calculated water surface profiles caused by dam break over dry bed (measurements from Ozmen-Cagatay and Kocaman, 2010) 67

4.5 Schematic side view of (a) solitary wave runup on a sloping beach (b) computational mesh 68

4.6 Propagation of Breaking solitary wave on a sloping beach (solid red line: calculated, blue circles: measurements from Synolakis, 1986) 70

4.7 Simulated wave breaking process on a sloping beach 71

4.8 (a) 3-D sketch of the laboratory flume; (b) side view of the trapezoidal shaped step and the computational mesh around the step 72

4.9 Measured (dots) and calculated (solid line) water surface profiles (measurements from Ozmen-Cagatay and Kocaman, 2011) 72

4.10 (a) 3-D sketch of the laboratory flume; (b) side view of the triangular shaped step and the computational mesh around the step 74

4.11 Measured and calculated water surface time series for the run with dry bed downstream of the step (measurements from Kao and Chang, 2012) 75

4.12 Measured and calculated water surface time series for the run with wet bed downstream of the step (measurements from Kao and Chang, 2012) 75

4.13 (a) 3-D sketch of the MARIN dam-break experiment; (b) the rectangular block 77

4.14 Time evolution of water surface level (measurements from Kleefsman et al., 2005) 77

4.15 Time evolution of pressure (measurements from Kleefsman et al., 2005) 78

4.16 Sketch of the partial dam-break experiment 79

4.17 Measured and calculated water surface levels (measurements from Fraccarollo and Toro 1995) 80

4.18 Measured and calculated pressures at the bottom (measurements from Fraccarollo and Toro 1995)....................80

4.19 Measured and calculated velocities in the longitudinal direction at different vertical distances from the bed (measurements from Fraccarollo and Toro 1995) 81

5.1 Schematic view of flow and sediment transport ($c(z)$=vertical distribution of sediment concentration, $\tau(z)$=vertical distribution of shear stress, $u(z)$=vertical distribution of stream-wise velocity, c_b=near-bed sediment concentration, $\overline{c}_b$=averaged near-bed sediment concentration, and τ_b=bed shear stress) 85

5.2 Schematic definition of the bed-load and suspended-load zones in the finite-volume computational mesh 88

5.3 (a-b) Side views of unit normal vector of cell faces, and (c) Plan view of stencil used to estimate bed slopes (black dots: bed elevation at cell centers, crosses: bed elevation at cell faces)..95

5.4 Vertical distribution of sediment concentration at (a) x/h=4, (b) x/h=10, (c) x/h=20, and (d) x/h=40 (solid line: calculated, squares: measurements from Van Rijn 1981) 103

5.5 Initial dam-break configuration conducted by Spinewine and Zech (2007).............104

5.6 Comparison between measured and calculated (using C_{fb}=0.15 and L=0.025 m) water surface and bed profiles (measurements and snapshots from Spinewine and Zech, 2007) 105

5.7 Comparison between measured and calculated (using C_{fb}=0.15 and L=0.025 m) bed profiles (measurements from Spinewine and Zech, 2007) 106

5.8 Sensitivity analysis of bed elevation change to varying adaptation length (C_{fb}=0.15, measurements from Spinewine and Zech, 2007) 108

5.9 Sensitivity analysis of bed elevation change to varying bed friction coefficient (L=0.05 m, measurements from Spinewine and Zech, 2007) 109

5.10 Comparison between measured (symbols) and calculated (using C_{fb}=0.35 and L=0.05 m; solid lines) water surface and bed profiles (measurements from Fraccarollo and Capart, 2002) 111

5.11 Wave front with high sediment load at the initial stage of gate removal t=0.25 s (picture from Fraccarollo and Capart, 2002) 112

5.12 Sensitivity analysis of bed elevation change to varying adaptation length (C_{fb}=0.2, measurements from Fraccarollo and Capart, 2002) 112

5.13 Sensitivity analysis of bed elevation change to varying bed friction coefficient (L=0.05 m, measurements from Spinewine and Zech, 2007) 113

5.14 Plan view of experimental setup (dam-break flow over movable bed in an abruptly expanded channel) 114

5.15 Calculated water surface level (in meter) downstream of the expansion zone at t=2.3 s (C_{fb}=0.2 and L=0.025 m) 116

5.16 Measured and calculated water surface time series (C_{fb}=0.2 and L=0.025 m) 117

5.17 Magnitude of calculated resultant velocity (in m/s) near the bed downstream of the expansion zone at t=3.3 s (C_{fb}=0.2 and L=0.025 m) 118

5.18 Flow pattern downstream of the expansion zone at t=3.3 s (C_{fb}=0.2 and L=0.025 m) 118

5.19 Final bed topographies (units in meter) downstream of the expansion, top map: calculated (using C_{fb}=0.2, L=0.025 m), bottom map: measured (measurements from Goutiere et al. 2011) 119

5.20 Measured and calculated cross sections of final bed (C_{fb}=0.2, dotted line: initial bed level) 120

5.21 Measured and calculated cross sections of final bed (L=0.025 m, dotted line: initial bed level) 121

5.22 Plan view of experimental setup (partial dam-break flow over movable bed) 124

5.23 Calculated water surface level (in meter) downstream of the dam at *t*=3 s (C_{fb}=0.2 and *L*=0.025 m) 124

5.24 Measured and calculated water surface time series (C_{fb}=0.2 and *L*=0.025 m) 125

5.25 Magnitude of calculated resultant velocity (in m/s) near the bed downstream of the dam at *t*=3 s (C_{fb}=0.2 and *L*=0.025 m) 125

5.26 Final bed topographies (units in meter) downstream of the dam, top map: calculated (using C_{fb}=0.2, *L*=0.025 m), bottom map: measured (IAHR working group, 2012) 126

5.27 Measured and calculated final longitudinal bed profiles (C_{fb}=0.2) 127

5.28 Measured and calculated final longitudinal bed profiles (*L*=0.025 m) 128

CHAPTER 1

INTRODUCTION

1.1 Background

Water is the vital liquid to support all forms of life on the earth. It is the essential element for the health of the world's environment. Although seventy percent of the Earth is covered with water, a significant portion of the world population suffers water shortage. This is because 96.5% of the water resources are salt water found in oceans (Gleick 1993). On the other hand, 98.8% of the Earth's freshwater is in ice and groundwater and only a small portion is in rivers and lakes. The demand for water as a result of the expanding world population and economic growth has increased the importance of freshwater resources. Therefore, it is essential to collect and store available freshwater water resources on the Earth. Building dams is one way of storing freshwater in large quantities.

Dams are one of the common ways to collect and store waters streaming in rivers, and provide essential benefits including drinking water, power generation, flood protection, irrigation, and recreation. In ancient times, dams were built for the single purpose of water supply or irrigation. As civilizations developed, there was a need in having multipurpose dams for water supply, irrigation, flood control, navigation, water quality, sediment control and energy. Dams store not only water streaming in rivers but also sediment particles. In general, rivers carry sediments and when a river is stilled in the reservoir behind a dam, the sediments deposit to the bottom of the reservoir. Therefore, depending on the reservoir size, a considerable volume of water and accumulated sediments exist behind a dam. Storing this amount of water and sediment mixture creates liabilities. Thus, it is important to ensure that a dam and its reservoir are well-designed, well-constructed, well-maintained, and well-operated. Otherwise a dam failure may result in sudden release of the mixture behind a dam, which creates a destructive muddy flood.

Despite the efforts to promote dam safety, dam failures sometimes occur as a result of overtopping due to an intense storm and associated runoff, foundation defects, piping and seepage, human error, earthquake, terrorism attacks, etc. Dam failure is a catastrophic event that may cause significant loss of life, and property and environmental damages due to uncontrolled release of large amount of water and sediment mixture from the reservoir which leads to a destructive flood propagating downstream. According to consequences of the failure, the hazard classification of a dam can be high hazard, significant hazard, and low hazard (Interagency Committee on Dam Safety, 2004). Dams assigned the high hazard potential classification are those whose failure will probably cause loss of human life, serious damage to homes, industrial or commercial buildings, important public utilities, and transportation systems or roads. Significant hazard dam failure results in no probable loss of human life but may cause significant property loss and environmental damages such as damage to main roads, minor railroads, or cause interruption of use or service of relatively important public utilities. Dams assigned the low hazard potential classification are those whose failure results in no probable loss of human life but may cause low economic and/or environmental losses such as damage to farm buildings, agricultural lands, and minor roads. Losses are principally limited to the owner’s property. The total number of dams with the classification of high hazard potential is increasing as they reach their lifespan. For example, the number of dams with high-hazard potential has increased from 10,118 dams in 2002 to 13,991 in 2012 (American Society of Civil Engineers, 2013). Therefore, devastating outcomes of dam break necessitate the study of dam-break flows which provides the information for risk assessment and management of river valleys downstream of a dam.

Basically, dam-break flow studies can be categorized as analytical, experimental/field, and numerical studies. Analytical study focuses on solving the governing equations using calculus, trigonometry, and other mathematical techniques. Since the governing equations of dam-break flow are complicated and usually non-linear, analytical approaches use a number of assumptions to simplify the governing equations. In case of movable bed, the governing equations of sediment transport bring extra complexity and therefore extra assumptions. These assumptions limit the application of exact analytical solutions to a narrow range of dam-break flow studies. Experimental study of dam-break flow overcomes the limitation of analytical approaches by using physical models and measuring information in laboratory. The advent of new technology and measurement tools has facilitated the experimental study of dam-break flows in which it is now feasible to simulate more complicated cases. Although experimental study of dam-break flow is financially expensive and time-consuming especially for large scale cases, they provide a reliable set of data to verify and validate numerical models. Numerical study of dam-break flow overcomes the limitations of analytical and experimental approaches. With increasing computer processing capacity, numerical simulations have become attractive and cost-effective.

1.2 Numerical Study of Dam-Break Flows

Numerical simulations of dam-break flow has received considerable attention such that several techniques have been developed over the years to solve one-dimensional (1-D), two-dimensional (2-D), and three-dimensional (3-D) equations of dam-break flow. Appreciable efforts have been dedicated to the development of 1-D and depth-averaged 2-D numerical models to simulate dam break flows. Because these models solve the shallow water equations based on a number of assumptions, such as hydrostatic pressure distribution and insignificant free surface curvature, they are inadequate to simulate flows involving significant variations of velocity and pressure in the vertical direction, e.g., in the initial stages of dam-break flow, at dam-break wave front, and near in-stream structures. Therefore, it is vital to simulate such flows by a 3-D model, which solves the Reynolds-Averaged Navier-Stokes (RANS) equations, to obtain meaningful and correct numerical results. On the other hand, most of the existing models focus on hydrodynamic studies of dam-break flow over fixed beds without considering sediment transport and bed morphology changes. The field survey, however, suggests that during the dam-break process, especially in the early stage of the dam failure, the flow is fast and it is strongly coupled with sediment motion and bed changes. The accurate simulation of dam-break flow must consider adequately sediment motion during this period (Lin et al. 2011).

1.3 Research Objectives

In this PhD dissertation, the interest is focused on the development of a numerical model for dam-break flows over movable beds. In particular, the main research objectives of this study are divided to the following major parts:

1- The first task is developing a 3-D finite-difference model of dam-break flow over fixed beds based on rectilinear and staggered grids. The model simulates only the hydrodynamic features of dam-break flows over non-erodible beds without considering sediment transport. The SOLA-VOF scheme is used to track the free surface boundary. The aim of developing the 3-D finite-difference model is assessment of the VOF technique to track the free surface boundary in dam-break flows. To investigate the efficiency and accuracy of the Volume-of-Fluid (VOF) technique, the developed model is verified by several experimental dam-break flows.

2- Development of a 3-D hydrodynamic finite-volume model to simulate dam-break flows over fixed beds is the second aim of this dissertation. The developed finite-volume model is superior to the above finite-difference model because it uses irregular, collocated meshes, which can be conveniently used for fitting on irregular beds. Moreover, it can be extended to use moving meshes to simulate dam-break flows over movable beds where the bed topography may change with time due to sediment transport.

3- The final goal is developing a 3-D non-equilibrium sediment transport model which can be linked to the 3-D hydrodynamic model. In other words, the final scope is to develop a 3-D finite-volume model for dam-break flows over movable beds which comprises decoupled hydrodynamic and sediment transport modules.

1.4 Dissertation Contents

The remainder of the dissertation contains 5 chapters. Chapter 2 reviews the past and recent works on numerical simulation of dam-break flows over fixed and movable beds. It also includes a literature review of common interface tracking methods. In Chapter 3, the development of the 3-D finite-difference model is described. The model is tested using several experimental dam-break flows over fixed beds. Chapter 4 describes the development of the 3-D finite-volume model for dam-break flows over fixed beds and the test results are demonstrated.

In Chapter 5, the 3-D non-equilibrium sediment transport model is developed and linked to the hydrodynamic model presented in Chapter 4. The model is tested using experimental dam-break flows over movable beds. Finally, Chapter 6 provides summary, conclusions, and future research.

CHAPTER 2

LITERATURE REVIEW

This chapter presents a comprehensive review of existing dam-break flow models. The basic theories and numerical methods used in the models are described briefly. In the last sections, the interface tracking approaches are introduced as well.

2.1 Dam-Break Flow Studies

Studies related to dam-break flows have been an interesting topic to environmental and hydraulic engineers and researchers for several decades. There have been substantial efforts to understand and simulate the mechanism of dam-break flows. Although the earliest study by Ritter (1892) was based on an analytical solution of the simplified dam-break problem, the complexity of governing equations caused researchers to be more interested in experimental and numerical approaches.

In recent decades, computer modeling has become available and many investigators have devoted their research to simulate and predict dam-break flows and their consequences numerically. Numerical models simulate and calculate the characteristics of flood resulting from the failure of a dam using finite-difference, finite-volume, or finite-element methods. The calculated data, including the water surface level, velocity, pressure, forces, etc., are used to identifying and predicting areas where are in danger of inundation and losses. Although most natural reservoirs contain a significant volume of accumulated sediment, the early developed models simulated dam-break flows over non-erodible beds without sediment transport computations. On the other hand, when a dam fails, the accumulated sediments in the reservoir are washed out by the released flood and deposit in downstream reach. Therefore, the released flood from the reservoir of a failed dam may cause the downstream lands considerable bed and bank erosion and/or deposition. The morphological changes of river may strongly affect the hydrodynamic behavior of the dam-break flood. Therefore, the interaction between flow and sediment transport has raised a strong motivation to study dam-break flows over movable beds. In the subsequent sections, a review of developed numerical models for dam-break flow simulation on fixed and movable beds are presented.

2.2 Dam-Break Flow Models for Fixed Beds

Numerical models developed for dam-break flow simulation on fixed beds assume that the bed is non-erodible and thus the sediment transport process is negligible. Depending on the development purposes of these models, they solve the 1-D, 2-D, and 3-D governing equations of incompressible flows.

1-D dam-break flow models solve the St. Venant equations, which are a set of nonlinear hyperbolic equations derived by integrating the 3-D continuity and momentum (Navier-Stokes) equations over the cross section with the assumption of hydrostatic pressure distribution. Therefore, the governing equations are solved in the stream-wise direction of the channel without considering the flow details over the cross section. 2-D models can be categorized in horizontal and vertical models. The 2-D horizontal models solve the shallow water equations in the horizontal plane whereas the 2-D vertical models solve the Navier-Stokes equations in the longitudinal and vertical directions. The shallow water equations are derived from depth-integrating the 3-D continuity and momentum equations. The derived equations are valid where the vertical length scale is negligible compared to the horizontal length scale. Under this condition, the vertical component of the fluid velocity is insignificant and the vertical pressure gradient is hydrostatic.

The St. Venant and shallow water equations have been solved by numerous approaches but the most widely-used ones among them are shock-capturing schemes, such as approximate Riemann solvers and Total Variation Diminishing (TVD) schemes. Rajar (1978) proposed a 1-D mathematical model based on the diffusive and Lax-Wendroff schemes for highly nonperismatic channels. Katopodes and Wu (1986) developed a 1-D explicit finite-element model that was second-order accurate in time and fourth-order in space. Bellos and Sakkas (1987) studied the 1-D dam-break flood wave on a broad rectangular channel using the MacCormack finite-difference algorithm. Savic and Holly (1993) considered the dam-break wave as a flow regime with strong shocks in such a way that the 1-D governing equations were solved with two Godunov methods based on linear and piecewise parabolic interpolations. Hicks et al. (1997) developed a 1-D model which solved the conservative and non-conservative forms of the St. Venant equations using the Characteristic Dissipative Galerkin (CDG) finite-element and the four-point implicit or Box Finite-Difference (BFD) methods. Jha et al. (1995) developed a model to investigate the accuracy of the Roe's first-order scheme and its second-order extension based on the Lax-Wendroff numerical flux, the MUSCLE, and the modified flux approach for dam-break flow problems. Wang et al. (2000) developed a model based on a hybrid type of second-order TVD scheme for dam-break problems. The proposed scheme combines the first-order upwind and the second-order Lax-Wendroff schemes with the optimum-selected limiter. Their scheme was originally developed for 1-D problems and the extension for the 2-D shallow water equations was presented by an operator splitting technique. Ying et al. (2004) proposed a numerical method to solve the St. Venant equations. They developed a model based on the proposed scheme which used an upwind conservative scheme with a weighted average water-surface-gradient approach. Ying and Wang (2008) developed a model which solved the St. Venant equations using their proposed schemes based on the HLL approximate Riemann solver to treat the discontinuities of the dam-break waves. Kuiry et al. (2008) solved the shallow water equations using the finite-volume method over triangular cells. The diffusion of momentum due to viscosity and turbulence was neglected and the fluid flux across a cell was approximated using the Roe's approximate Riemann solver. Altinakar et al. (2012) developed two state-of-the-art models called DSS-WISE and WGFEM to simulate dam/levee break/breaching floods and/or fluvial floods over complex topography. They solved the 2-D shallow-water equations using a shock-capturing finite-volume scheme that accepted regular DEM-based grids. Their models were parallelized using OpenMP and GPU programing to accelerate the computations.

Due to the assumptions used in 1-D and horizontal 2-D dam-break flow models, these models are inadequate to simulate flows involving significant variations of flow depth, velocity, and pressure in the vertical direction, such as dam-break flow near in-stream structures. Simulating these complex flows must rely on vertical 2-D or 3-D models which solve the RANS equations. Although the vertical 2-D models are applicable where the lateral changes of flow is negligible, the 3-D models are appropriate to study dam-break flows with rapid changes in the horizontal and vertical directions. Mohapatra et al. (1999) developed a vertical 2-D model for incompressible inviscid dam-break flows in the vertical plane. They used the GENSMAC Navier-Stokes Solver and the VOF technique to solve the governing equations and track the free surface, respectively. The governing equations were discretized using the finite-difference approach on a staggered grid. The effects of turbulence and bed friction were neglected in their model. Kleefsman et al. (2005) investigated the water impact and green water loading using a 3-D model. The RANS equations were solved on a fixed Cartesian staggered grid using the finite-volume method and the VOF technique with a height function was applied to track the water surface changes. The surface tension was taken into account by calculating the total curvature of the free surface. The Poisson equation of pressure was solved using the SOR method. Ferrari et al. (2010) developed a 2-D dam-break model based on the shallow water assumptions and also a 3-D model based on the Smooth Particle Hydrodynamics (SPH) approach. Their 3-D SPH model considered the weakly compressible Navier-Stokes equations which enabled the model to use the Tait equation of state instead of the Poisson relation for the determination of pressure. The models were tested by an experimental dam-break flow released from a partial opening to duplicate a dam collapse in an open valley. The comparisons showed that the results calculated by the 3-D SPH model are superior to those calculated by the 2-D shallow water model. Yang et al. (2010) studied the dam-break flows by developing a 3-D model which solved the continuity and RANS equations using the finite-difference method in the Cartesian staggered grid. They applied the VOF technique to track the water surface and the k-ε model for turbulence closure of the RANS equations. Pressure-velocity coupling in the governing equations was achieved by using a two-step projection method. Marsooli et al. (2011) developed a vertical 2-D model for dam-break flows. Their model solved the 2-D RANS equations in the longitudinal and vertical directions using a finite-difference method on the Cartesian staggered grid. The Smagorinsky sub-grid model was used for turbulence closure of the RANS equations and the free surface was tracked by means of the VOF technique.

2.3 Dam-Break Flow Models for Movable Beds

Simulation of dam-break flow over movable beds is much more challenging than that over fixed beds. One of the problems encountered in the movable-bed case is that the transported sediment load by the dam-break wave is so high and the bed varies so rapidly that the effects of sediment transport and bed change on the flow cannot be ignored. Another problem is that the sediment transport in the higher flow regime, such as dam-break flow, is little understood and the existing sediment transport formulas may not be applicable (Wu 2007, p363). In such regions, the assumption of equilibrium sediment transport capacity is violated and the sediment transport is in non-equilibrium condition.

Capart and Young (1998) developed a 1-D shallow-water model for dam-break flow over movable beds. They considered the non-equilibrium sediment transport and the effects of sediment on the flow calculations. Fraccarollo and Capart (2002) proposed a 1-D dam-break flow model over mobile beds based on a shallow-water approach. Their model divided the water column into two layers in which the clear water in the upper layer and the mixture of sediment and water in the lower layer. They assumed that the sediment concentration of the mixture layer is equal to the bed material concentration in the bed which can overestimate the sediment concentration. Capart and Young (2002) and Spinewine (2005) developed 1-D two-layer models with variable concentration in the mixture layer.

Cao et al. (2004) developed a dam-break flow model over erodible beds. They solved 1-D mass and momentum equations of water-sediment mixture for channel with rectangular cross sections of constant width, over mobile beds covered by uniform and non-cohesive sediments. The numerical scheme used to approximate fluxes was the total-variation-diminishing (TVD) version of the second-order weighted average flux method in conjunction with the HLLC approximate Riemann solver and SUPERBEE limiter. Wu and Wang (2007) established a 1-D model to simulate the fluvial processes under dam-break flow over movable beds. They considered the interaction of flow, sediment transport, and bed change by solving 1-D unsteady sediment-laden flow in rivers. The 1-D shallow water equations were derived by section integrating the 3-D shallow water equations with longitudinally varying flow density. The effects of sediment concentration and bed change were taken into account by using the density of water and sediment mixture in the governing equations and including the bed change rate in the continuity equation. The non-equilibrium transport of bed-load and suspended-load was used in the sediment transport computations. The bed-load transport capacity and the suspended-load near-bed concentration in the sediment transport equations were estimated by introducing a correction factor in Van Rijn (1984a,b) formulas. They replaced the water density with the flow and sediment mixture density near the bed to make these formulas applicable to situations of high sediment transport. The flow and sediment transport equations were solved by an explicit finite-volume method with the first-order upwind scheme. A 1-D finite-volume model was developed by Zhang et al. (2013) for simulating non-equilibrium sediment transport in dam-break flows.

Xia et al. (2010) proposed a 2D morphodynamic model for predicting dam-break flows over movable beds. Their model solved the shallow-water and non-equilibrium sediment transport equations based on a finite-volume method on unstructured triangular meshes. Their model solved the suspended and bed load transport equations separately. They also considered the effects of sediment concentration and bed evolution on the flood wave propagation. Wu et al. (2012) developed a depth-averaged 2D model to simulate the flow, sediment transport and morphological changes induced by embankment break/breach. The model solved the governing equations using a finite-volume method with the HLL approximate Riemann solver on structured rectangular grids. Their model considers the non-equilibrium total-load non-cohesive sediment transport.

3-D numerical modeling of dam-break flow over movable beds is more challenging than 1-D and 2-D modeling. In a 3-D model, as erosion and deposition occur over time the computational mesh must be specially treated in order to track the time evolution of bed surface boundary. To the author's knowledge, no successful numerical study of 3-D dam-break flow over movable beds has been reported up to now. The present dissertation may be the first study on 3-D numerical simulation of dam-break flows over movable beds.

2.4 Water Surface Tracking Methods

In vertical 2-D and 3-D dam-break flow models, the water depth is not explicitly included either in the momentum equations or the continuity equation, and therefore, efforts must be devoted to trace the free surface boundary. To track the movement of free surface, a fluid-fluid interface tracking technique must be used. Basically, two classes of methodologies, called surface tracking methods and volume tracking methods, have been used to track the moving boundaries. In surface tracking methods, the interface is specified by an ordered set of marker points. As shown in Fig. 2.1, the marker points may be represented either by a height function or line segments (a parametric function). The height function method represents the interface by defining its distance from a reference plane. The time evolution of the height function $h=f(\mathrm{x}, y, t)$ is governed by the following kinematic equation expressing the fact that the surface moves with the fluid (Hirt and Nichols, 1981):

$$\frac{\partial h}{\partial t} + u\frac{\partial h}{\partial x} + v\frac{\partial h}{\partial y} = w \tag{2.1}$$

where t is the time, x and y are the horizontal coordinates, and u, v, and w are the velocity components in x, y and z directions, respectively. Note that this method does not work for multiple-valued surfaces, such as the breaking wave shown in Fig. 2.1(b), which have more than one h value for a given point of the reference plane.

The line segments approach (Nichols and Hirt, 1971) uses chains of short line segments, or in other words, points connected by line segments. This method is not limited to single-valued surfaces but requires more storage since coordinates for each point must be stored and for accuracy it is best to limit the distance between neighboring points to less than the minimum mesh size. The time evolution of line segments can be accomplished by simply moving each point with the local fluid velocity. This method is not convenient when two surfaces intersect or a surface folds over on itself. In this case, segment chains must be reordered possibly with adding or removing some chains. Detection of intersections, reordering of the line segments, and extension of the line segment approach to 3-D surfaces are not trivial (Hirt and Nichols, 1981).

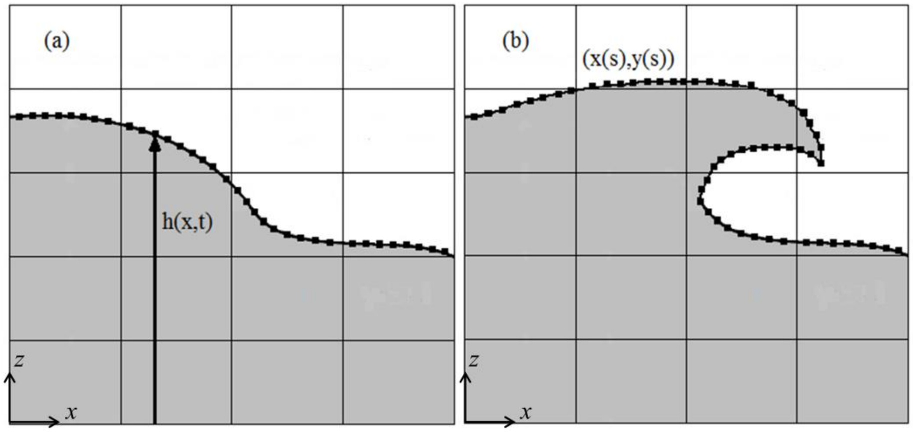

Fig. 2.1 Marker points on the interface: (a) height function; (b) line segments

In volume tracking methods, the domain is divided to disjoint solution regions such that the boundary between them is the interface. Since this approach follows regions rather than surfaces, all logic problems associated with intersecting surfaces are avoided. The regions can be distinguished by either marker points, such as the Marker and Cell (MAC) method, or a fraction function, such as Volume-of-Fluid (VOF) method, and can be advanced in time using an auxiliary kinematic equation. The MAC method, proposed by Harlow and Welch (1965), was the earliest volume tracking method. In this technique, marker particles are distributed initially in the computational cells and convected with the local fluid velocity. Distribution of particles determines the interface configuration, as shown in Fig. 2.2(a). The main shortcoming of the MAC method is that a massive number of particles distributed throughout the domain are needed in order to estimate the interface accurately. This would lead to an expensive computational effort especially for large scale and 3-D cases.

The VOF method provides the same hypothesis available in the MAC method but it requires only one storage variable. The VOF method treats the fluid-fluid interface by introducing a step function F(x,y,t) that is defined to be unity at any point occupied by a particular fluid and zero at points occupied by other fluid. When averaged over the cells of a computing mesh, the average value of F in a cell is equal to the fractional volume of the cell occupied by each fluid and simply called F-function. Therefore, for example, consider two different types of fluid A and B, a cell filled by fluid A has a unit value of F whereas a zero value of F indicates a cell filled by fluid B. Cells with F value between zero and one contain the interface separating fluids A and B. In surface waters problems, water can be assumed as fluid A and air as fluid B.

For an incompressible flow, the time evolution of the F-function is calculated using the following advection equation:

$$\frac{\partial F}{\partial t}+\frac{\partial\left(u_i F_i\right)}{\partial x_i}=0 \tag{2.2}$$

Since the *F*-function is a step function which changes between zero and one abruptly, regular advection techniques cannot be used because numerical diffusion and dispersion errors destroy the sharp nature of the *F*-function distribution and rapidly smear and diffuse the surface. Therefore, special care must be taken to determine its derivatives. Widespread research has been devoted to define the advection scheme in such a way that the sharp definition of fluid surface is preserved and diffusion errors are avoided. Basically, advection schemes are categorized in interface-tracking and interface-capturing methods.

In interface-tracking methods the interface is reconstructed in each computational cell and advected based on the local velocity in a Lagrangian way. The accuracy of these methods strongly depends on the reconstructed interface in each single computational cell. Several piecewise constant and piecewise linear interface reconstruction methods have been developed. In piecewise constant algorithms the interface within each cell is assumed to be parallel with one of the local mesh coordinates. The SLIC method of Noh and Woodward (1976) reconstructs the interface using the piecewise constant method. Piecewise linear methods reconstruct the interface by estimating the slope and intercept of the interface in each computational cell. These methods can be named PLIC (Piecewise Linear Interface Calculation) methods. Among PLIC methods the Youngs (1982 and 1984) methods are notable. However, many extensions to the early work of Youngs have reported in literature. For example, Kothe et al. (1996) extended Youngs method to unstructured meshes. Pilliod and Pukett (2004) introduced two 2-D methods for determining the normal vector, which are second-order and called LVIRA (Least-square Volume-of-fluid Interface Reconstruction Algorithm) and ELVIRA (Efficient Least-square Volume-of-fluid

Interface Reconstruction Algorithm). Both methods are based on generating a linear interface which minimizes the volume fraction error in the neighboring cells and has zero error in the central cell.

In interface-capturing methods, the exact shape of the interface in each computational cell is not necessarily required and the main care must be taken in calculating the *F*-function at cell faces. Generally, these methods use a switching strategy between a compressive and a high-resolution scheme to preserve the interface resolution. The switching function is based on the angle between the interface and the grid orientation. In the first VOF technique introduced by Hirt and Nichols (1981), called SOLA-VOF, a combination of donor-acceptor formulation was used to advect the *F*-function. Torey et al. (1985) modified the advection scheme to make the early proposed VOF method more mass conservative. Muzaferija and Peric (1998) and Muzaferija et al. (1998) introduced the High-Resolution Interface-Capturing scheme (HRIC), which was based on a blending strategy between the Bounded Downwind and Upwind Differencing schemes. The Compressive Interface Capturing Scheme for Arbitrary Meshes (CISCAM) scheme proposed by Ubbink and Issa (1999) is an interface-capturing scheme based on the HYPER-C and ULTIMATE-QUICKEST (UQ) schemes.

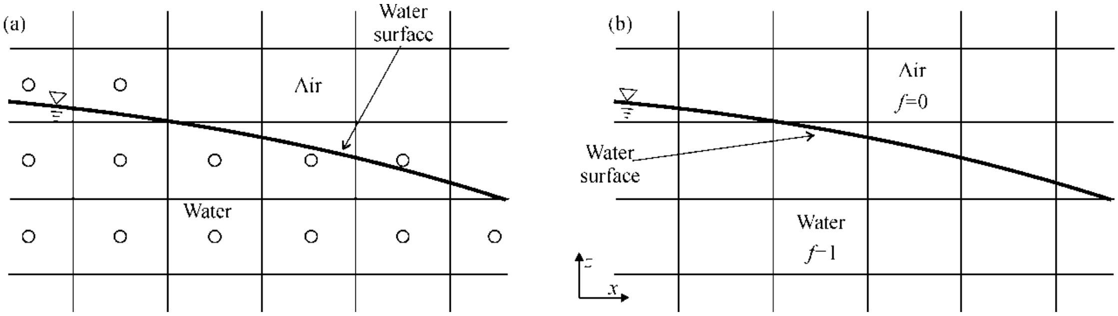

Fig. 2.2 Mesh setup for volume tracking methods: (a) MAC and (b) VOF

In addition, several other interface tracking methods, such as level set method and SPH, can be applied to handling the complex dam-break flows. The level set method uses a scalar function with opposite signs in either side of the interface and a value of zero on the interface (Osher and Sethian, 1988). The SPH method, which was introduced by Lucy (1977) and Gingold and Monaghan (1977), solves the governing equations without using a computational mesh by replacing the fluid with a set of particles that move with the flow motion, and thus can simulate the evolution of the free surface.

Among the aforementioned interface tracking methods, the VOF method is one of the most mature and widely used methods for vertical 2-D and 3-D dam-break flow simulations. Therefore, it is chosen in the present study.

CHAPTER 3

3-D FINITE-DIFFERENCE MODEL OF DAM-BREAK FLOW OVER FIXED BEDS

This chapter presents the development of a 3-D finite-difference model to simulate unsteady flows due to dam-break over fixed beds. The developed model solves the 3-D Reynolds-averaged Navier-Stokes equations (RANS) equations using a finite-difference method on rectilinear, staggered grids. The Smagorinsky sub-grid model is used for turbulence closure of the RANS equations. The developed model tracks the movement of water surface by means of the VOF method, which uses the 3-D Parker and Youngs method and the SOLA-VOF approach for interface reconstruction and evolution, respectively.

3.1 Governing Equations

In the present model, the pressure and velocity fields are calculated by solving the 3-D RANS equations for incompressible flows, which are written in the Cartesian coordinate system as follows:

$$\frac{\partial u_i}{\partial x_i} = 0 \tag{3.1}$$

$$\frac{\partial u_i}{\partial t} + u_j \frac{\partial u_i}{\partial x_j} = \frac{1}{\rho} f_i - \frac{1}{\rho}\frac{\partial p}{\partial x_i} + \frac{1}{\rho}\frac{\partial \tau_{ij}}{\partial x_j} \tag{3.2}$$

where x_i ($i=x,y,z$) are the components of the coordinate system, u_i are the components of the flow velocity, f_i are the components of the external forces, p is the pressure, ρ is the water density, and

τ_{ij} ($j=x,y,z$) are the stresses. The stresses are determined using the Boussinesq's eddy viscosity concept:

$$\tau_{ij} = \mu\left(\frac{\partial u_i}{\partial x_j} + \frac{\partial u_j}{\partial x_i}\right) \tag{3.3}$$

where μ is the viscosity including the molecular (dynamic) and turbulent viscosities ($\mu=\mu_m+\mu_t$). The turbulent viscosity is determined by the Smagorinsky (1963) sub-grid model:

$$\mu_t = C_s^2 \Delta^2 \sqrt{2S_{ij}^2} \tag{3.4}$$

where C_s is a coefficient between 0.1 and 0.25, $S_{ij} = \left(\partial u_i / \partial x_j + \partial u_j / \partial x_i\right)/2$ and $\Delta=(\Delta x \Delta y \Delta z)^{1/3}$ with Δx, Δy, and Δz being the grid spacing in x, y, and z directions, respectively.

3.2 Numerical Methods

The governing equations are discretized by means of finite-difference method. Fig. 3.1 shows a computational cell that is a hexahedron embraced by six perpendicular faces. The staggered grid system is used such that the velocity components are defined across the cell faces while other variables, such as pressure, are specified at the cell center.

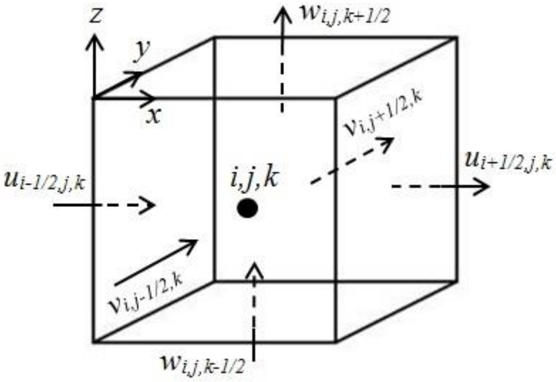

Fig. 3.1 3-D finite-difference computational cell (staggered grid)

In the momentum equation, Eq. (3.2), the time derivative term is discretized using the Euler scheme, the convection fluxes are approximated using the upwind difference scheme, and the diffusion term is discretized using the central difference scheme. The discretized RANS equation in the x direction can be written in the following explicit form:

$$u_{i+1/2,j,k}^{t+\Delta t} = u_{i+1/2,j,k}^{t} - \Delta t \left[\frac{p_{i+1,j,k}^{t} - p_{i,j,k}^{t}}{\rho\left(x_{i+1} - x_i\right)} + \mathrm{FUX} + \mathrm{FUY} + \mathrm{FUZ} - \mathrm{VISX} - \mathrm{TUX} \right] \tag{3.5}$$

where t is the time, Δt is the time step, VISX and TUX are the viscous and turbulent components of the diffusion term, and FUX, FUY, and FUZ are the convection terms defined as

$$\mathrm{FUX} = u\frac{\partial u}{\partial x},\ \mathrm{FUY} = v\frac{\partial u}{\partial y},\ \mathrm{FUZ} = w\frac{\partial u}{\partial z} \tag{3.6}$$

Analogously, the RANS equations in y and z directions can be similarly discretized. After the RANS equations are solved explicitly, the velocity and pressure fields must be corrected to satisfy the continuity equation. Herein, a 3-D extension of the 2-D Successive-Over-Relaxation (SOR) iterative method (Nichols et al., 1980) is adopted to correct the pressure and velocity fields. In this method the pressure is corrected in every computational time step by the following pressure correction relation

$$p_{i,j,k}^{n+1} = p_{i,j,k}^{n} + p'_{i,j,k} \tag{3.7}$$

where

$$p'_{i,j,k} = \frac{-S}{\partial S/\partial p} \tag{3.8}$$

and S is the continuity equation. Superscript n stands for iteration index. The above pressure correction is calculated only for cells which are full of fluid. The pressure boundary condition on the water surface, which is elaborated later on, is used to calculate the pressure field of cells which contain the free surface. The calculated pressure correction $p'_{i,j,k}$ updates the flow velocity components as:

$$u_{i+1/2,j,k}^{n+1}=u_{i+1/2,j,k}^{n}+\Delta t\frac{p'_{i,j,k}}{\rho\left(x_{i+1}-x_i\right)} \tag{3.9a}$$

$$u_{i-1/2,j,k}^{n+1}=u_{i-1/2,j,k}^{n}-\Delta t\frac{p'_{i,j,k}}{\rho\left(x_i-x_{i-1}\right)} \tag{3.9b}$$

$$v_{i,j+1/2,k}^{n+1}=v_{i,j+1/2,k}^{n}+\Delta t\frac{p'_{i,j,k}}{\rho\left(y_{j+1}-y_j\right)} \tag{3.9c}$$

$$v_{i,j-1/2,k}^{n+1}=v_{i,j-1/2,k}^{n}-\Delta t\frac{p'_{i,j,k}}{\rho\left(y_j-y_{j-1}\right)} \tag{3.9d}$$

$$w_{i,j,k+1/2}^{n+1}=w_{i,j,k+1/2}^{n}+\Delta t\frac{p'_{i,j,k}}{\rho\left(z_{k+1}-z_k\right)} \tag{3.9e}$$

$$w_{i,j,k-1/2}^{n+1}=w_{i,j,k-1/2}^{n}-\Delta t\frac{p'_{i,j,k}}{\rho\left(z_k-z_{k-1}\right)} \tag{3.9f}$$

The divergence of the velocity field, i.e. the continuity equation (3.1), is calculated based on the corrected values of velocity and the iteration is continued until a divergence less than a small value, for example 0.001, is reached.

3.3 Water Surface Tracking

In the present model the water surface movement is tracked using the VOF method. The VOF method treats the water surface by introducing the *F*-function to be unity at any cell occupied by fluid and zero at empty cells. This implies that a fluid cell (F cell) filled by water has the *F*-function of a unit value, whereas a zero value indicates an empty cell (E cell) which is filled by air. Cells with *F*-function between zero and one contain the water surface and called surface cells (S cell). Basically, The VOF algorithm consists of two steps: advection and reconstruction. In VOF methods such as SOLA-VOF which are based on algebraic algorithms rather than geometric ones, the advection step computes the advection of the *F*-function and the surface reconstruction is not necessary.

For an incompressible flow, the VOF algorithm solves the following advection equation to compute the time evolution of the *F*-function:

$$\frac{\partial F}{\partial t}+\frac{\partial (uF)}{\partial x}+\frac{\partial (vF)}{\partial y}+\frac{\partial (wF)}{\partial z}=0 \tag{3.10}$$

3.3.1 SOLA-VOF Advection Scheme

The SOLA-VOF scheme proposed by Nichols et al. (1980) is used to trace the changes of water surface boundary. Time evolution of Eq. (3.10) is achieved using an operator split method since the scheme was originally developed for 1-D flows. The operator splitting method applies the 1-D advection equation in separate steps for every coordinate direction. Therefore, the problem is split into sequential updates of the *F*-function in each spatial dimension as follows:

$$F^{*}_{i,j,k}=F^{t}_{i,j,k}-\Delta t\frac{\partial uF}{\partial x},\quad F^{**}_{i,j,k}=F^{*}_{i,j,k}-\Delta t\frac{\partial vF}{\partial y},\quad F^{t+\Delta t}_{i,j,k}=F^{**}_{i,j,k}-\Delta t\frac{\partial wF}{\partial z} \tag{3.11}$$

Fluxes across the cell faces can be approximated using the donor-acceptor schemes introduced by Nichols et al. (1980) and Torey et al. (1985). The scheme proposed by the latter is a modified version of the former one and estimates the *F*-function fluxes, for example in the longitudinal direction, as:

$$u_{i+1/2,j,k}F_{i+1/2,j,k}\Delta t=sign\left(u_{i+1/2,j,k}\right)\times\min\left(F_{AD}\left|u_{i+1/2,j,k}\Delta t\right|+CF,F_{D}\Delta x_{D}\right) \tag{3.12}$$

where

$$CF=\max\left(\left[F-F_{AD}\right]\left|u_{i+1/2,j,k}\Delta t\right|-\left[F-F_{D}\right]\Delta x_{D},0\right) \tag{3.13}$$

and F_D is the F-function value of the donor cell which is always upstream of the face under consideration and can be determined according to the flow direction (note that in the staggered grid the flow direction is determined based on the calculated velocity vector at the cell face), F_A is the F-function value of the acceptor cell which is always downstream, F =max(F_D,F_{DM},0.1), F_{DM} is the F-function value of the cell upstream of the donor cell, Δx_D is the grid size of the donor cell in the longitudinal direction, and F_{AD} is a cell face value of F-function which can be either F_D or F_A. When the donor cell is a cell full of fluid $F_{AD}= F_D$, whereas if the donor cell is a surface cell then F_{AD} is determined by inspecting whether the convection of fluid in the donor cell across the cell face is primarily normal or tangential to the fluid interface. $F_{AD}= F_A$ when the convection is primarily normal to the surface, while $F_{AD}= F_D$ when the convection is primarily tangential to the surface. Furthermore, if the acceptor cell or the *DM* cell is a cell occupied by air (E cell), then $F_{AD}= F_A$. To determine whether the convection is more normal or tangential to the water surface, the biggest normal vector component of the surface cell is taken as the surface orientation. Therefore, it is necessary to define the free surface orientation. Next sub-section describes the method used to determine the free surface direction.

3.3.2 Reconstruction Method

The Youngs (1982) reconstruction method is used to determine the direction of the water surface in surface cells. The direction of water surface must be estimated in order to solve the advection scheme and also to choose an appropriate neighbor cell to determine the boundary values of pressure on the water surface boundary. In other words, the calculated pressure of the neighbor cell, which must be a fluid cell, is used to compute the pressure of surface cells as is explained in the next section.

Available reconstruction methods can be typically categorized into piecewise constant and piecewise linear/planar methods. Piecewise constant methods represent the water surface using a horizontal or vertical line/plane aligned with the coordinate system. Piecewise linear/planar methods adopt the idea that a normal vector, $\mathbf{m}=m_x i+m_y j+m_z k$, determines a linear/planar surface cutting the cell. Fig. 3.2 shows an example of a 2-D reconstructed surface using piecewise linear and piecewise constant methods. The piecewise linear/planar reconstruction method is applied to the present model. In the 3-D computational domain, the interface of each surface cell is represented by a unique plane as follows:

$$m_x x + m_y y + m_z z = B \tag{3.14}$$

where m_x, m_y, and m_z are the normal vector components in x, y, and z directions of a Cartesian coordinate system, respectively, and B is the plane constant. The normal vector and the plane constant must be calculated in such a way that the cut volume under the planar surface be equal to the multiplication of F-function and the volume of computational cell.

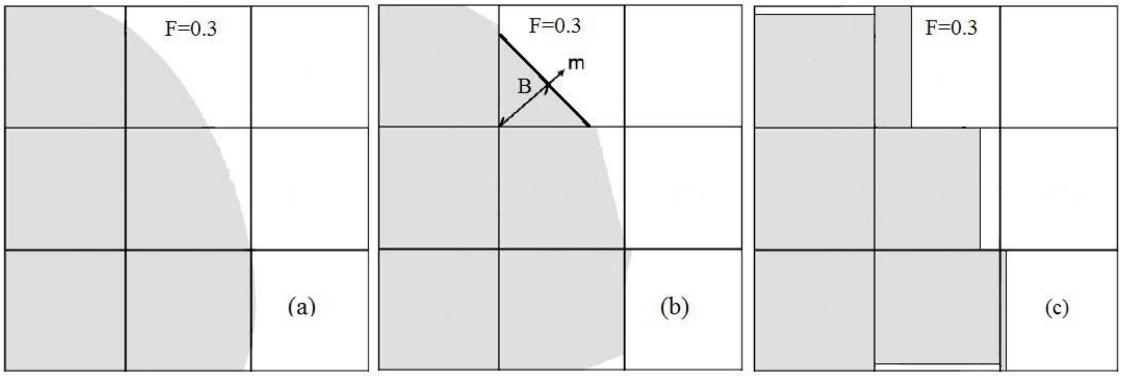

Fig. 3.2 (a) exact (b) piecewise linear and (c) piecewise constant 2-D reconstructed free surface

The present model estimates the normal vector using the Youngs (1982) method. This method was first introduced for 2-D problems (also see Aulisa et al., 2007). The orientation of the normal vector is evaluated as the gradient of F-function. In a 3×3×3 symmetric stencil, the normal vector is first estimated on all vertices of the central cell, as shown in Fig. 3.3, and then the cell-centered normal vector is obtained by averaging the normal vectors computed at the vertices. The normal components of a vertex, for example the vertex (i+1/2, j+1/2, k+1/2), is estimated as

$$m_x = \frac{\overline{F}_i - \overline{F}_{i+1}}{\Delta x},\ m_y = \frac{\overline{F}_j - \overline{F}_{j+1}}{\Delta y},\ m_z = \frac{\overline{F}_k - \overline{F}_{k+1}}{\Delta z} \tag{3.15}$$

where, for example, $\overline{F}_i = \left(F_{i,j,k} + F_{i,j+1,k} + F_{i,j,k+1} + F_{i,j+1,k+1}\right)/4$.

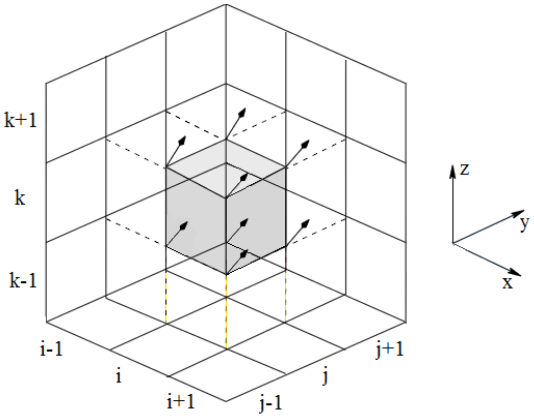

Fig. 3.3 Normal vectors of vertices in a 3×3×3 Youngs' stencil

The estimated normal vector is used in the advection scheme and also to identify the neighbor cell of each surface cell in order to define the pressure of the surface cells which is elaborated in Section 3.4. Although it is not necessary but the developed model is able to compute the plane constant B, which is a parameter related to the smallest distance from the origin of the cell under consideration. Scardovelli and Zaleski (2000) proposed a forward and inverse analytical approach for computing the plane constant based on the local fractional volume and the estimated normal vector. In their 3-D forward approach, the volume below a planar surface is computed as:

$$V=\frac{1}{6m_1m_2m_3}\left[B^3-\sum_{i=1}^{3}f_3\left(B-m_i\Delta x_i\right)+\sum_{i=1}^{3}f_3\left(B-B_{\max}+m_i\Delta x_i\right)\right] \tag{3.16}$$

where V is the cut volume under the free surface, m_i (i=1,2,3) are the normal vector components in x, y, and z directions, respectively, $B_{\max}=\sum_{i=1}^{3}m_i\Delta x_i$, and the function $f_n(s)$ is:

$$f_n(s)=\begin{cases} s^n & for\ \ s>0 \\ 0 & for\ \ s\le 0 \end{cases} \tag{3.17}$$

A standard root-finding approach, such as bisection or Newton's method, can be used to iteratively find the particular value of B for a given value of the cut volume V based on Eq. (3.16). Instead, one can also use the inverse analytical approach suggested by Scardovelli and Zaleski (2000), which usually is computationally cheaper. In the inverse method, the plane constant is calculated directly from the given cut volume and normal vector in a surface cell as follows:

$$\begin{cases} B=\sqrt[3]{6m_1m_2m_3V} & for\ \ 0\le V<V_1 \\ B=0.5\left(m_1+\sqrt{m_1^2+8m_2m_3\left(V-V_1\right)}\right) & for\ \ V_1\le V<V_2 \\ P(B)=a_3'B^3+a_2'B^2+a_1'B+a_0'=0 & for\ \ V_2\le V<V_3 \\ P(B)=a_3''B^3+a_2''B^2+a_1''B+a_0''=0 & for\ \ V_{31}\le V\le 0.5 \\ B=m_3V+\dfrac{m_{12}}{2} & for\ \ V_{32}\le V\le 0.5 \end{cases} \tag{3.18}$$

where $m_{12}=m_1+m_2$, $m=min(m_{12},m_3)$, $V_1=m_1^2/\max\left(6m_2m_3,epsilon\right)$ with $epsilon$ being an arbitrary small number, $V_2=V_1+\left(m_2-m_1\right)/2m_3$, and $V_3=V_{32}=m_{12}/2m_3$ when $m=m_{12}$ or $V_3=V_{31}=\left[m_3^2\left(3m_{12}-m_3\right)+m_1^2\left(m_1-3m_3\right)+m_2^2\left(m_2-3m_3\right)\right]/\left(6m_1m_2m_3\right)$ when $m=m_3$. The coefficients of the two cubic polynomials are $a_3'=-1$, $a_2'=3m_{12}$, $a_1'=-3\left(m_1^2+m_2^2\right)$,

$a_0' = m_1^3 + m_2^3 - 6m_1m_2m_3V$, $a_3'' = -2$, $a_2'' = 3$, $a_1'' = -3\left(m_1^2 + m_2^2 + m_3^2\right)$, and $a_0'' = m_1^3 + m_2^3 + m_3^3 - 6m_1m_2m_3V$. Note that Eq. (3.18) only summarizes the analytical solution of the inverse problem and more logical details can be found in the original work. The inverse method is applied to the present model.

3.4 Boundary Conditions

Accurate solution of discretized governing equations can be obtained by using appropriate boundary conditions. Basically, there are two types of boundary conditions: Dirichlet and Neumann conditions. The Dirichlet boundary condition specifies the variables at the boundary by predefined values. The Neumann boundary condition prescribes the gradient normal to the boundary. In the following sub-sections, boundary conditions applied to inlet, outlet, and solid walls are presented. In addition, special boundary conditions are described on the water surface.

3.4.1 Inlet Boundary Condition

The pressure of the inlet cells are defined using the Neumann condition with zero gradient. For supercritical flow, the water surface elevation at inlet needs to be defined and in turn the *F*-function is specified accordingly. Predefined velocity should be assigned to inlet cells.

3.4.2 Outlet Boundary Condition

The Neumann condition with zero gradient is used to determine the boundary values of pressure and velocity. For supercritical flow or free outflow, the water surface elevation and therefore the *F*-function at outlet is a copy of adjacent interior cells. For subcritical flow, the water surface elevation is given and in turn the F-function is specified accordingly at outlet cells.

3.4.3 Solid Wall Boundary Condition

Solid walls are considered as impenetrable boundaries such that the velocity normal to the boundary is set equal to zero and the tangential velocities can be defined using either the no-slip or free-slip conditions. In free-slip condition the boundary is frictionless and the fluid velocity on the solid boundary is equal to the velocity of the interior neighbor cell. No-slip condition states that the fluid velocity at the solid boundary is zero relative to the boundary. The bed and solid wall friction is considered by adding the bed shear stress in the momentum equations integrated over the near-bed control volumes. The bed shear stress is determined with

$$\boldsymbol{\tau}_{bi} = \rho C_{fb} \mathbf{u}_i U \tag{3.19}$$

where C_{fb} is the bed friction coefficient and $U = \sqrt{u^2 + v^2}$. The bed friction coefficient can be calibrated using measured data. For the test cases presented in this chapter, which the flume beds are made of smooth materials, the friction coefficient C_{fb} is specified equal to 0.001.

Similar to inlet and outlet boundaries the pressure of solid walls is calculated using the Neumann condition. The zero gradient condition is used to determine the *F*-function.

3.4.4 Water Surface Boundary Condition

Special boundary conditions are required for surface cells. The pressure in a surface cell is calculated by interpolation (or extrapolation) between the pressures at the water surface (the atmospheric pressure) and a neighbor fluid cell as follows:

$$p_{i,j,k} = (1-\eta) p_n + \eta p_s \tag{3.20}$$

$$p_s = p_a + 2\mu \frac{\partial w}{\partial z} \tag{3.21}$$

where P_n is the pressure in the neighbor fluid cell, P_s is the water surface pressure, P_a is the atmospheric pressure, and η is a coefficient illustrated in Fig. 3.4(a). The neighbor cell is chosen using the direction of water surface. The second term in Eq. (3.21) can be neglected.

The velocity component between a surface cell and an empty cell can be calculated using two different methods. In the first method, the divergence of every surface cell is set to zero. In other words, conservation of mass is applied in each Cartesian direction. The second method determines the boundary velocities by linear or constant extrapolating interior velocities. Fekken (2004) showed that the second approach provide a smooth behavior of the velocities near the free surface. Therefore, the second approach with constant extrapolation is adopted herein. The interior velocities are taken from the neighbor cell. For instance, consider the central cell (with *F*=0.2) shown in Fig. 3.4(b) which is surrounded by two empty cells. The velocity components across the right and top faces are specified using the known velocity components of the neighbor cell located below the bottom face.

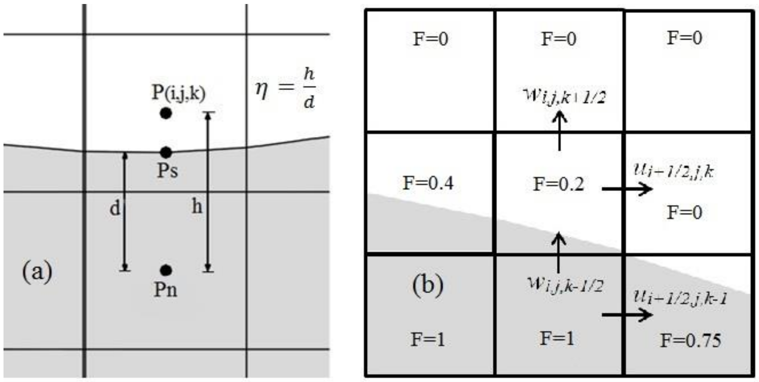

Fig. 3.4 (a) Definition of parameters used in the pressure interpolation of the surface cells and (b) free surface velocity components (2-D view)

3.5 Model Stability

Since the governing equations are solved explicitly, the computational time step should be limited by the stability conditions. The time step is restricted by the Courant-Friedrichs-Lewy (CFL) condition that prevents the mass and momentum to advect more than one cell in a single time step. Furthermore, a Courant-type restriction proposed by Weymouth and Yue (2010) is taken into account to assure that the time evolution of *F*-function does not overfill or over-empty the computational cells in each time step. Therefore, the stability condition can be written as follows:

$$\Delta t < \min\left[\left|\frac{\Delta x_i}{u_i}\right|, \frac{1}{2}\sum\left|\frac{\Delta x_i}{u_i}\right|\right] \tag{3.22}$$

The first term on the right side of the inequality (3.22) is the CFL condition and can be restricted by a constant coefficient between zero and one, which is chosen to be 0.2 in the present study. The second term is the *F*-function stability condition. Depending on the constant coefficient used to restrict the CFL condition, either CFL or VOF condition can be the dominant stability condition to control the time step. In this study the VOF condition was found as the dominant stability condition.

3.6 Computational Procedure

Shown in Fig. 3.5, the solution procedure of the present model starts with generating an appropriate computational grid for the entire physical domain. The computational grid adopted by the model is the rectilinear structured mesh with constant or variable grid spacing in the Cartesian coordinate system. It is also necessary to provide the initial conditions in the first step. The second step includes the turbulence model and calculates the eddy viscosity using the Smagorinsky sub-grid model. The RANS equations are solved in the third step using the calculated variables from the previous time step as an initial guess. Since the calculated velocity field may not satisfy the continuity equation, the SOR method is used in the next step to correct the pressure and velocity fields such that the free divergence can be obtained from the continuity equation. The advection equation of F-function is solved in step 5 and the new F-function field is used to reconstruct the interface of surface cells in step 6. The estimated normal vector of the interface provides the orientation of the free surface in each surface cell. In step 7, the new time step is calculated using the stability conditions of the model and then the new computations start from the second step. This procedure continues until the elapsed time reaches the predefined simulation time.

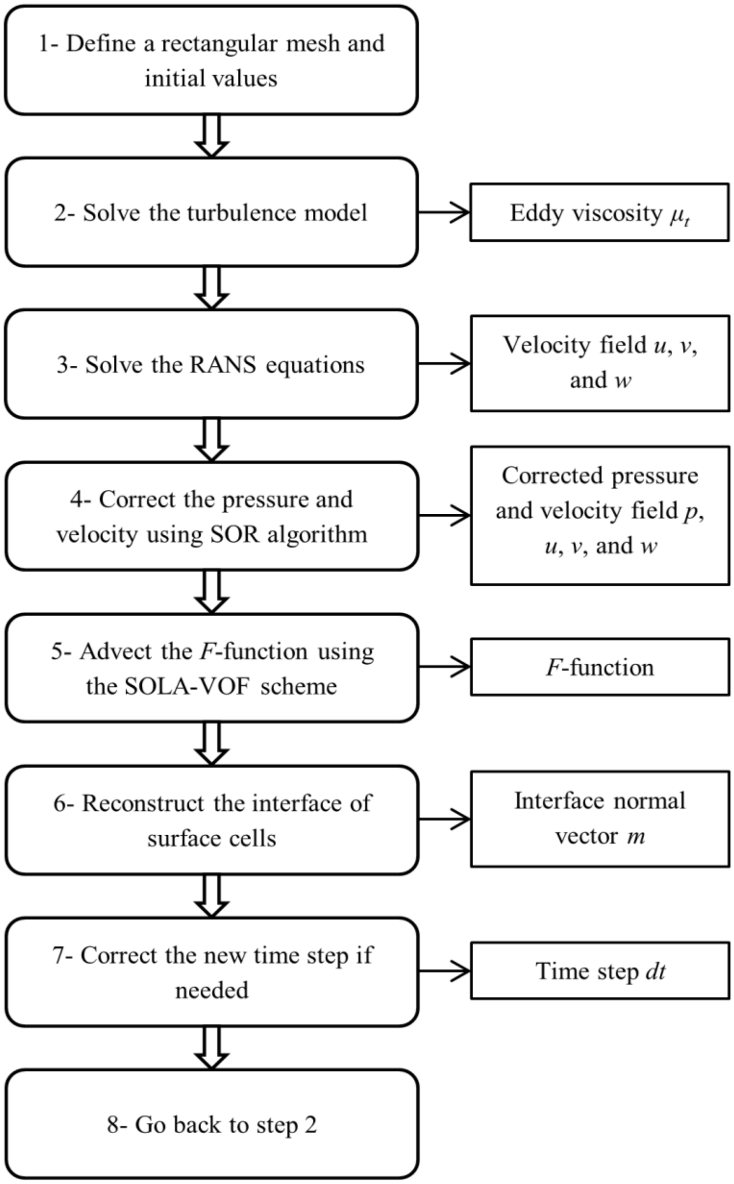

Fig. 3.5 Solution steps of the present model

3.7 Model Test

The developed 3-D finite-difference model has been tested using five laboratory experiments of dam-break flow. The first three cases concern the initial stages of 2-D dam-break flows over dry and wet flat beds and a dry bed with a rectangular obstacle. The other two cases investigate 3-D dam-break flows due to partial dam break and over an obstacle. The simulation results are presented in the following sub-sections.

3.7.1 Initial Stage of Dam-Break Flow over a Wet Flat Bed

The first case aims to investigate the ability of the present model to simulate the initial stage of dam-break flow over a wet bed. The experiment was conducted by Stansby et al. (1998) in a flume 15.24 m long, 0.4 m wide, and 0.4 m high with a flat bed. The gate was located 9.76 m downstream of the upper flume end. The initial water depth in the reservoir, h_0, was 10 cm and the downstream depth was 4.5 cm. A fine computational grid spacing equal to 0.75 cm is used in the model. In the experiment, A 7 kg weight attached to a wire rope was used to pull up the gate rapidly. To investigate the effects of non-instantaneous gate removal, the simulations used two gate removal scenarios: instantaneous and gradual lift. In the gradual lift of the gate, it was assumed that the gate is pulled up in 0.1 s, which is shorter than $1.25(h_0/g)^{0.5}$ recommended by Lauber and Hager (1998). Here, g is the acceleration due to gravity. Fig. 3.6 compares the measured and calculated water surface profiles at several initial instants after dam break. Spatial scales are normalized by h_0, and $x/h_0=0$ corresponds to the gate location. One can see the effects of the gradual lift of the gate on the wave speed. The front wave propagates slightly faster when the gate is lifted instantaneously. This is perhaps because of the fact that when the gate is released instantaneously the potential energy (due to gravity) of the entire water column becomes kinetic energy, whereas in the gradual gate release this process takes place gradually. The wave shape is relatively the same for both scenarios. The water surface profiles calculated by both scenarios are generally in a good agreement with the measured ones.

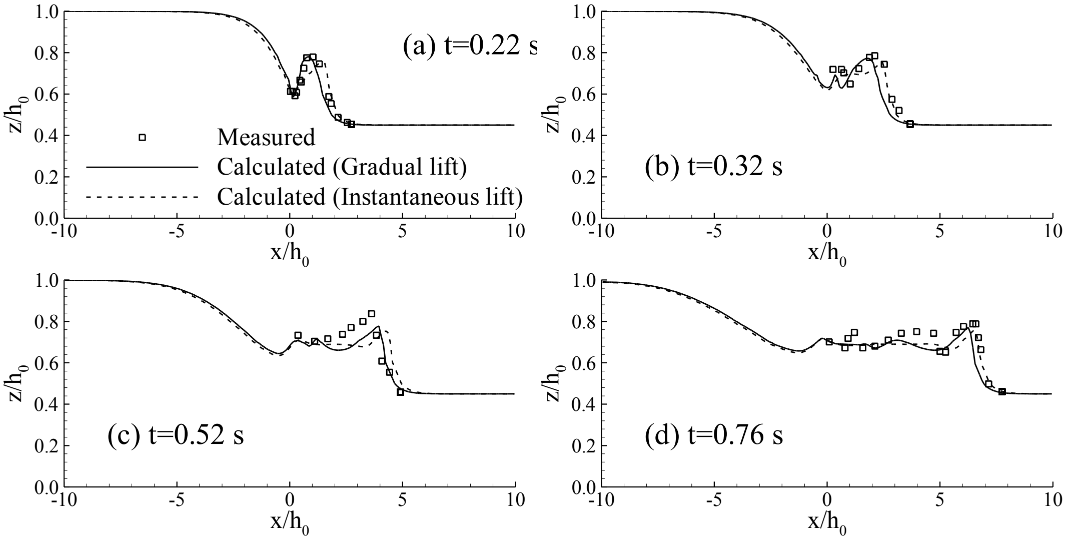

Fig. 3.6 Measured and calculated water surface profiles caused by dam break over wet bed (measurements from Stansby et al., 1998)

3.7.2 Initial Stage of Dam-Break Flow over a Dry Flat Bed

The second test is the initial stage of dam-break flow over a dry bed. The experiment was carried out by Kocaman (2007) and the data published by Ozmen-Cagatay and Kocaman (2010). The laboratory flume was 9 m long, 0.3 m wide, and 0.34 m high. The gate was located 4.65 m from the upstream flume end. The computational grid spacing is 0.75 cm. Similar to the previous case with a downstream wet bed, the dam breaking process was simulated by instantaneous and gradual dam removal scenarios. Fig. 3.7 shows a good agreement between the measured and calculated water surface profiles at several instants. It is observed that the gradual dam removal does not affect the calculated results in the dry bed case. Note that spatial scales are normalized by h_0, and $x/h_0=0$ corresponds to the gate site.

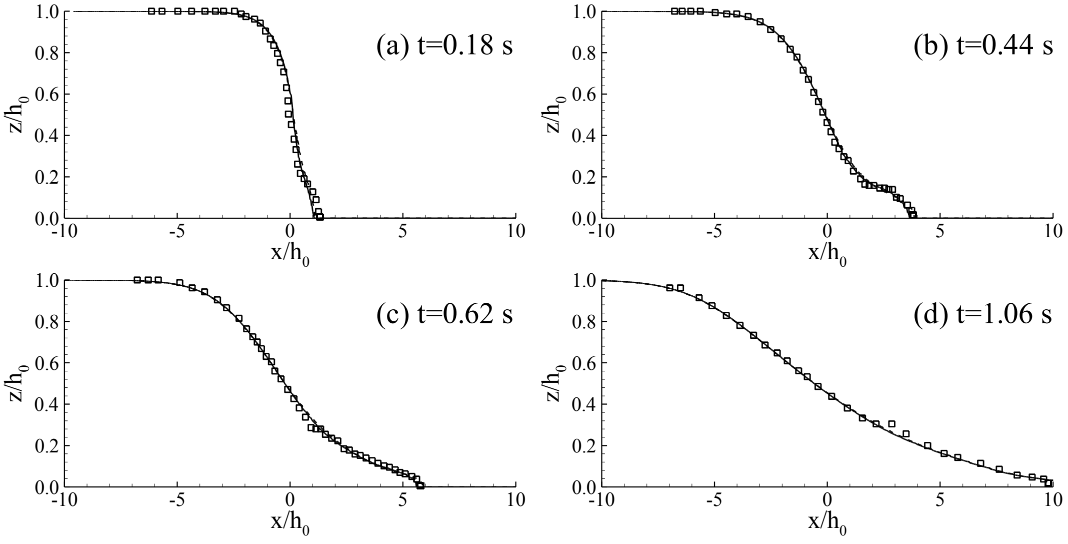

Fig. 3.7 Measured and calculated water surface profiles caused by dam break over dry bed (legend similar to Fig. 3.6, measurements from Ozmen-Cagatay and Kocaman, 2010)

3.7.3 Initial Stage of Dam-Break Flow over a Rectangular Obstacle

The third case investigates the initial stage of 2-D dam-break wave over a dry bed with a rectangular obstacle downstream of the dam. Experiments were conducted by Oertel and Bung (2012) in a rectangular flume that was 22 m long, 0.30 m wide and 0.50 m high. A gate of thickness 0.015 m was installed at a distance of 13 m from the upstream end. Herein, the selected experiment included an initial water depth equal to 0.2 m in the reservoir and the downstream bed was dry. An obstacle of height 0.06 m was placed 0.2 m downstream of the gate. The dimensionless gate lift time, T, is 1.12. Here, $T=t(g/h_0)^{0.5}$. The computational grid spacing is equal to 0.5 cm.

Fig. 3.8 depicts the time evolution of dam-break wave observed in the physical model and calculated by the present numerical model. After the dam-break wave hits the obstacle, it is redirected and splashes upward. Then, the splash falls down, the wave overtops the obstacle and moves toward downstream. The numerical model is able to predict this process well, particularly the redirected splash height and shape. The model predicts a slower upward splashing and faster falling stage. This may be due to the appearance of air bubbles and water drops created by wave and obstacle collision, which makes the simulation of flow motion very complex at the initial stages.

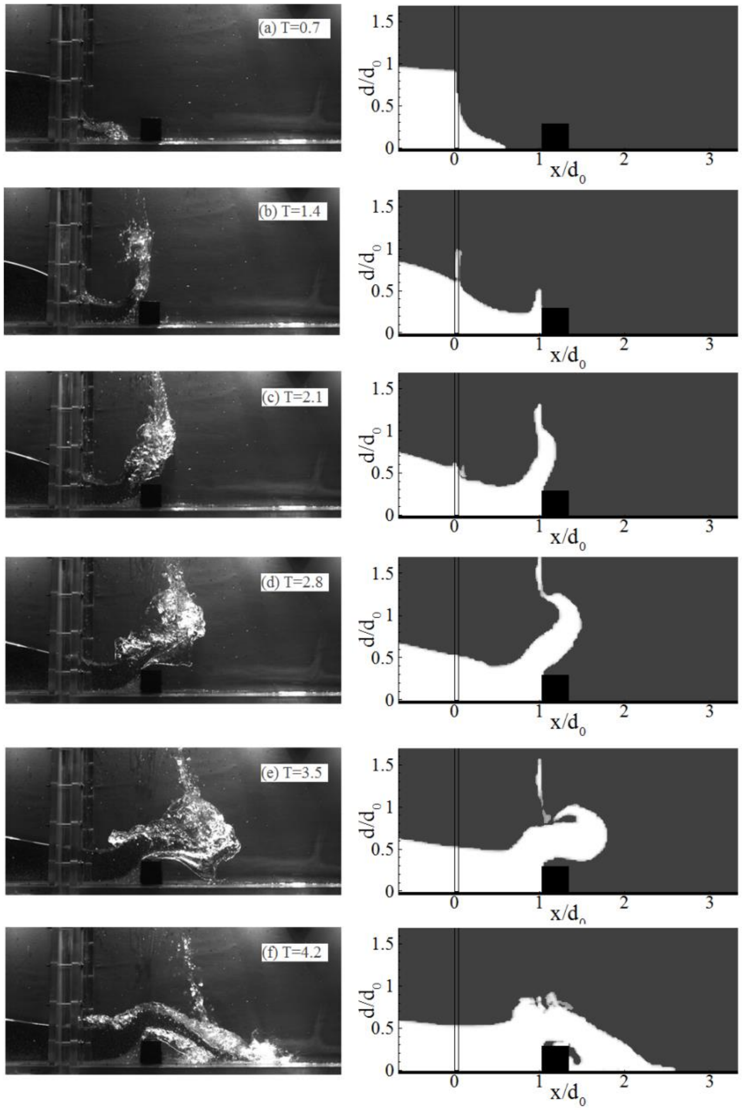

Fig. 3.8 Initial stages of dam-break wave over a rectangular obstacle (left: experimental images from Oertel and Bung, 2012 and right: present model results)

3.7.4 Partial Dam-Break Flow

The developed model is tested by a partial dam-break flow experiment conducted by Fraccarollo and Toro (1995) to simulate the dam-break flow in an open valley. The experiment was conducted in a 3 m long and 2 m wide flume, shown in Fig. 3.9. The partially broken dam was represented by two impervious vertical walls and a 0.4 m wide gate located between the walls, at 1 m from the upstream end of the flume. The downstream bed was dry with open boundaries. The breaking of the dam was simulated by the rotation of the gate on a fixed hinge in a very short lapse of time, less than 0.1 s, as shown in Fig. 3.10 (picture from Fraccarollo and Toro, 1995). The temporal evolution of water level, pressure, and velocity were measured at several gages sketched in Fig. 3.9. The gages G-5A, G-3A, and G-2A are placed inside the reservoir, G0 at the gate location, and G1A immediately downstream of the gate. These gages are located at 0.18, 0.58, 0.78, 1.0, and 1.02 m from the upstream end, respectively.

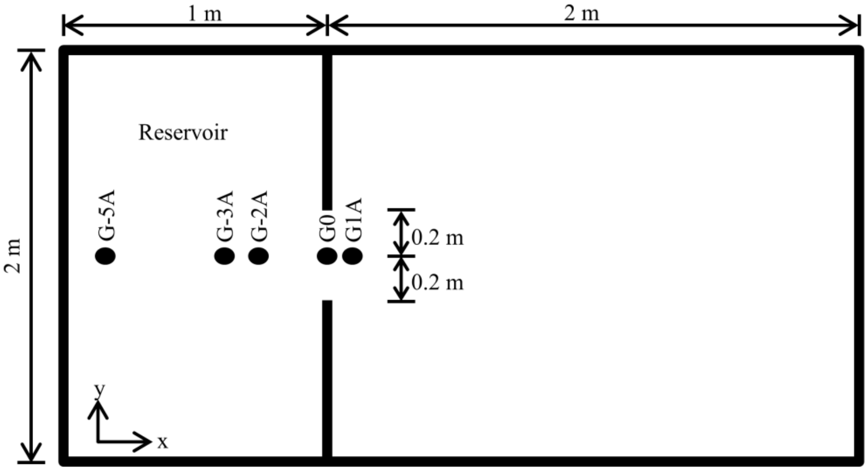

Fig. 3.9 Plan view of the partial dam-break experiment

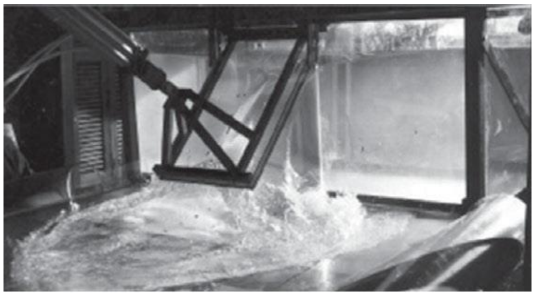

Fig. 3.10 Photograph of the experimental dam-break carried out by Fraccarollo and Toro (1995)

The computational domain is meshed by an equal grid spacing of 1.6 cm in the longitudinal, lateral, and vertical directions. Fig. 3.11 shows the snapshots of the calculated water surface at several elapsed times. The propagated wave at time 0.5 s shows a significant longitudinal crest on the free surface profile. The sharp crest was also observed in the experiment shown in Fig. 3.10. A spade-like flood downstream of the opening can be recognized in both calculated and observed results. These outcomes were also reported using a 3-D SPH model developed by Ferrari et al. (2010).

Fig. 3.12 shows the 2-D distribution of bottom pressure and longitudinal velocity near the bed at different instants. The bottom pressure inside the reservoir decreases with time. The pressure distribution on the bottom shows a spade-like evolution over time, which is consistent with time evolution of water level stated above. The pressure magnitude in front of the opening is larger than other spots downstream of the exit during the simulation. This is reasonable since the water surface level, as shown in Fig 3.10, is higher there. The velocity distribution reveals that the areas around the walls adjacent to the gate experience the velocity less than 0.2 m/s. Therefore, the impacts of the flood caused by the partial dam-break flow are insignificant on these areas.

Figs. 3.13(a)-(h) show a good agreement between the measured and calculated time series of the water surface level and pressure. Figs. 3.14(a)-(i) compare the time evolution of the flow velocity component in the longitudinal direction at gages G0, G-2A, and G-3A. The calculated velocities in the reservoir show a similar oscillatory behavior to the measured velocities. When the gate is opened, the progressive dam-break wave propagates downstream and a rarefaction wave propagates upstream into the reservoir. The rarefaction wave hits the upstream and side walls of the reservoir and generates reflected waves which cause the oscillatory pattern of flow velocity. The effects of the reflected waves on water surface can be also seen in Fig. 3.13.

The velocity time series shown in Fig. 3.14 reveal a phase lag between the measured and calculated velocities in which the calculated velocity reaches the peak value about 0.3 s prior to the measured one. Moreover, a discrepancy between measured and calculated peak velocities can be seen. These might be due to the rotational motion of the gate removal process in the experiment but a sudden removal of the gate in the numerical simulation. The adhesion of water to the gate causes an upward velocity boundary at the gate location which can affect the flow properties. The adhesion of water is not considered by the model. Another reason might be the existence of experimental errors. According to Fraccarollo and Toro (1995), the velocity was measured using a four quadrant electromagnetic velocity meter. The measurement instrument was supported by a rounded rod in order to avoid possible vibrations induced by the flow. Vibration of the rod and in turn experimental errors might be arisen by the gate rotation and reflected waves in the reservoir.

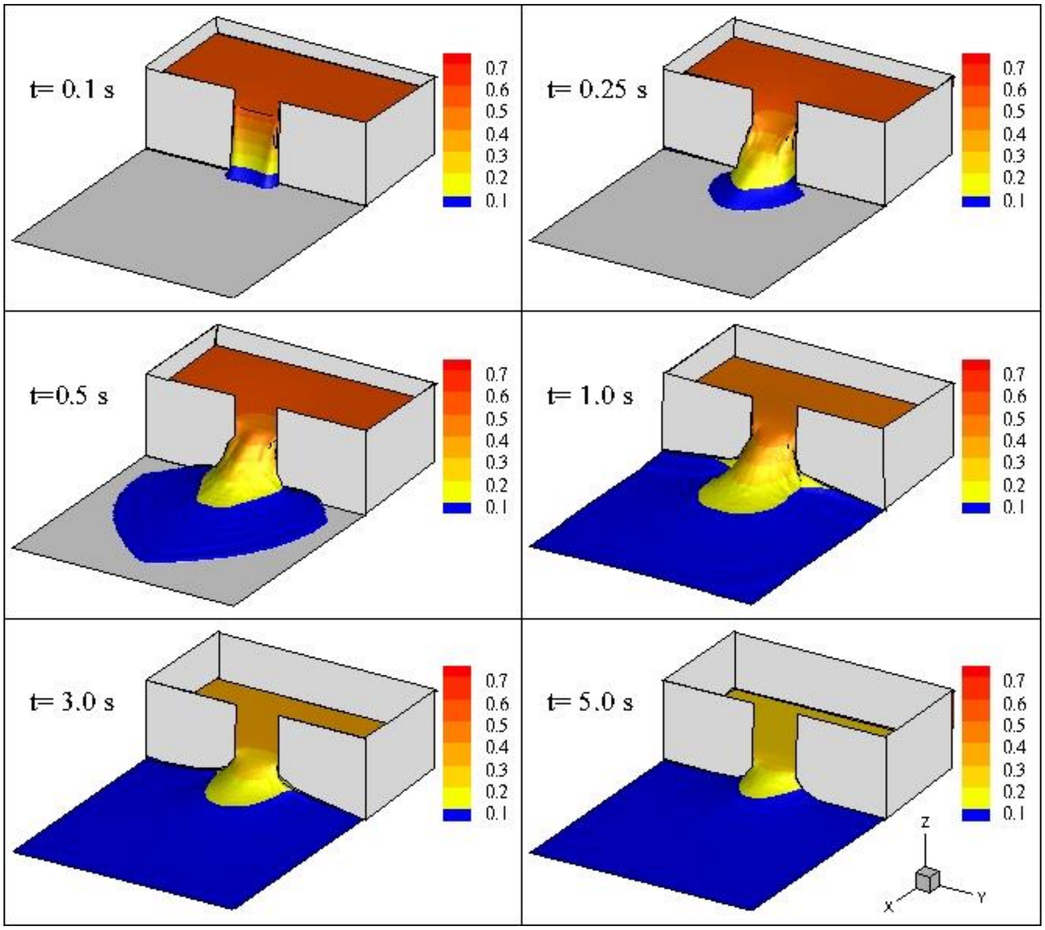

Fig. 3.11 3-D Snapshots of calculated water surface elevation

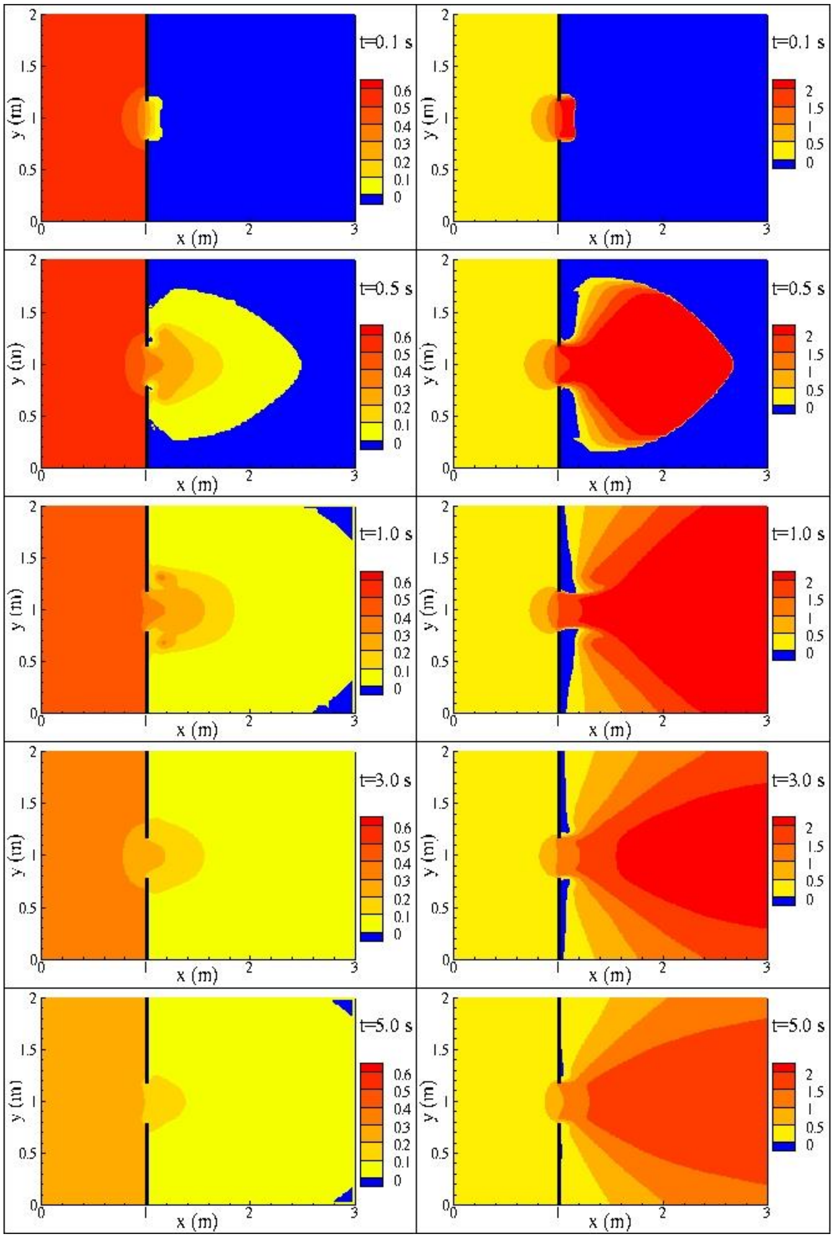

Fig. 3.12 2-D Snapshots of calculated bottom pressure and velocity (left: bottom pressure in m, and right: longitudinal velocity near the bed in m/s)

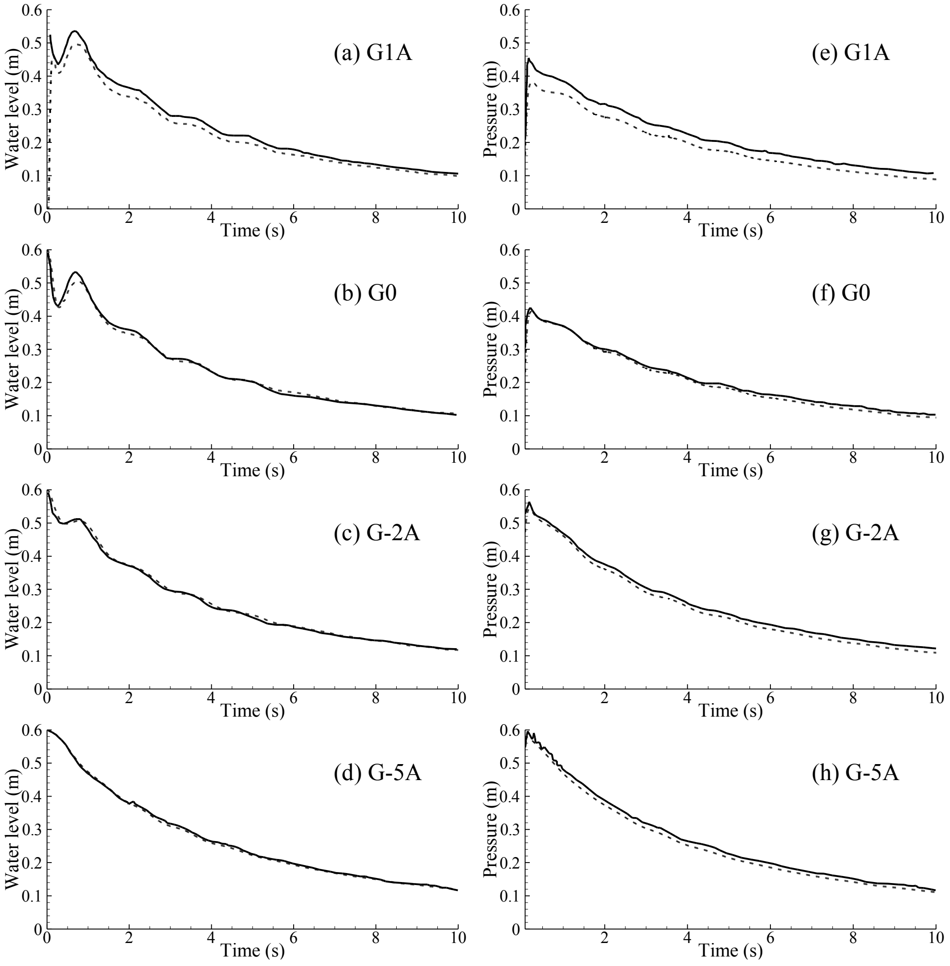

Fig. 3.13 (a)-(d): Measured (–) and calculated (---) water surface levels; (e)-(h): measured (–) and calculated (---) pressures at the bottom (measurements from Fraccarollo and Toro, 1995)

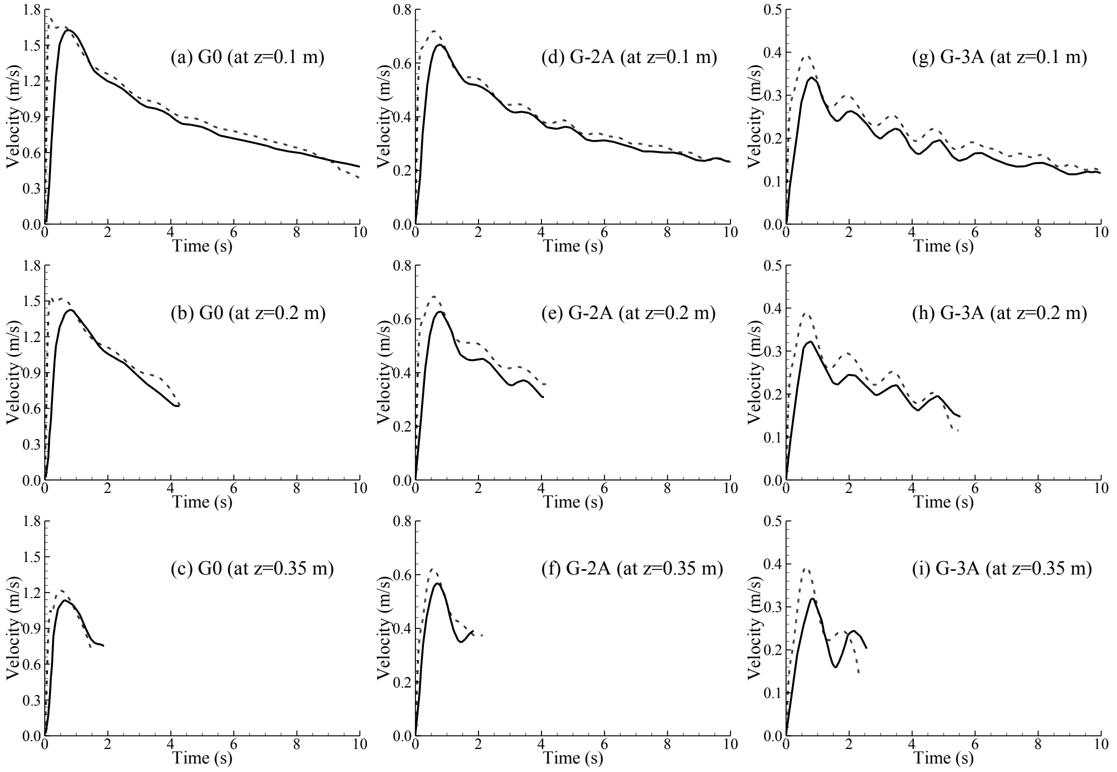

Fig. 3.14 Measured (–) and calculated (---) longitudinal velocities at 0.1, 0.2, and 0.35 m above the bed (measurements from Fraccarollo and Toro, 1995)

3.7.5 Dam-Break Flow over a Rectangular Block

A laboratory experiment of dam-break flow carried out at the Maritime Research Institute of the Netherlands (MARIN) (Kleefsman et al., 2005) is applied to test the model as the final case. The flume was 3.22 m long, 1 m wide, and 1 m high and a gate was placed 1.23 m from the upstream end. A rectangular block of 0.403×0.161×0.161 m was placed downstream of the reservoir. The initial water surface depth inside the reservoir was 0.55 m and the downstream region was dry. Fig. 3.15 shows the configuration of the tank and the location of measurement gages.

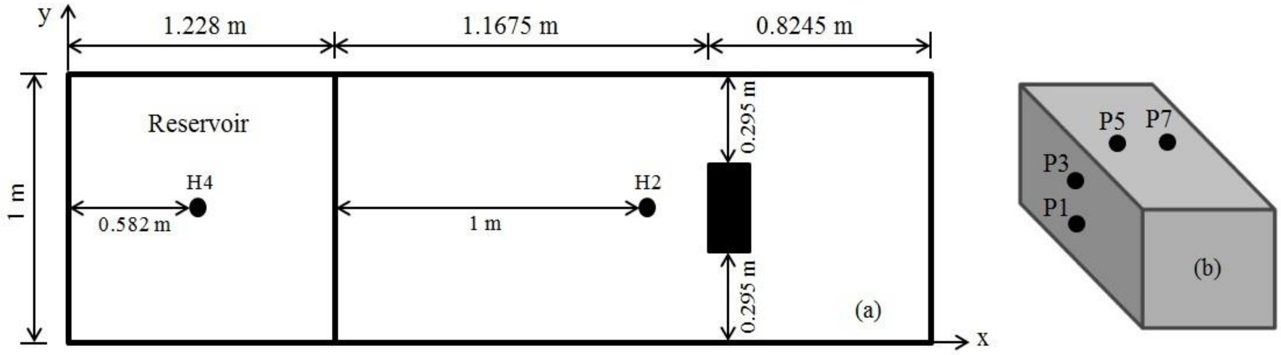

Fig. 3.15 Sketch of the MARIN dam-break experiment (H4 and H2: water surface level measurement gages; P1, P3, P5, and P7: pressure measurement gages around the block)

The computational grid consists of 161×50×50 cells. Fig. 3.16 shows 3-D views of wave front propagation and reflection during the simulation period. The initial water body in the reservoir and the obstacle located downstream of the reservoir are shown at *t*=0.0 s. Removing the gate, which separates the reservoir and the downstream flume, generates a wave propagating downstream monotonously. The progressive wave hits the obstacle and the downstream wall and is then reflected toward the upstream.

Fig. 3.17 compares the water surface time series at gages H2 and H4. The comparison shows similar patterns in the temporal evolution of measured and calculated water surface levels. The progressive wave front reaches gage H2 at *t*=0.4 s and the water surface level increases until *t*=2.4 s when the reflected wave from the obstacle and the downstream wall moves toward the upstream. This causes a decrease in the water surface level until the second reflected wave reaches the gage and the water level increases again. At gage H4, the water surface level decreases as the reservoir drains smoothly until *t*=2.9 s. At this time the first reflected wave reaches and approaches the upstream wall. The reflected wave hits the wall and the second reflected wave shows a peak level around *t*=3.9 s and propagates toward the downstream.

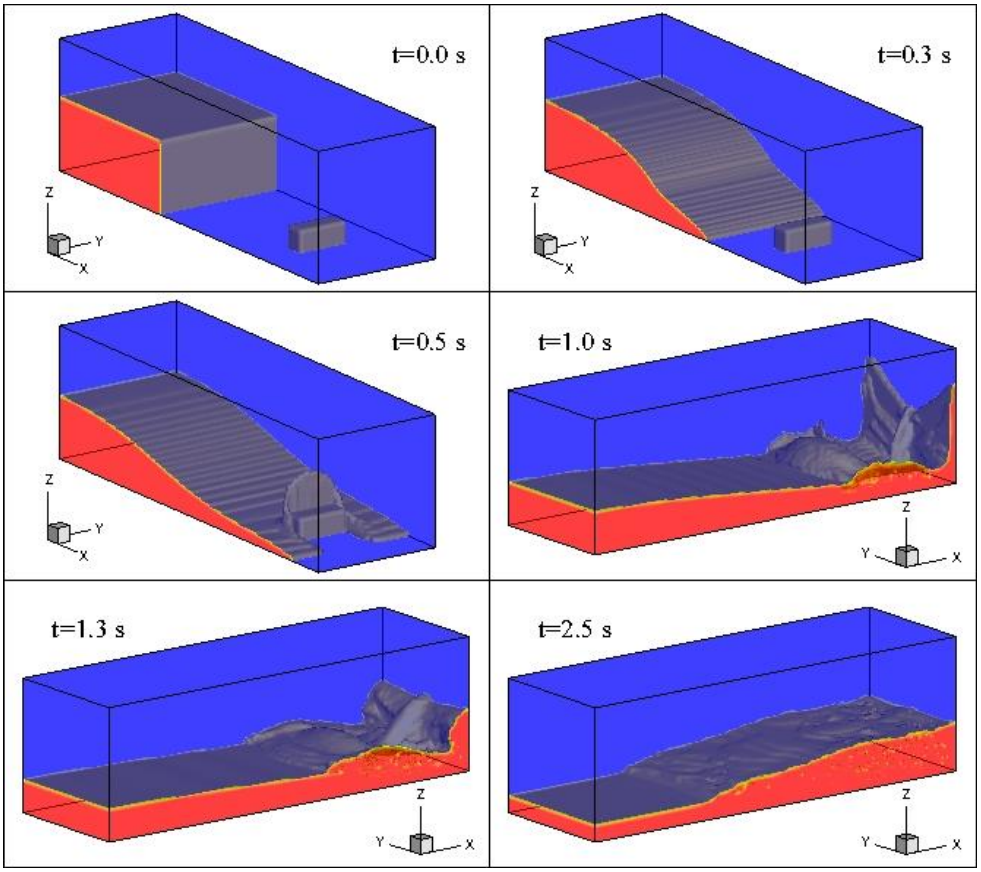

Fig. 3.16 3-D view of wave propagation process

The measured and calculated pressure time series at gages P1, P3, P5, and P7 are shown in Fig. 3.18. Both measurement and simulation show sudden increase in pressures at gages P1 and P3 when the wave hits the obstacle. The calculated pressures exhibit spurious spikes, particularly on gages P5 and P7. This is due to the appearance of air pockets in the water and the model has difficulty in handling an isolated empty cell surrounded by fluid cells. When the water enters the isolated empty cell, this cell becomes a fluid cell in one time step without being a surface cell in between. Since the free divergence condition was not satisfied by the empty cell in the previous time step, the sudden change from being an empty cell to a fluid cell results to a pressure peak over the calculated pressure field. Similar situation occurs in the model results of

Kleefsman et al. (2005). Nevertheless, the comparisons in Fig. 3.18 reveal the capability of the developed model to simulate the general pressure changes caused by the progressive and reflected waves.

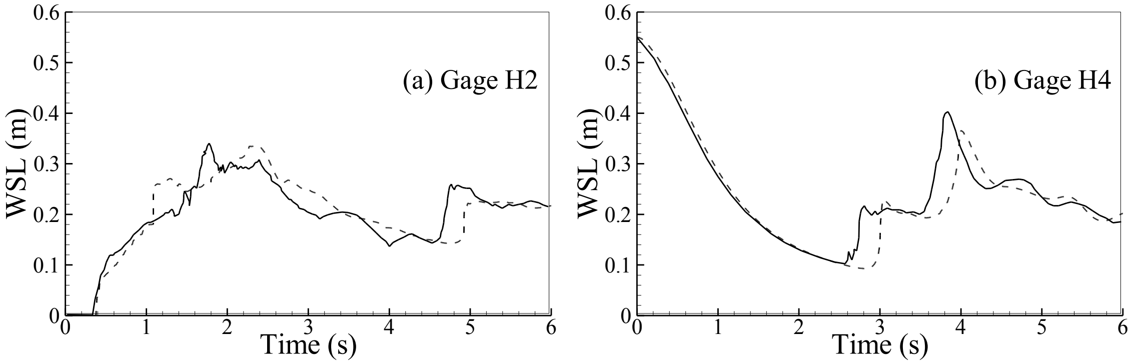

Fig. 3.17 Time evolution of water surface level: measured (–), calculated (---) (measurements from Kleefsman et al., 2005)

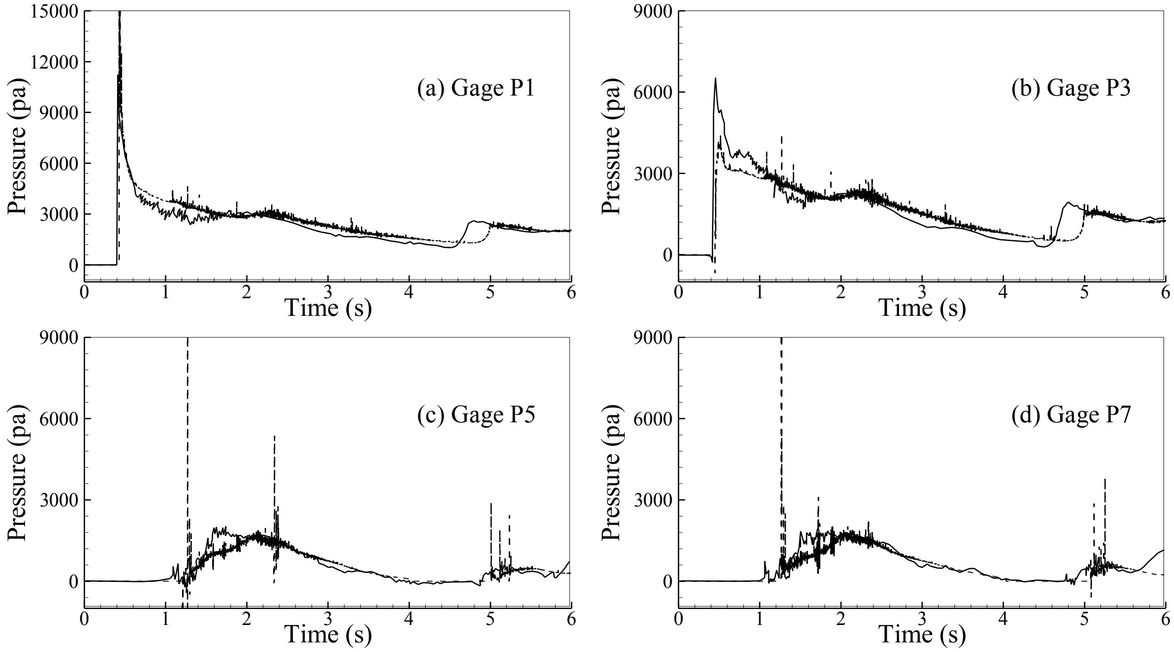

Fig. 3.18 Time evolution of pressure: measured (–), calculated (---) (measurements from Kleefsman et al., 2005)

3.8 Summary

In this chapter, the VOF interface tracking method was applied to develop a 3-D model of dam-break flows. The model solved the RANS equations in the Cartesian coordinate system using an explicit finite-difference method based on rectilinear, staggered grid. The convection and diffusion terms were discretized using the upwind and central difference schemes, respectively. The flow velocity field calculated from the RANS equations based on an assumed pressure were corrected using the SOR method to satisfy the continuity equation. The turbulent viscosity was calculated by means of the Smagorinsky sub-grid model. A VOF algorithm was adopted to track the free surface, including the SOLA-VOF scheme modified by Torey et al. (1985) to calculate F-function fluxes and the Youngs reconstruction method to estimate the normal vector of water surface and consequently the free surface orientation.

The model was tested by using five laboratory experiments, including 2-D dam-break flows over wet and dry flat beds and a dry bed with rectangular obstacle, and 3-D dam-break flows caused by a partial dam break and over an obstacle. The computed water surface evolutions and velocity and pressure distributions agree generally well with the measurements. The dam-break wave fronts over dry and wet flat beds, partial dam-break wave spreading, wave splash redirected by the obstacles and reflection from the solid walls are reasonably well reproduced by the model. The results revealed that the VOF method is an efficient tool to track the water surface elevation of dam-break waves.

CHAPTER 4

3-D FINITE-VOLUME MODEL OF DAM-BREAK FLOW OVER FIXED BEDS

In this chapter the governing equations, numerical solutions, and test results of a 3-D finite-volume model of dam break flows over irregular fixed beds are presented. The model solves the RANS equations using a finite-volume method on Cartesian coordinate system and collocated grids. The model is able to simulate dam-break flow on irregular beds since the computational mesh can fit on the bottom. The water surface tracking method is based on a method introduced by Ubbink and Issa (1999) for capturing sharp fluid interfaces on arbitrary-shaped meshes.

4.1 Governing Equations

Similar to the model described in the previous chapter, the governing equations are 3-D continuity and RANS equations for incompressible flows. The governing equations of flow in tensor form are:

$$\frac{\partial u_i}{\partial x_i} = 0 \tag{4.1}$$

$$\frac{\partial u_i}{\partial t} + u_j \frac{\partial u_i}{\partial x_j} = \frac{1}{\rho} f_i - \frac{1}{\rho}\frac{\partial p}{\partial x_i} + \frac{1}{\rho}\frac{\partial \tau_{ij}}{\partial x_j} \tag{4.2}$$

where x_i ($i=x,y,z$) are the components of the coordinate system, u_i are the components of the flow velocity, f_i are the components of the external forces, p is the pressure, ρ is the water density, and τ_{ij} (j=x,y,z) are the stresses defined as:

$$\tau_{ij} = \mu\left(\frac{\partial u_i}{\partial x_j} + \frac{\partial u_j}{\partial x_i}\right) \tag{4.3}$$

where μ is the viscosity which includes molecular, μ_m, and turbulent, μ_t, viscosities. The molecular viscosity of water is equal to 10^{-3} Ns/m^2 and the turbulent viscosity is determined using the Smagorinsky (1963) sub-grid model described by Eq. (3.4).

The governing equations can be also written as follows:

$$\nabla \bullet \mathbf{u} = 0 \tag{4.4}$$

$$\frac{\partial \mathbf{u}}{\partial t} + \nabla \bullet (\mathbf{uu}) = -\frac{1}{\rho}\nabla p + \frac{1}{\rho}\mathbf{f} + \frac{1}{\rho}\nabla \bullet \boldsymbol{\tau} \tag{4.5}$$

Eq. (4.4) can be used to simplify the stress tensor relation, Eq. (4.3), and consequently the momentum equation as:

$$\frac{\partial \mathbf{u}}{\partial t} + \nabla \bullet (\mathbf{uu}) = -\frac{1}{\rho}\nabla p + \frac{1}{\rho}\mathbf{f} + \frac{1}{\rho}\nabla \bullet (\mu \nabla \mathbf{u}) \tag{4.6}$$

Eqs. (4.4) and (4.6) are the flow governing equations in Cartesian coordinate system.

As described in Chapter 3, the advection of F-function in VOF method is governed by Eq. (3.10) which can be rewritten as follows:

$$\frac{\partial F}{\partial t} + \nabla \bullet (F\mathbf{u}) = 0 \tag{4.7}$$

4.2 Computational Grid

The governing equations are discretized using a finite-volume method. The computational cells are numbered in an unstructured index. To preserve the efficiency of the numerical solutions on irregular unstructured grids, the collocated or non-staggered approach is used, which stores all primary variables at the center points and fluxes at the faces of computational cells. This approach simplifies the computer programming and minimizes the amount of geometrical information required at each computational cell.

The computational domain is represented by a mesh of hexahedral cells that fits the solid boundaries, such as bed. Each cell is embraced by flat faces. Fig. 4.1 shows the 3-D sketch of a hexahedral cell where point P is the center of the control volume under consideration and point N is the center of a neighbor cell. Vector **A** is the outward-pointing face area vector normal to the face located between cell P and N. Vector $\mathbf{d} = \overrightarrow{PN}$ shown in Fig. 4.1 as the dashed line connects points P and N. Vector **d** does not necessarily go through the centroid of the cell face where vector **A** starts. The angle between vectors **A** and **d** determines if the mesh is orthogonal or non-orthogonal. The mesh is defined as non-orthogonal if the angle is not zero. The orthogonality and non-orthogonality of faces are taken into account by over-relaxed approach proposed by Jasak (1996) and applied by Ubbink (1997), in which vectors **D** and **K** are introduced as follows:

$$\mathbf{D} = \frac{\mathbf{d}}{\mathbf{d} \bullet \mathbf{A}} \left|\mathbf{A}\right|^2 \tag{4.8}$$

$$\mathbf{K} = \mathbf{A} - \mathbf{D} \tag{4.9}$$

where orthogonality means that **K** is equal to zero.

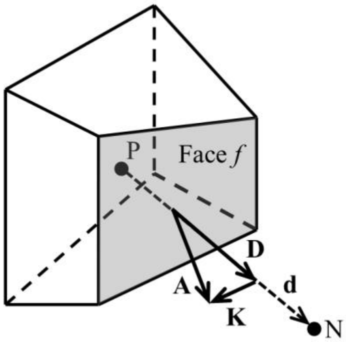

Fig. 4.1 Sketch of a hexahedral computational cell (points P, N, and face centroid may not necessarily make a straight line)

In order to mesh a physical domain with irregular beds, the computational grid is generated in two steps. First, a 2-D horizontal mesh, which fits on the bed surface boundary, is generated. The horizontal mesh contains quadrilateral cells with edges parallel to the coordinate axes x and y. The average longitudinal and lateral slopes of the cell face are calculated using the bed elevation at the center points of cell edges. The second step is meshing the domain in the vertical direction. This is accomplished by copying the 2-D horizontal mesh in the vertical direction. The number of vertical layers depends on the grid spacing in z direction. The horizontal mesh and vertical layers of the computational domain adopt constant and varying grid spacing.

4.3 Numerical Solutions of Continuity and RANS Equations

In the finite-volume method the governing equations are integrated in each computational cell. The divergence theorem can be used to integrate terms which contain vector divergence and scalar gradient. The divergence theorem, more commonly known, especially in older literature, as Gauss's theorem, defines the volume integral of the divergence of an arbitrary vector $\boldsymbol{\varphi}$ as:

$$\int_V (\nabla \bullet \boldsymbol{\varphi}) dV = \oint_S \boldsymbol{\varphi} \bullet d\mathbf{S} \tag{4.10}$$

where V is the volume of the control volume and S is the surface boundary of the control volume. Eq. (4.10) can be written for a control volume with n faces as follows:

$$\int_V (\nabla \bullet \boldsymbol{\varphi}) dV = \sum_{f=1}^{n} \mathbf{A}_f \bullet \boldsymbol{\varphi}_f \tag{4.11}$$

where subscript f is the face number and variables with index f determine the values on the face. Similarly, for an arbitrary scalar variable φ we have:

$$\int_V (\nabla\varphi) dV = \sum_{f=1}^{n} \mathbf{A}_f \varphi_f \tag{4.12}$$

A second-order accurate approximation of the gradient of flow properties can be calculated based on Eqs. (4.11) and (4.12) as follows:

$$\left(\nabla\bullet\boldsymbol{\varphi}\right)_P = \frac{1}{V_P}\sum_{f=1}^{n} \mathbf{A}_f \bullet \boldsymbol{\varphi}_f \tag{4.13}$$

$$\left(\nabla\varphi\right)_P = \frac{1}{V_P}\sum_{f=1}^{n} A_f \varphi_f \tag{4.14}$$

In the next sub-sections the discretized form of momentum equation is explained first and then the pressure equation is derived based on the continuity equation. The discretization approach of the pressure equation is also described in detail.

4.3.1 Discretization of Momentum Equation

The momentum equation (4.6) can be integrated over the control volume as:

$$\int_V \frac{\partial \mathbf{u}}{\partial t} dV + \int_V \nabla\bullet\left(\mathbf{u}\mathbf{u}\right) dV = -\frac{1}{\rho}\int_V \left(\nabla p\right) dV + \frac{1}{\rho}\int_V \mathbf{f}\, dV + \frac{1}{\rho}\int_V \nabla\bullet\left(\mu\nabla\mathbf{u}\right) dV \tag{4.15}$$

Integrating the temporal, pressure gradient, and the external force terms over the control volume and using Eqs. (4.11) and (4.12) leads to:

$$V_P \frac{\partial \mathbf{u}}{\partial t} + \sum_{f=1}^{n}\left(\mathbf{A}_f \bullet \mathbf{u}_f\right)\mathbf{u}_f = -\frac{V_P}{\rho}\nabla p + \frac{V_P}{\rho}\mathbf{f} + \frac{1}{\rho}\sum_{f=1}^{n} \mathbf{A}_f \bullet \left(\mu\nabla\mathbf{u}\right)_f \tag{4.16}$$

The only external force that we consider is the gravitational body force, which on unit volume is $\rho\boldsymbol{g}$, where $\mathbf{g}$ is the vector acceleration of gravity. Also, by replacing the dynamic viscosity μ with the kinematic viscosity υ, Eq. (4.16) becomes:

$$V_P \frac{\partial \mathbf{u}}{\partial t} + \sum_{f=1}^{n} \left(\mathbf{A}_f \bullet \mathbf{u}_f \right) \mathbf{u}_f = -\frac{V_P}{\rho} \nabla p + V_P \mathbf{g} + \sum_{f=1}^{n} \mathbf{A}_f \bullet \left(\upsilon \nabla \mathbf{u} \right)_f \tag{4.17}$$

Discretization form of each term in Eq. (4.17) is presented in the next sub-sections.

4.3.1.1 Convection Term

The second term on the left side of Eq. (4.17) is the convection term. The dot product of face area vector and velocity vector determines the volumetric flux at the face, thus:

$$\sum_{f=1}^{n} \left(\mathbf{A}_f \bullet \mathbf{u}_f \right) \mathbf{u}_f = \sum_{f=1}^{n} Flux_f \mathbf{u}_f \tag{4.18}$$

To approximate the velocity at the face, several well-known upwinding schemes, including the first-order upwind scheme, hybrid upwind/center scheme and exponential difference scheme (Patankar 1980), are adopted by the model.

4.3.1.2 Diffusion Term

The diffusion term in Eq. (4.17) can be written as:

$$\sum_{f=1}^{n} \mathbf{A}_f \bullet \left(\upsilon \nabla \mathbf{u} \right)_f = \sum_{f=1}^{n} \upsilon_f \mathbf{A}_f \bullet \left(\nabla \mathbf{u} \right)_f \tag{4.19}$$

The viscosity in the diffusion term is the total viscosity which includes molecular and eddy viscosities. The eddy viscosity is calculated using the Smagorinsky sub-grid model formulated by Eq. (3.4). The important issue for the diffusion term is how to treat the dot product of the face area and the velocity gradient at the face for non-orthogonal meshes. As shown in Fig. 4.1 and Eqs. (4.8) and (4.9) the orthogonal and non-orthogonal contributions can be taken into account by introducing vectors **D** and **K**. Therefore, the diffusion term can be written in the following form:

$$\sum_{f=1}^{n} \upsilon_f \mathbf{A}_f \bullet (\nabla \mathbf{u})_f = \sum_{f=1}^{n} \upsilon_f \left[\mathbf{D}_f \bullet (\nabla \mathbf{u})_f + \mathbf{K}_f \bullet (\nabla \mathbf{u})_f \right] \tag{4.20}$$

where the first and second terms in the bracket are the orthogonal and non-orthogonal contributions, respectively. The viscosity at the face is approximated by linear interpolation. Since the angle between vector **D** and vector **d** which connects points P and N is zero, the orthogonal contribution can be computed as:

$$\mathbf{D}_f \bullet (\nabla \mathbf{u})_f = \left| \mathbf{D}_f \right| \frac{\mathbf{u}_N - \mathbf{u}_P}{\left| \mathbf{d}_f \right|} \tag{4.21}$$

In the term accounting for the non-orthogonal contributions, the velocity gradient at the cell centers and faces are estimated based on the method described in Section 4.3.3. The non-orthogonal contribution is included in the source term.

4.3.1.3 Temporal Term

The temporal term in Eq. (4.17) is discretized using the first-order Euler scheme as follows:

$$V_P \frac{\partial \mathbf{u}}{\partial t} = V_P \frac{\mathbf{u}_P^{t+\Delta t} - \mathbf{u}_P^{t}}{\Delta t} \tag{4.22}$$

The velocity contribution of the previous time step is included in the source term of Eq. (4.17).

4.3.1.4 Final Discretization Form

The discretized terms shown in the previous sub-sections are combined to obtain a general discretized equation. For example, if the upwind scheme is used for the convective term, the general discretized equation is written as follows:

$$V_P \frac{\mathbf{u}_P^{t+\Delta t}}{\Delta t} + \sum_{f=1}^{n} \left(\max(Flux_f ,0)\mathbf{u}_P + \max(-Flux_f ,0)\mathbf{u}_N \right) = -\frac{V_P}{\rho} \nabla p_P + \sum_{f=1}^{n} \nu_f \left|\mathbf{D}_f\right| \frac{\mathbf{u}_N - \mathbf{u}_P}{\left|\mathbf{d}_f\right|} + S_u^U \qquad (4.23)$$

where the source term is

$$S_u^U = V_P \frac{\mathbf{u}_P^t}{\Delta t} + V_P \mathbf{g} + \sum_{f=1}^{n} \upsilon_f \left(\mathbf{K}_f \bullet (\nabla \mathbf{u})_f \right) \qquad (4.24)$$

By rearranging the velocity terms of the cell under consideration P on the left side and terms of the neighbor cells on the right side, Eq. (4.24) can be written in the following form:

$$a_P^U \mathbf{u}_P = \sum_{N=1}^{nb} a_N^U \mathbf{u}_N - \frac{V_P}{\rho} \nabla p_P + S_u^U \qquad (4.25)$$

$$a_N^U = \max(-Flux_f ,0) + \nu_f \frac{\left|\mathbf{D}_f\right|}{\left|\mathbf{d}_f\right|} \quad , \quad a_P^U = \sum_{N=1}^{nb} a_N^U - S_p^U \quad , \quad S_p^U = -\sum_{N=1}^{nb} Flux_f - \frac{V_P}{\Delta t} \qquad (4.26)$$

where *nb* denotes the number of neighbor cells or in other words the number of faces. Eq. (4.25) is the general discretized finite-volume form of the momentum equation.

Eq. (4.25) shows linear dependence of velocity on pressure and vice versa. Therefore, the RANS equation calculates the correct values of velocity field only when the pressure field in the new time step is given. Since the new time step pressure is unknown, the RANS equation is solved using a guessed pressure field which can be the initial or previous time step pressure. The velocity field calculated based on the guessed pressure may not necessarily satisfy the continuity equation. This reveals that a velocity-pressure coupling scheme is required. Several coupling methods have been developed in the literature, such as MAC algorithm (Harlow and Welch 1965), projection method (Chorin 1968), Semi-Implicit Method for Pressure Linked Equations (SIMPLE) (Patankar and Spalding 1972), SIMPLE-Revised (SIMPLER) (Patankar 1980), SIMPLE-Consistent (SIMPLEC) (van Doormaal and Raithby 1984) and Pressure Implicit solution by Split Operator (PISO) (Issa 1986). Jang et al. (1986) and Yin and Chow (2003) compared the SIMPLE, SIMPLER, SIMPLEC, and PISO methods and concluded that PISO yields more stable results and takes less computational time. Therefore, the PISO method is used in this study. To couple velocity and pressure we need to derive a pressure equation. Derivation of the explicit version of the PISO method is the subject of next section.

4.3.2 Pressure Equation

We shall now derive the pressure equation from the continuity equation. By volume integrating Eq. (4.4) and using the Gauss' theorem we have:

$$\int_V \nabla \bullet \mathbf{u} dV = \sum_{f=1}^{n} \mathbf{A}_f \bullet u_f = 0 \tag{4.27}$$

For deriving the pressure equation it is needed to approximate the face velocity values. In the collocated grid, which is adopted in the present study, estimating the face velocity using simple linear interpolation leads to numerical oscillations in the pressure and velocity fields. In order to avoid the decoupling of the pressure and velocity, the momentum interpolation method introduced by Rhie and Chow (1983) is used. This interpolation technique improves the pressure-velocity coupling on the non-staggered grids (Wu 2007).

The discretized momentum equation (4.25) at node P can be rewritten as:

$$\mathbf{u}_P = \frac{\mathbf{H}(\mathbf{u})_P}{a_P^U} - \frac{V_P}{a_P^U \rho} \nabla p \tag{4.28}$$

where

$$\mathbf{H}(\mathbf{u})_P = \sum_{N=1}^{nb} a_N^U \mathbf{u}_N + S_u^U \tag{4.29}$$

Using the momentum interpolation, the velocity at face *f* is approximated by:

$$\mathbf{u}_f = \left(\frac{\mathbf{H}(\mathbf{u})_P}{a_P^U}\right)_f - \left(\frac{V_P}{a_P^U \rho}\nabla p\right)_f \tag{4.30}$$

Substituting Eq. (4.30) into Eq. (4.27) leads to:

$$\sum_{f=1}^{n} \mathbf{A}_f \bullet \left(\left(\frac{\mathbf{H}(\mathbf{u})}{a_P^U}\right)_f - \left(\frac{V}{a_P^U \rho}\nabla p\right)_f \right) = 0 \tag{4.31}$$

The quantity $\left(\mathbf{H}(\mathbf{u})/a_P^U\right)_f$ is evaluated by linear interpolation of $\mathbf{H}(\mathbf{u})/a_P^U$ at node P and the corresponding adjacent node N. The pressure gradient at a cell face is calculated by taking into account the orthogonal and non-orthogonal contributions as follows:

$$\sum_{f=1}^{n} \mathbf{A}_f \bullet (\nabla p)_f = \sum_{f=1}^{n} \left(\mathbf{D}_f \bullet (\nabla p)_f + \mathbf{K}_f \bullet (\nabla p)_f \right) \tag{4.32}$$

where

$$\mathbf{D}_f \bullet (\nabla p)_f = \left|\mathbf{D}_f\right| \frac{p_N - p_P}{\left|\mathbf{d}_f\right|} \tag{4.33}$$

In the non-orthogonal term, the face value of pressure gradient is calculated similarly to the face value of velocity gradient in the non-orthogonal diffusion term of the momentum equation described in Section 4.3.1.2. The non-orthogonal contribution is considered as the source term of the pressure equation. Substituting Eq. (4.32) into Eq. (4.31), the general form of the pressure equation can be formulated as:

$$a_P^P p_P = \sum_{N=1}^{nb} a_N^P p_N + S_u^P \tag{4.34}$$

where

$$a_N^P = \left(\frac{V_P}{a_P^U \rho}\right)_f \frac{\left|\mathbf{D}_f\right|}{\left|\mathbf{d}_f\right|} \tag{4.35}$$

$$a_P^P = \sum_{N=1}^{nb} a_N^P \tag{4.36}$$

$$S_u^P = \sum_{f=1}^{n} \mathbf{K}_f \bullet (\nabla p)_f - \sum_{f=1}^{n} \mathbf{A}_f \bullet \left(\frac{\mathbf{H(u)}}{a_P^U} \right)_f \tag{4.37}$$

4.3.3 Gradient of Flow Properties

A second-order accurate approximation of the gradients at the centroid of control volume can be calculated based on the Gauss's theorem, as shown in Eqs. (4.13) and (4.14).The gradient at a cell face can be computed using linear interpolation between the gradients at the cell under consideration (P) and the neighbor cell (N). Haselbacher and Blazek (2000) demonstrated that the linear interpolation leads to a wide stencil which allows for the decoupling of the solution on quadrilateral or hexahedral grids. Crumpton et al. (1997) and Weiss et al. (1999) modified the face gradient as

$$(\nabla \varphi)_f = \overline{(\nabla \varphi)_f} - \left[\overline{(\nabla \varphi)_f} \bullet \mathbf{d}_n - \frac{\varphi_N - \varphi_P}{|\mathbf{d}|} \mathbf{d}_n \right] \tag{4.38}$$

where $\overline{(\nabla \varphi)_f}$ is the average value of gradients at cells P and N, and $\mathbf{d}_n$ is the unit vector of $\mathbf{d}$. Since there is no flow information in the computational domain outside the water surface boundary, the average value of gradients in cells which contain the water surface and also cells adjacent to the water surface may cause unsmooth pressure and velocity fields and water surface profile. Therefore, in this study the gradient at cell face is calculated as

$$(\nabla \varphi)_f = \frac{\varphi_N - \varphi_P}{|\mathbf{d}|} \mathbf{d}_n \tag{4.39}$$

which is also computationally cheaper than Eq. (4.38).

4.3.4 Pressure-Velocity Coupling Algorithm

The solution procedure in a single time step is summarized as follows:

Step 1: The RANS Eq. (4.25) is solved based on the pressure field of the previous time step. This step calculates the velocity field which does not necessarily satisfy the continuity equation.

Step 2: New values of $\mathbf{H}(\mathbf{u})$ are calculated using Eq. (4.29) based on the velocity field calculated by the RANS equation in the first step.

Step 3: Using the new values of $\mathbf{H}(\mathbf{u})$ the pressure Eq. (4.34) is solved to compute a new pressure field.

Step 4: The flow fluxes $F_f=\mathbf{A}_f.\mathbf{u}_f$ are calculated using the new $\mathbf{H}(\mathbf{u})$ calculated at step 2 and new pressure field from step 3. The face value of velocity is computed by Eq. (4.30).

Step 5: Velocity field is corrected using Eq. (4.28) based on the new $\mathbf{H}(\mathbf{u})$ and pressure field.

Step 6: If the corrected velocity field satisfies the continuity equation (error less than a small value), the most recent calculated variables are the final values in the current time step, otherwise a new iteration starts from step 2 by using the most recent updated variables.

4.4 Boundary Conditions

Boundary values of water surface elevation and flow velocity are determined similar to the finite-difference model elaborated in Section 3.4. The Neumann condition with constant gradient $-\boldsymbol{g}$ is used to determine the pressure of cells located at inlet, outlet, and solid wall. The pressure in a cell which contains the water surface is calculated by interpolation (or extrapolation) between the pressures at the water surface (the atmospheric pressure) and an appropriate neighbor fluid cell as follows:

$$p_{i,j,k} = (1-\eta)\, p_n + \eta p_s \tag{4.40}$$

where P_n is the pressure in the neighbor fluid cell, P_s is the water surface pressure and is equal to the atmospheric pressure, and η is a coefficient illustrated in Fig. 3.4(a). The neighbor cell is chosen using the direction of water surface. The Neumann condition with zero gradient is used to define other flow properties at the water surface.

4.5 Surface Capturing Method

In the finite-difference model developed in Chapter 3, the SOLA-VOF technique was adopted to track the water surface. The SOLA-VOF was originally derived for 1-D flow and its implementation in 2-D and 3-D flows requires the operator splitting approach as used in the finite-difference model developed in this study. The SOLA-VOF scheme is not applicable to meshes which contain cells with complicated shapes and unstructured meshes. Ubbink and Issa (1999) developed an interface capturing technique called CICSAM (Compressive Interface Capturing Scheme for Arbitrary Meshes), which is applicable in the context of multi-dimensional applications and avoids the need to use operator splitting. Since the CICSAM scheme was originally an implicit solution, an explicit version of CICSAM used in this study is presented below.

As described before, the time evolution of *F*-function is calculated using the scalar advection Eq. (2.2). The advection equation can be rewritten as:

$$\frac{\partial F}{\partial t} + \nabla \bullet \left(\mathbf{u} F \right) = 0 \tag{4.41}$$

Integrating over control volume gives:

$$\int_V \frac{\partial F}{\partial t} dV + \int_V \nabla \bullet \left(\mathbf{u} F \right) dV = 0 \tag{4.42}$$

Applying the Euler explicit scheme for the temporal derivative term and the Green's theorem for the convection term leads to

$$\frac{F_P^{t+\Delta t} - F_P^t}{\Delta t} V_P + \sum_{f=1}^{n} \mathbf{A}_f \bullet \left(\mathbf{u} F \right)_f = 0 \tag{4.43}$$

Since F is a scalar variable, Eq. (4.43) can be reformulated as the following:

$$\frac{F_P^{t+\Delta t} - F_P^t}{\Delta t} V_P + \sum_{f=1}^{n} \left(\mathbf{A}_f \bullet \mathbf{u}_f \right) F_f = 0 \tag{4.44}$$

in which the term in the parenthesis is the volumetric flux. Then,

$$F_P^{t+\Delta t} = F_P^t - \frac{\Delta t}{V_P} \sum_{f=1}^{n} Flux_f F_f \tag{4.45}$$

As it was mentioned before, F is a step function which changes between zero and one abruptly and special care must be taken to estimate the face values of F. In the CICSAM scheme, which was developed on arbitrary meshes, a switching strategy between HYPER-C and ULTIMATE-QUICKEST (UQ) schemes is used to handle this.

The face value F_f is estimated based on the F values of donor cell D, acceptor cell A, and upwind cell U. The donor cell is always upstream and the acceptor cell is always downstream of the face under consideration. The upwind cell U is the cell upstream of the donor cell. A schematic representation of donor, acceptor, and upwind cells for a 1-D flow is depicted in Fig. 4.2. Basically, the face value F_f should lie between the F values of the donor and acceptor cells. Therefore, the face value can be estimated as

$$F_f = (1-\beta_f)F_D + \beta_f F_A \tag{4.46}$$

where β_f is the weighting factor. In the CICSAM scheme the weighting factor is calculated based on normalized F values as $\beta_f = \left(\tilde{F}_f - \tilde{F}_D\right)\big/\left(1-\tilde{F}_D\right)$. The normalized F value of the donor cell is calculated as

$$\tilde{F}_D = \frac{F_D - F_U}{F_A - F_U} \tag{4.47}$$

The normalized face value F_f is estimated using a switching strategy between the HYPER-C and ULTIMATE-QUICKEST (UQ) schemes as follows:

$$\tilde{F}_f = \gamma_f \tilde{F}_{f(Hyper-C)} + (1-\gamma_f)\tilde{F}_{f(UQ)} \tag{4.48}$$

where γ_f is the switching factor, and $\tilde{F}_{f(HYPER-C)}$ and $\tilde{F}_{f(UQ)}$ are the normalized face values computed using the HYPER-C and UQ schemes, respectively. The switching factor varies between zero and one based on the angle between the interface and the direction of flow motion as

$$\gamma_f = \min\left(\frac{\cos(2\theta_f)+1}{2}, 1\right) \tag{4.49}$$

where $\theta_f = \arccos\left|\frac{(\nabla F)_D \bullet \mathbf{d}_f}{\left|(\nabla F)_D\right|\left|\mathbf{d}_f\right|}\right|$. Vector $\mathbf{d}_f$ connects the centroids of the donor and acceptor cells. The HYPER-C and UQ normalized face values are computed as

$$\tilde{F}_{f(HYPER-C)} = \begin{cases} \min\left(1, \dfrac{\tilde{F}_D}{C_D}\right) & \text{when } 0 \le \tilde{F}_D \le 1 \\ \tilde{F}_D & \text{otherwise} \end{cases} \tag{4.50}$$

$$F_{f(UQ)} = \begin{cases} \min\left(F_{f(HYPER-C)}, \dfrac{8C_D F_D + (1-C_D)(6F_D+3)}{8} \right) & \text{when } 0 \le F_D \le 1 \\ F_D & \text{otherwise} \end{cases} \tag{4.51}$$

where C_D is the summation of the Courant number for outflow faces of the donor cell, $C_D = \sum_{f=1}^{n} \max(0, C_f)$.

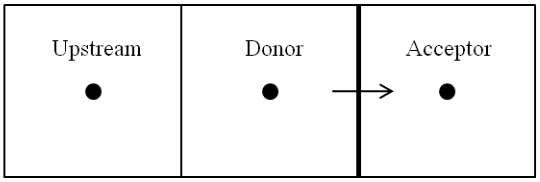

Fig. 4.2 Definition of donor, acceptor, and upstream cells (the arrow shows the flow direction at the face under consideration)

4.6 Model Stability

Time step is controlled by the Courant-Friedrichs-Lewy (CFL) and VOF conditions described in Eq. (3.22).

4.7 Model Test

The developed finite-volume hydrodynamic model is tested using six laboratory experiments. The first test case investigates the capability of the model to simulate initial stages of dam-break flows over wet and dry beds. In the second test case the model simulates the breaking process of a solitary wave on a sloping beach, which can be seen as the propagation of dam-break wave over an inclined channel. The ability of the model to simulate dam-break flows over uneven beds is further investigated using dam-break flows over trapezoidal and triangular steps in the third and fourth test cases. The fifth test case is simulation of dam-break flow over a

3-D isolated block. In the last test the model is validated by simulating the 3-D dam-break flow caused by partial dam failure.

The simulations are carried out on a desktop computer with Windows 7 operating system, Intel Core i7-3.20 GHz processor, and 24 GB memory (RAM). The source code of the developed model is written serial in FORTRAN 90 and runs on single core CPU processor.

4.7.1 Initial Stage of Dam-Break Flow over Wet and Dry Flat Beds

The developed model is first tested using the experiments of initial stage of dam-break flow described in Sections 3.7.1 and 3.7.2. Herein, it is assumed that the gate is lifted instantaneously. The computational grid spacing is 0.75 cm. The computational mesh contains 26 and 40 vertical layers in the wet and dry bed cases, respectively. Figs. 4.3 and 4.4 show the comparison between measured and calculated water surface profiles at different instances for dam-break flows over wet and dry beds, respectively. The calculated results reveal that the developed 3-D finite-volume model can simulate the initial stages of dam-break flow well.

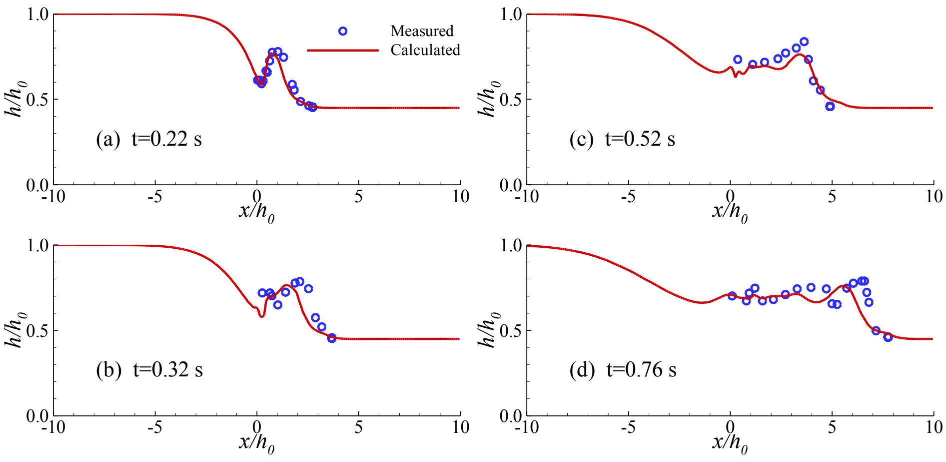

Fig. 4.3 Measured and calculated water surface profiles caused by dam break over wet bed (measurements from Stansby et al., 1998)

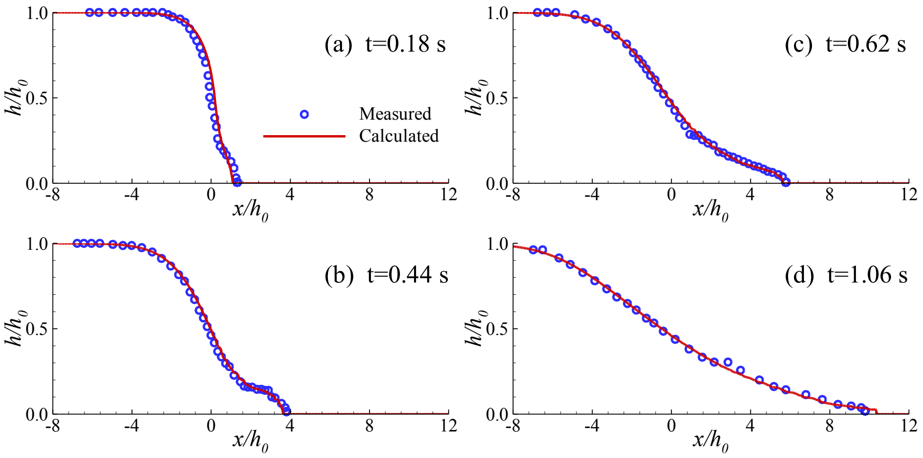

Fig. 4.4 Measured and calculated water surface profiles caused by dam break over dry bed (measurements from Ozmen-Cagatay and Kocaman, 2010)

4.7.2 Breaking Solitary Wave on a Sloping Beach

Synolakis (1986) carried out a series of experiments to investigate runup/rundown and breaking of a solitary wave propagating on a sloping beach. The topography consisted of a plane beach with a slope of 1:19.85 adjacent to a constant depth region, as shown in Fig. 4.5 (a). The initial condition was still water of h=0.2 m in depth. The experimental run with H/h =0.3, in which H is the wave height, is selected here to test the developed model's capability of simulating breaking waves on a sloping beach. The first-order solitary wave theory is used to define the initial water surface profile z_s and longitudinal flow velocity u as follows (Synolakis 1987, Li and Raichlen 2002, Que and Xu 2006, and Mahdavi and Talebbeydokhti 2009):

$$z_s = H \sec h^2 \left[\sqrt{\frac{3H}{4h^3}} (x - X) \right] \tag{4.52}$$

$$u = -z_s \sqrt{\frac{g}{h}} \tag{4.53}$$

where the initial wave crest is located at x=X. In the experiment, the initial wave crest was located at X=14h (Mahdavi and Talebbeydokhti 2009). The computational domain is represented by a mesh containing hexahedral cells with grid spacing equal to 0.75 cm. The computational mesh consists of 56 vertical layers. Fig. 4.5 (b) shows the side view of mesh fitted on the flat bed as well as the sloping beach. For convenience, the measured and calculated data are compared in non-dimensional forms: $x^* = x/h$, $z^* = z/h$, and $t^* = t\sqrt{g/h}$.

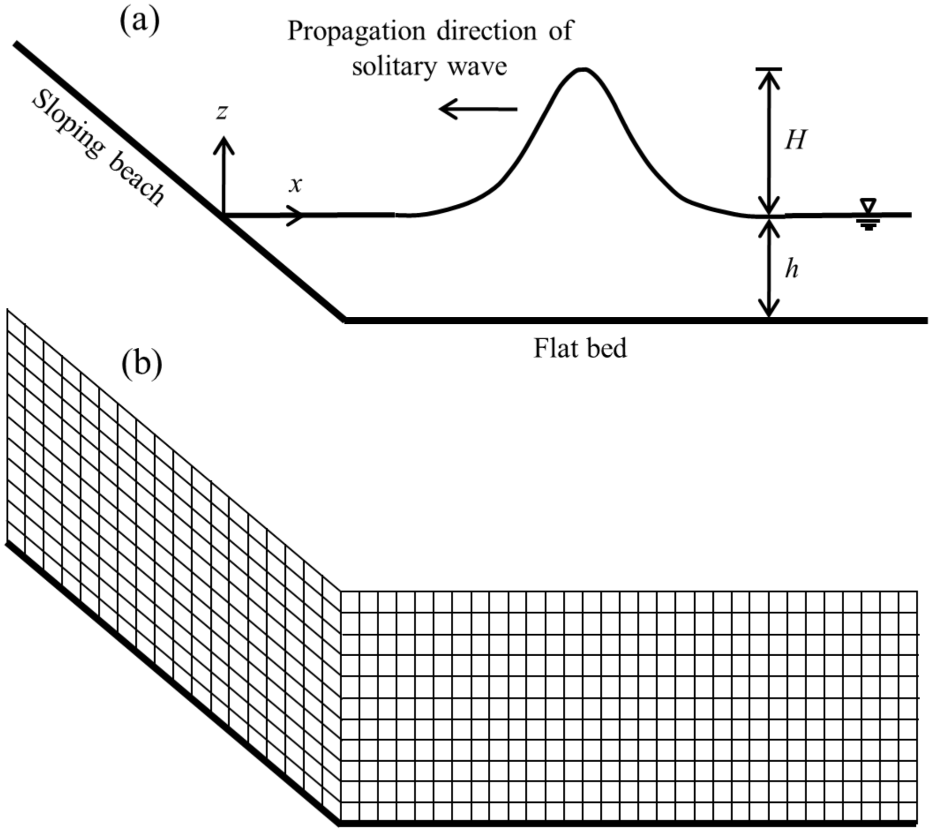

Fig. 4.5 Schematic side view of (a) solitary wave runup on a sloping beach (b) computational mesh

Figs. 4.6 shows the water surface profiles obtained at different times. At t^* = 5 and 10 (Figs. 4.6(b) and (c)), the wave shoals and the front face becomes steeper. These two snapshots indicate that the breaking process can be simulated by the numerical model accurately. As can be seen, the wave speed and wave height are well-simulated as well. When the breaking process terminates at t^*=15 (Fig. 4.6(d)) the attenuated wave forms a tongue propagating up the sloping beach at t^* = 20, 25, and 30 (Fig. 4.6(e) to (g)). After the broken wave reaches the highest point around t^* = 35 (Fig. 4.6(h)), rundown takes place in which a thin layer of water accelerates down the beach, and at approximately t^* = 40 (Fig. 4.6(i)) the receding supercritical flow impacts the wave tail near the still water shoreline. The model approximates this flow pattern as a hydraulic jump. Figs. 4.6(i) and (j) show that the simulated rundown process takes place faster than the observed process. This might be because of the surface tension force which is not considered by the model. The surface tension exerts a resistance force which slows down the rundown process of the thin layer of water.

The solitary wave breaks in between t^*=10 and t^*=15. It is important to investigate the ability of the model to simulate the breaking process of the solitary wave; however there is no measured data to evaluate the accuracy of the simulated breaking process. Fig. 4.7 shows the solitary wave propagating on the sloping beach from t^*=11 to t^*=14. At t^*=11 the wave amplitude reaches a critical level and the wave shoaling process terminates. The breaking process starts at t^*=12 and wave breaking occurs at t^*=13. Finally, at t^*=14 the wave crest deformation finishes and the crest collides with the sloping beach.

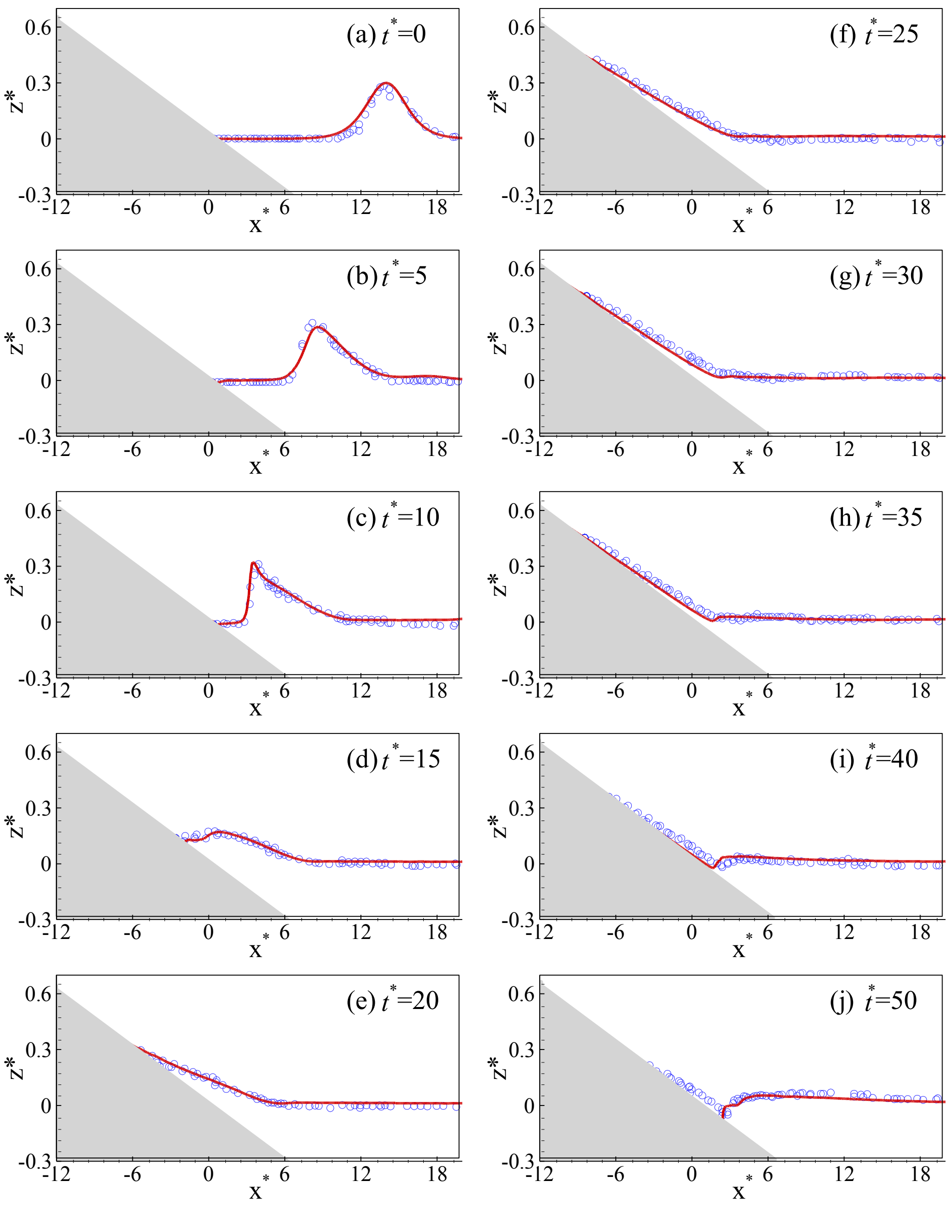

Fig. 4.6 Propagation of breaking solitary wave on a sloping beach (solid red line: calculated, blue circles: measurements from Synolakis, 1986)

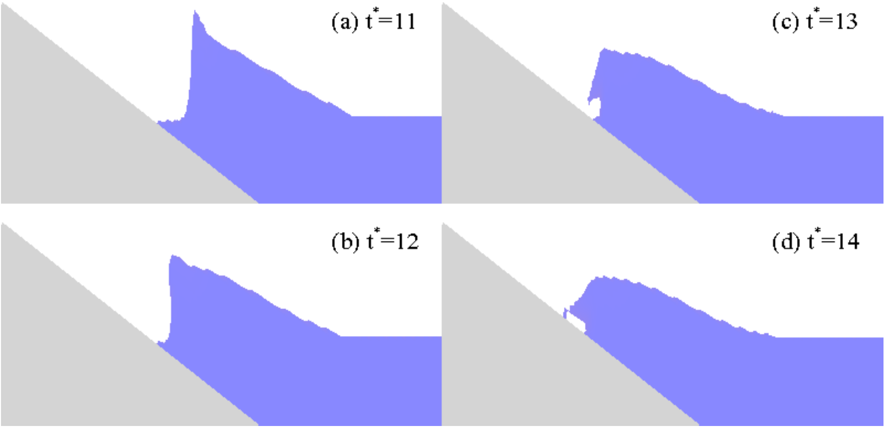

Fig. 4.7 Simulated wave breaking process on a sloping beach

4.7.3 Dam-Break Flow over a Trapezoidal Step

The developed model is tested using the experiment conducted by Kocaman (2007). The measured data are reported by Ozmen-Cagatay and Kocaman (2011). The laboratory flume was 9 m long, 0.3 m wide, and 0.34 m high. The flume bed and walls were made of glass. A gate was located 4.65 m from the channel entrance. The initial water depth in the reservoir, h_0, was 25 cm and the downstream was dry. A trapezoidal shaped step was placed downstream of the flume. Fig. 4.8(a) shows the 3-D sketch of the laboratory flume and Fig. 4.8(b) shows the step dimensions and the computational mesh around the step. The bottom line of the mesh fits along the step surface. The computational mesh uses 28 vertical layers and the computational grid spacing is equal to1 cm.

Fig. 4.9 compares the measured and calculated water surface profiles at different instances. When the dam-break wave reaches the step, the flow forms a hydraulic jump and overtops the step at t=1.9 s. The wave height rises till t=2.8 s when the reflected wave starts propagating upstream. The dam-break and reflected waves are simulated well by the model.

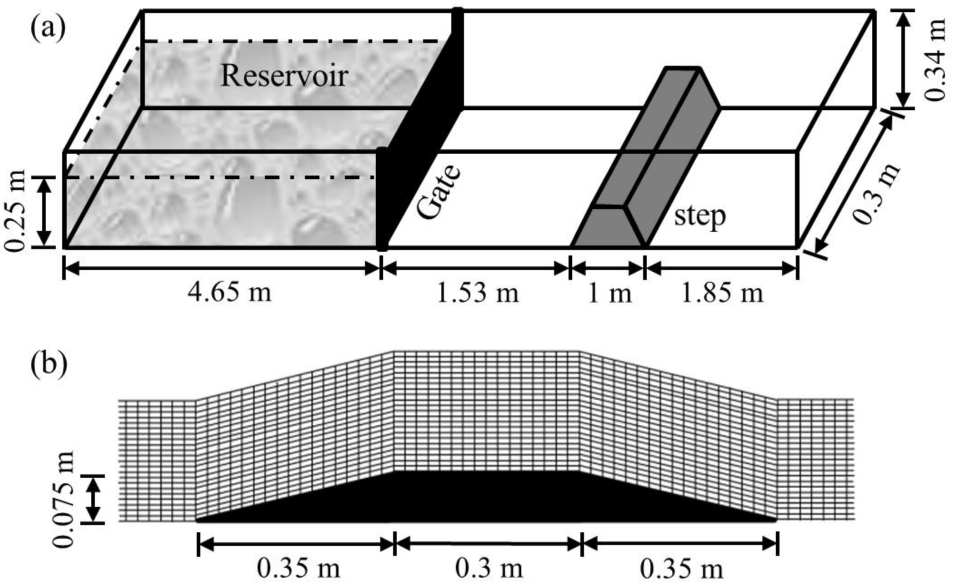

Fig. 4.8 (a) 3-D sketch of the laboratory flume; (b) side view of the trapezoidal shaped step and the computational mesh around the step

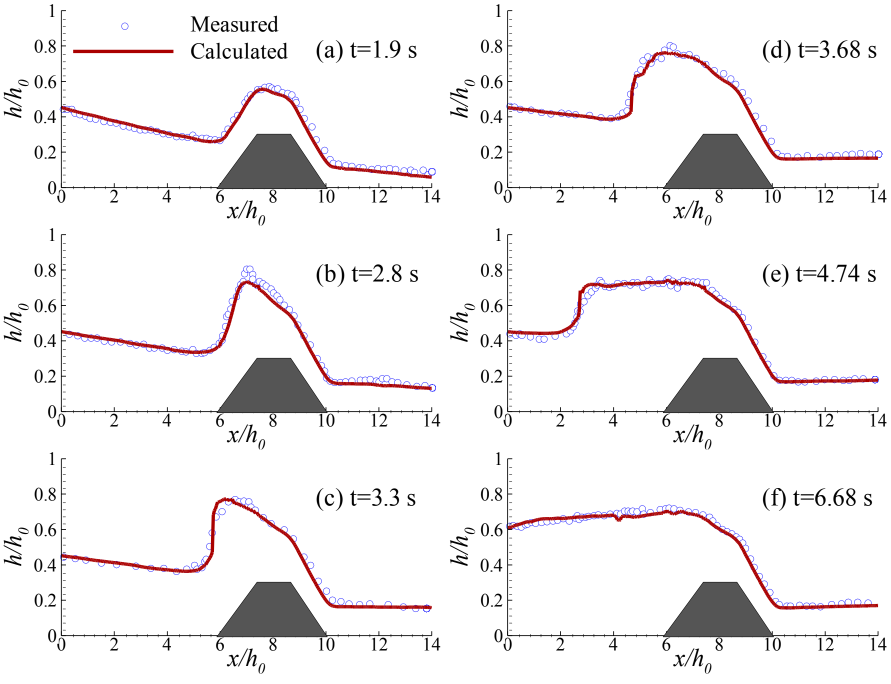

Fig. 4.9 Measured (circles) and calculated (solid line) water surface profiles (measurements from Ozmen-Cagatay and Kocaman, 2011)

4.7.4 Dam-Break Flow over a Triangular Step

The model is tested using laboratory dam-break flows over a triangular step selected from the Concerted Action on Dam-Break Modeling project, CADAM, (Kao and Chang 2012). The experimental set-up consisted of a rectangular channel 38 m in length, 1 m in width, and 1 m in height with a gate located 15.5 m from the channel entrance to separate the upstream reservoir and the downstream channel. A triangular step 6 m long, 1 m wide, and 0.4 m high was placed 13 m downstream of the gate. The initial water depth in the reservoir was 0.75 m and the reach between the gate and the step was dry. In the experiments, different initial and boundary conditions were used for the channel reach between the step and the outlet. Herein two runs are chosen to test the present model. In the first run, the channel reach downstream of the step was initially dry and the boundary condition at the end of the channel was open outlet. In the second run, the downstream boundary condition was closed, and the channel reach between the step and downstream boundary was wet in which the water depth was 0.15 m initially, as shown in Fig. 4.10(a). Measuring gages G4, G10, G13, and G20 were placed at the center line of the channel and 4, 10, 13, and 20 m downstream from the gate, respectively, to record the time evolution of water surface. The computational domain is represented by a mesh containing hexahedral cells with grid spacing equal to 2 cm. The computational mesh contains 40 vertical layers. The bottom layer of the mesh fits the step surface, as shown in Fig. 4.10(b).

Fig. 4.11 shows the comparison between the measured and calculated time evolutions of the water surface at four measuring gages for the run with dry bed downstream of the step. At gage G4, the progressive dam-break wave leads to a rapid increase in the water level in about the first 3 seconds, and then the water level varies slowly till about t=13 s when the reflected wave caused by the step arrives and leads to the second rapid increase in the water level. Then, the water level decreases smoothly till the second reflected wave caused by the upstream wall of the reservoir arrives at t=36 s. The water level at gage G10 increases rapidly due to the progressive dam-break wave and the reflected wave from the step in the first 8 s, varies slowly in the next 8 s when the reflected wave travels upstream, and then starts decreasing at t=16 s till the second reflected wave arrives at t=39 s. Since the downstream boundary condition is open outlet, the water surface elevation at gages G13 and G20 rises only because of the progressive wave and no wave reflection is observed. Simulated time evolution of water surface level for the run with wet bed downstream of the step is compared with the measured data in Fig. 4.12. Similar to the run with dry bed, it can be seen that the model is able to simulate the changes of the water surface caused by the progressive and reflected waves well. The water levels are influenced additionally by the reflected wave from the downstream end, particularly at gages G13 and G20.

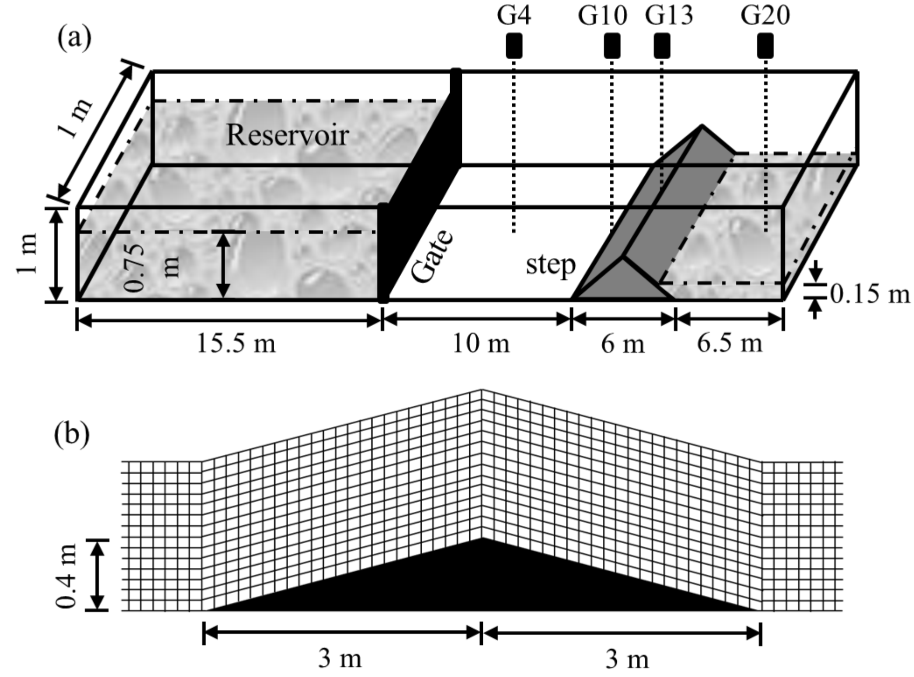

Fig. 4.10 (a) 3-D sketch of the laboratory flume; (b) side view of the triangular shaped step and the computational mesh around the step

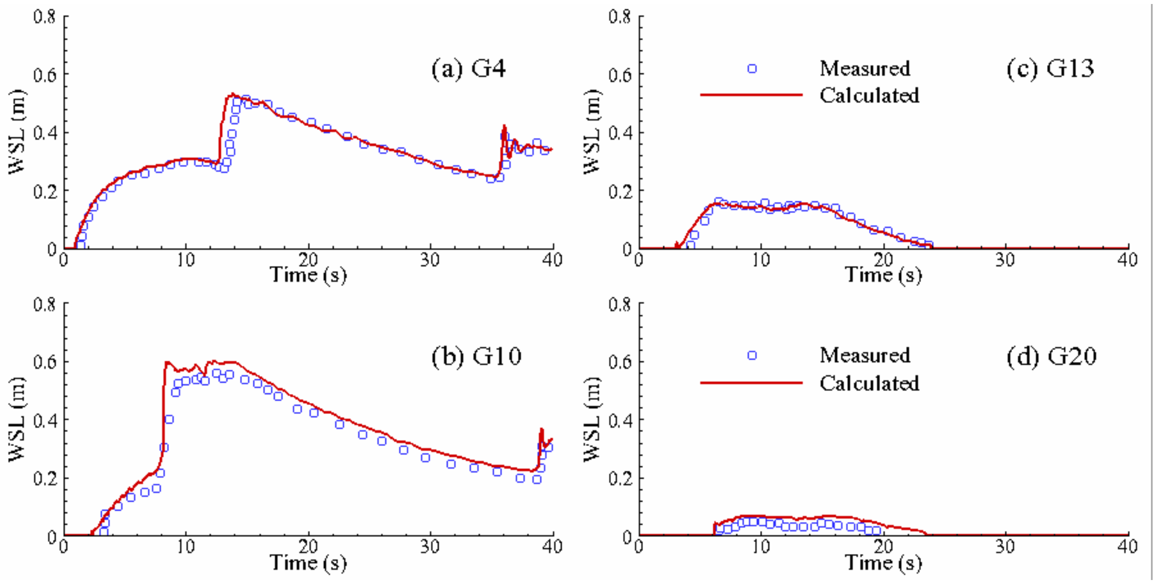

Fig. 4.11 Measured and calculated water surface time series for the run with dry bed downstream of the step (measurements from Kao and Chang, 2012)

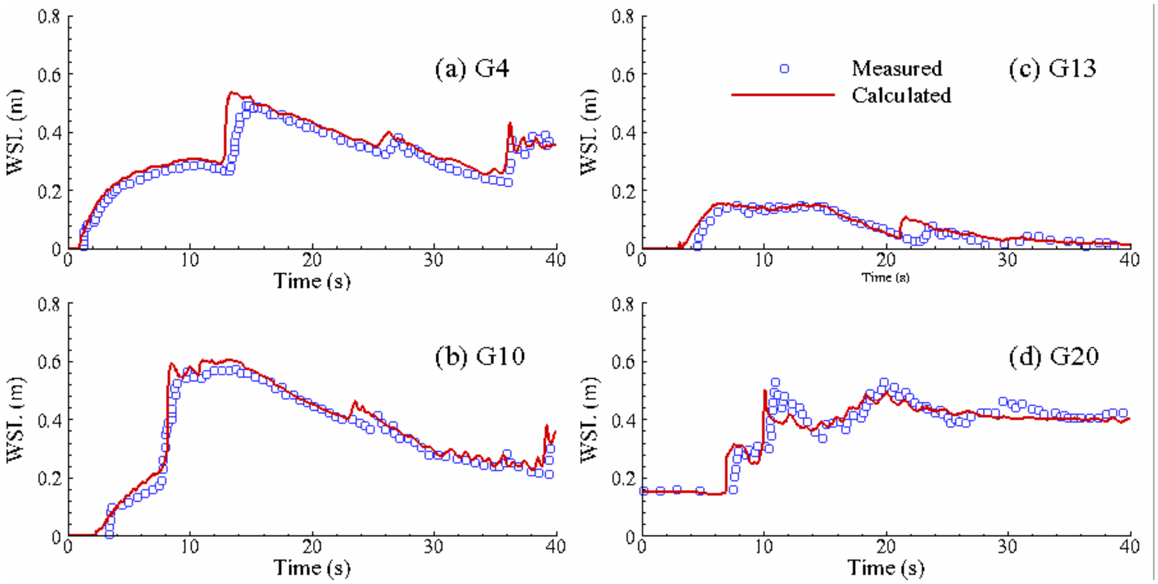

Fig. 4.12 Measured and calculated water surface time series for the run with wet bed downstream of the step (measurements from Kao and Chang, 2012)

4.7.5 Dam-Break Flow over an Isolated Block

The model is validated using the laboratory experiment of dam-break flow over a 3-D isolated block carried out at the Maritime Research Institute of the Netherlands (MARIN) (Kleefsman et al. 2005). The laboratory tank was 3.22 m long, 1 m wide, and 1 m high. A rectangular block of 0.403×0.161×0.161 m was placed 1.17 m downstream of the reservoir. The initial water depth inside the reservoir was 0.55 m and the downstream region was dry. Fig. 4.13 shows the configuration of the tank and the locations of measurement gages. Two water level gages (H2, H4) were installed in the downstream and upstream of the gate, and four pressure gages (P1, P3, P5, P7) were on the upstream side and top of the block. The computational mesh consists of 50 vertical layers and the grid spacing is equal to 2 cm.

Fig. 4.14 shows the water level time series at gages H2 and H4. Similar time evolution patterns are shown in the measured and calculated water levels. The dam-break wave front reaches to gage H2 at t=0.4 s and the water level increases until t=2.4 s when the reflected waves from the block and the downstream wall arrive. Then the water level decreases until the reflected wave from upstream wall reaches the gage. The reflected wave height is somehow over-predicted. At gage H4, the water level decreases as the reservoir drains smoothly until t=2.9 s when the first reflected wave arrives and travels toward the upstream wall. The reflected wave hits the wall and is reflected back downstream, showing a peak water level around t=3.9 s. The measured and calculated pressure time series at gages P1, P3, P5, and P7 are shown in Fig. 4.15. Both measurement and simulation show sudden increase in pressures at gages P1 and P3 when the wave hits the block at about t=0.5 s. The calculated results exhibit a few spurious spikes at the gages on the top of the step (P5 and P7). This is due to the isolated empty cells (air pockets) in the water as described in Section 3.7.5. The air pockets arise when the progressive wave hits the block, gets redirected upward and falls onto the top of the block. Similar problem was also observed by Kleefsman et al. (2005). Nevertheless, the comparisons in Fig. 4.15 reveal the capability of the developed model to predict the pressure changes caused by the progressive and reflected waves.

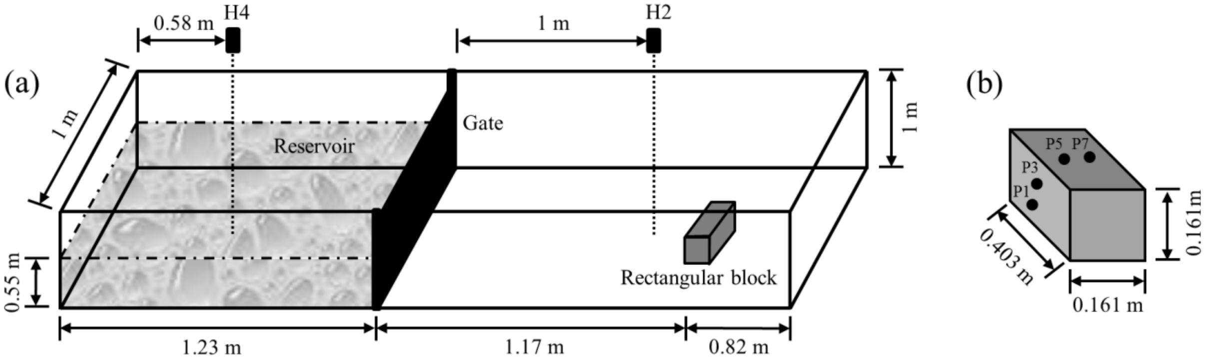

Fig. 4.13 (a) 3-D sketch of the MARIN dam-break experiment; (b) the rectangular block

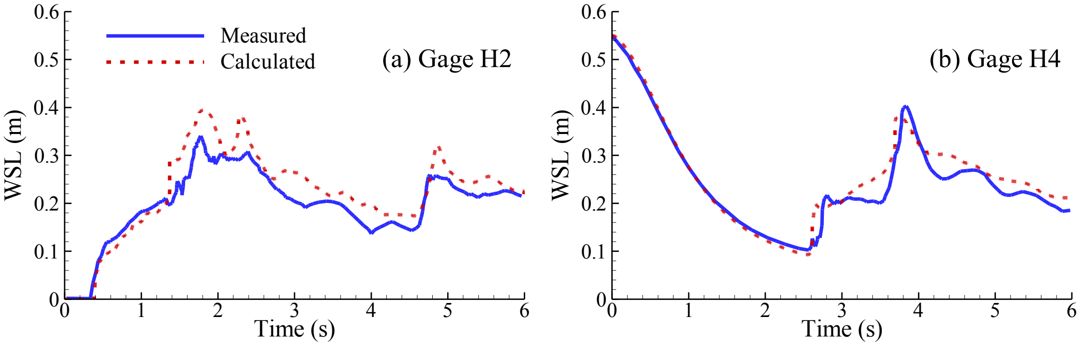

Fig. 4.14 Time evolution of water surface level (measurements from Kleefsman et al., 2005)

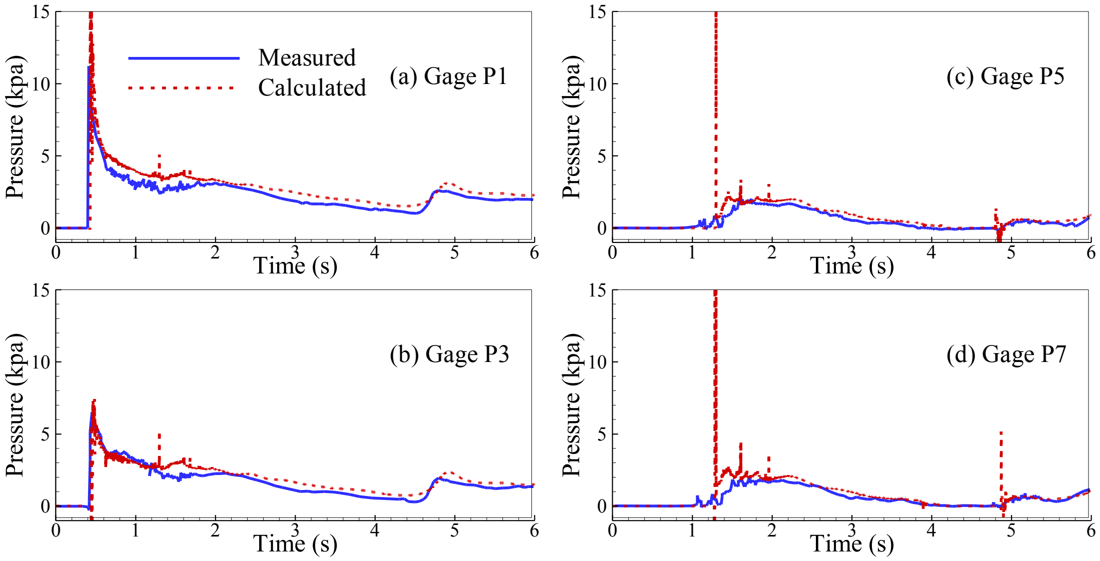

Fig. 4.15 Time evolution of pressure (measurements from Kleefsman et al., 2005)

4.7.6 Dam-Break Flow Caused by Partial Failure

The developed model is further validated by the 3-D partial dam-break flow experiment conducted by Fraccarollo and Toro (1995) in a 3 m long, 2 m wide, and 0.7 m high flume, as shown in Fig. 4.16. The partially broken dam was represented by two impervious vertical walls and a 0.4 m wide gate located between the walls, 1 m from the upstream end of the flume. The gate was opened rotationally. The initial water depth in the reservoir was 0.6 m and the downstream channel was dry with open outlet and side boundaries. The time evolution of water level, pressure, and velocity were measured at several gages as sketched in Fig. 4.16. Gages G-5A, G-3A, G-2A, and GC were placed inside the reservoir, G0 at the gate site, and G2A and G8A downstream of the gate. The computational grid consists of cells with equal grid spacing of 2 cm and 35 vertical layers.

Fig. 4.17 shows a good agreement between the measured and calculated time series of the water levels at gages G-5A, GC, G0 and G8A. The calculated pressures at the bottom of gages

G-5A, G-3A, G0 and G2A are compared with measured ones in Fig. 4.18 and reveals the model is accurate. Fig. 4.19 compares the measured and calculated time evolutions of the longitudinal flow velocities at 5, 15, 25, and 35 cm above the bed at gages G-2A and G0. The comparison shows a temporal gap in which the calculated velocity reaches to the peak value about 0.3 s prior to the measured one. As described in Section 3.7.4, this might be due to the rotational motion of the gate removal process in the experiment whereas the model assumes sudden removal. After reaching the maximum value, the measured and calculated velocities decrease with similar behavior.

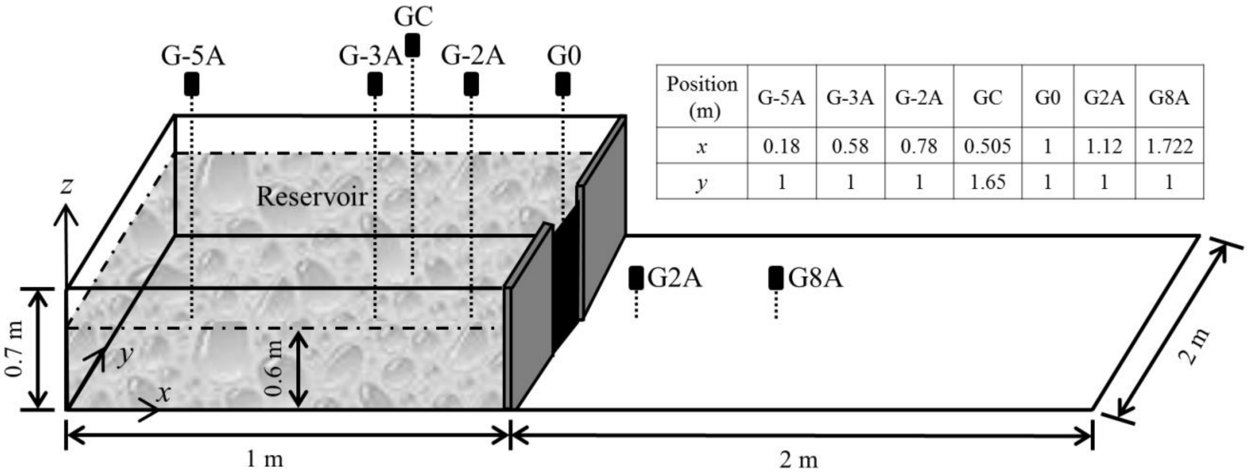

Position (m)	G-5A	G-3A	G-2A	GC	G0	G2A	G8A
x	0.18	0.58	0.78	0.505	1	1.12	1.722
y	1	1	1	1.65	1	1	1

Fig. 4.16 Sketch of the partial dam-break experiment

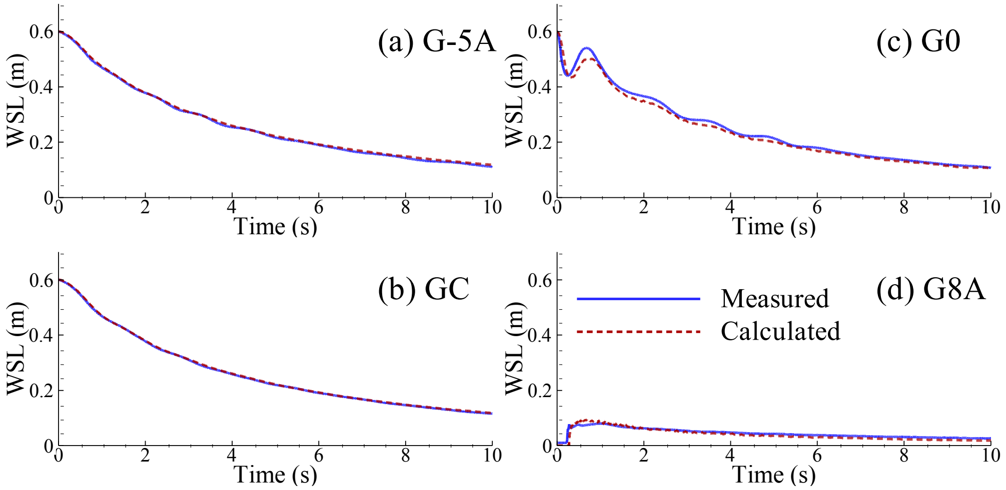

Fig. 4.17 Measured and calculated water surface levels (measurements from Fraccarollo and Toro 1995)

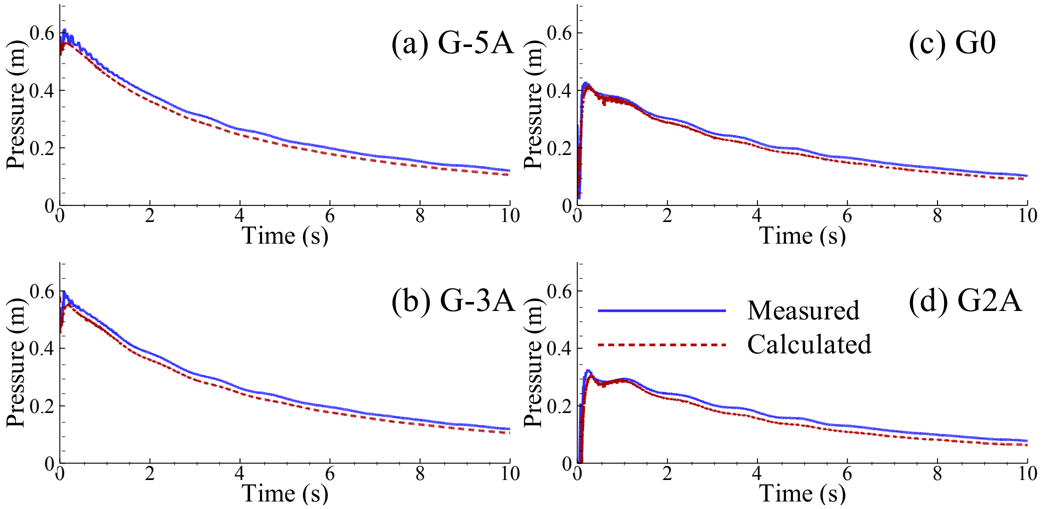

Fig. 4.18 Measured and calculated pressures at the bottom (measurements from Fraccarollo and Toro 1995)

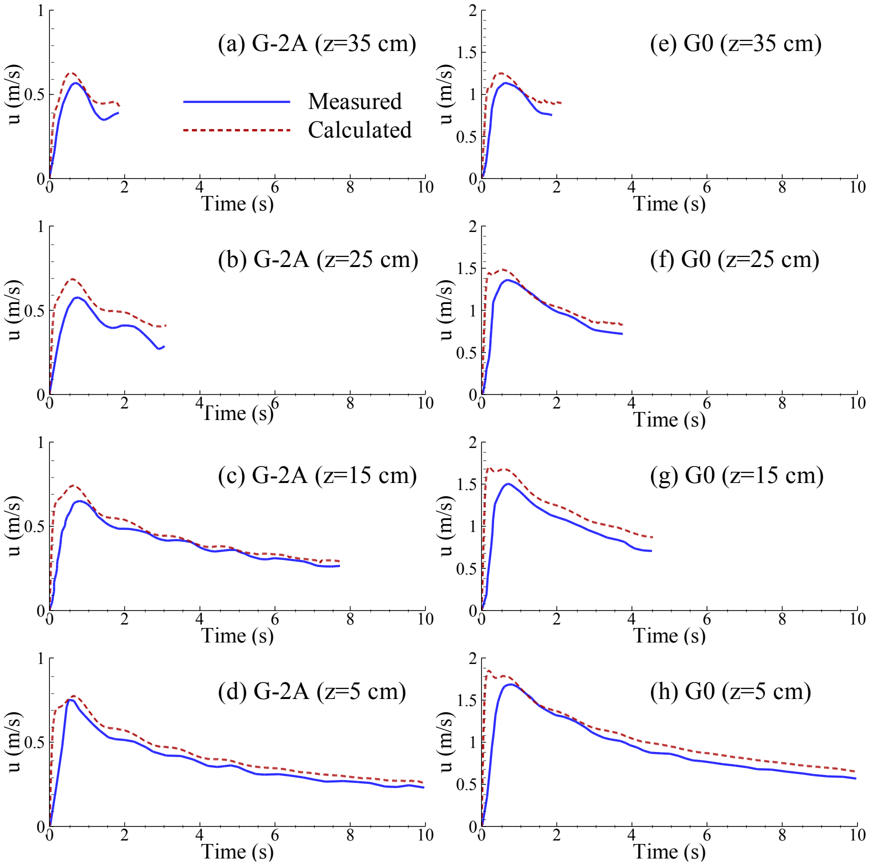

Fig. 4.19 Measured and calculated velocities in the longitudinal direction at different vertical distances from the bed (measurements from Fraccarollo and Toro 1995)

4.8 Summary

In this chapter, a 3-D finite-volume model of dam-break flows over irregular beds has been developed. This is required in a dam-break flow model over movable beds since the grid is better to be fitted on irregular beds. The hydrodynamic equations are solved using an explicit finite-volume method based on collocated mesh with hexahedral cells that fits on the bed. The turbulent viscosity is calculated by the Smagorinsky model. The velocity and pressure coupling is achieved by using the PISO method and the Rhie and Chow's (1983) momentum interpolation method. An explicit version of CICSAM-VOF surface-capturing method is formulated and used to track the changes of water surface.

The developed model has been tested using six sets of classical laboratory experiments. The initial stage of dam-break flows over dry and wet beds were examined in the first test case. The results of the second test case showed that the propagation of breaking solitary wave over sloping beach can be simulated well using a boundary-fitted mesh. Moreover, the ability of the model to simulate dam-break flows over irregular beds using solid boundary-fitted meshes was validated in the third and fourth test cases. The fifth test case was simulation of dam-break flow over an isolated rectangular block. Finally, the model was tested using a 3-D partial dam-break flow. The calculated water levels, pressures and velocities are in good agreement with the measured data.

CHAPTER 5

3-D FINITE-VOLUME MODEL OF SEDIMENT TRANSPORT UNDER DAM-BREAK FLOW OVER MOVABLE BEDS

The developed model in Chapter 4 is extended to simulate dam-break flow over movable beds. In other words, this chapter presents a 3-D sediment transport model integrated with the 3-D hydrodynamic model of dam-break flow developed in Chapter 4. Therefore, the model comprises two parts; hydrodynamic module and sediment transport module. The hydrodynamic module, which developed and validated in Chapter 4, calculates the flow velocity, pressure, and eddy viscosity. The sediment transport module solves the sediment transport and bed change equations based on the results calculated by the hydrodynamic module. In this chapter the governing equations and numerical solutions of the sediment transport module are first described and then the developed model is tested using several experimental dam-break flows over movable beds.

5.1 General Concepts and Definitions

Sediment particles in natural rivers transported by flow are called the total load. The total load usually contains bed-material load and wash load. Sediment particles which can be found in appreciable quantities in the river bed are categorized as the bed-material load. In contrast, the wash load consists of only those sediment particles that move mainly in suspension and cannot be found in the river bed in appreciable quantities. The wash load originates from upland sources instead of the river bed. Since the wash load consists of fine particles suspended in the flow and made up of grains that are only found from the local bed in small quantities, the bed-material load is typically considered as the total load in a fluvial system.

The bed-material load can also be divided into bed load and suspended load. The bed load consists of sediment particles that slide, roll, or saltate in a thin layer above the river bed shown in Fig. 5.1. It usually accounts for 5-25 percent of the total load for fine particles and more for coarse particles in natural rivers (Wu 2007). On the other hand, the suspended load consists of sediment particles that are suspended in the water column above the bed-load layer. The suspended-load sediments are supported by the flow turbulence.

Because of the different behaviors of bed load and suspended load, the water column can be divided into a bed-load zone and a suspended-load zone. The bed-load zone, shown in Fig. 5.1, is a thin layer between the bed elevation z_b and $z_b+\delta_b$, whereas the suspended-load zone is a thicker layer between $z_b+\delta_b$ and water surface z_s. The thickness of the bed-load layer is usually assumed to be about twice the sediment particle diameter or half the bed-form height in natural rivers.

Because of variations in flow conditions and channel morphology, sediment transport is usually in non-equilibrium state. Sediment cannot reach new equilibrium states instantaneously due to temporal and spatial lags between the flow and sediment transport (Wu 2007). Therefore, the non-equilibrium sediment transport should be taken into account in a model of sediment transport under rapidly-varying flow conditions. In the next section the governing equations of non-equilibrium sediment transport in the suspended-load and bed-load layers are presented.

5.2 Governing Equations of Sediment Transport

The governing equation of single-sized sediment transport in the suspended-load zone with a thickness of h-δ_b is formulated as

$$\frac{\partial c}{\partial t}+\frac{\partial\left[\left(u_j-\omega_s\delta_{j3}\right)c\right]}{\partial x_j}=\frac{\partial}{\partial x_j}\left(\varepsilon_s\frac{\partial c}{\partial x_j}\right) \tag{5.1}$$

where c is the suspended-load concentration, ε_s is the turbulent diffusivity of sediment, ω_s is the settling velocity, and δ_{j3} is the Kronecker delta with “3” indicating the vertical direction. The turbulent diffusivity of sediment and the settling velocity are explained later in the next sections.

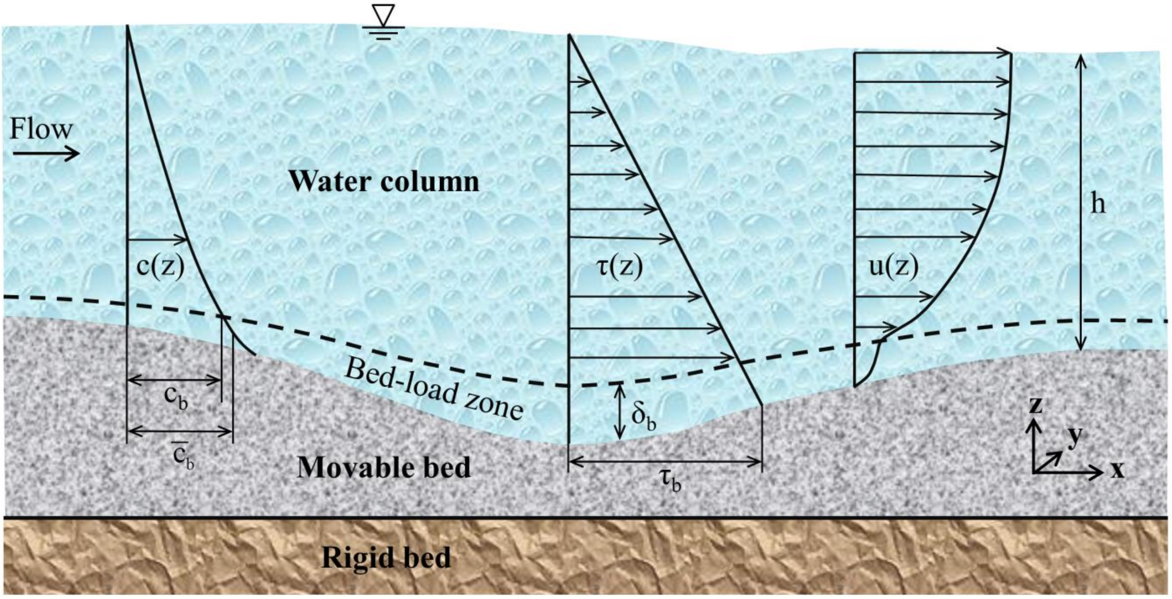

Fig. 5.1 Schematic view of flow and sediment transport ($c(z)$=vertical distribution of sediment concentration, $\tau(z)$=vertical distribution of shear stress, $u(z)$=vertical distribution of stream-wise velocity, c_b=near-bed sediment concentration, $\overline{c}_b$=averaged near-bed sediment concentration, and τ_b=bed shear stress)

Because the bed-load layer is a thin layer near the bottom, the bed-load transport equation in the 3-D model has the same formulation as that in the horizontal 2-D model as follows (Wu 2007):

$$\frac{\partial(q_b/u_b)}{\partial t}+\frac{\partial(\alpha_{bx}q_b)}{\partial x}+\frac{\partial(\alpha_{by}q_b)}{\partial y}=\frac{1}{L}(q_{b*}-q_b) \tag{5.2}$$

where q_b and q_{b*} are the actual and equilibrium (capacity) transport rates of bed load, u_b is the bed-load velocity, α_{bx} and α_{by} are the direction cosines of bed-load movement that is assumed to be along the near-bed flow direction, and L is the adaptation length of sediment particles. The direction cosines α_{bx} and α_{by} are calculated using the near-bred flow velocity vector as $\alpha_{bx}=u/U$, $\alpha_{by}=v/U$, where U is the velocity magnitude, $U=(u^2+v^2)^{0.5}$.The velocity and equilibrium (capacity) transport rate of bed load are determined using empirical formulas described later.

The bed change due to total load is calculated using the following relation:

$$(1-p'_m)\frac{\partial z_b}{\partial t}=D_b-E_b+\frac{1}{L}(q_b-q_{b*}) \tag{5.3}$$

where p'_m is the porosity of sediment deposit, and D_b and E_b are the deposition and entrainment fluxes of sediment, respectively, at the interface between bed load and suspended load. D_b and E_b are determined as

$$D_b=\omega_s c_b\,,\ E_b=\omega_s c_{b*} \tag{5.4}$$

where c_b and c_{b*} are the actual and equilibrium (capacity) suspended-load concentrations, respectively, at the interface between bed load and suspended load. The equilibrium (capacity) near-bed suspended-load concentration is calculated using an empirical equation described later.

5.3 Boundary Conditions

In the sediment transport module the boundary values of bed-load transport rate and suspended-load concentration may be required. In the inflow boundary the bed-load transport rate and suspended-load concentration must be given. At the outflow boundary, calculating the bed load does not require any boundary condition, and the suspended-load concentration is determined using the Neumann condition in which the concentration gradient in the flow direction is set to zero. At solid wall boundary the Dirichlet and Neumann conditions are used to define the bed-load rate and suspended-load concentration, respectively. The bed-load rate is set to zero and the suspended-load concentration is determined using zero gradient condition. At the water surface boundary the net vertical flux across the water surface should be zero (Wu, 2007). Thus, the suspended-load boundary condition at the water surface is

$$\left(\varepsilon_s \frac{\partial c}{\partial z} + \omega_s c \right)_{z=z_s} = 0 \tag{5.5}$$

At the interface between the bed load and suspended load zones, the net sediment exchange flux D_b-E_b is applied. The sediment entrainment flux is rewritten as

$$E_b = -\varepsilon_s \left. \frac{\partial c}{\partial z} \right|_{z=z_b+\delta_b} = \omega_s c_{b*} \tag{5.6}$$

which is used as the suspended-load concentration boundary condition at the interface near the bed.

5.4 Numerical Solution Methods

The suspended-load transport equation, Eq. (5.1), is applied in the suspended-load zone h-δ_b, whereas the bed-load transport equation, Eq. (5.2), is valid over the bed-load zone δ_b. Because the suspended-load domain is different from the flow domain, the arrangement of the flow and suspended-load control volumes near the bed is an important issue (Wu, 2007). If the bed-load layer is thinner than the first near-bed flow cell, the near-bed suspended-load cell is only part of the first flow cell. This needs special care of the suspended-load cell geometry and cell flux computation. For simplicity, in this study the suspended-load zone starts from the second row of computational cells, and the bed-load transport equation is solved in the first row (δ_b is set equal to the z-grid spacing of the first vertical layer). Because Eq. (5.2) does not include the bed-load layer thickness, therefore δ_b and the z-grid spacing Δz of the first row of cells are not necessarily the same. However, it is a good practice to set up the z-grid spacing of the first layer of the computational mesh close to the bed-load layer thickness. This is important for suspended load calculation and sediment mass balance. The z-grid spacing of mesh layers above the first layer can be constant as the first layer or varying as a function of z.

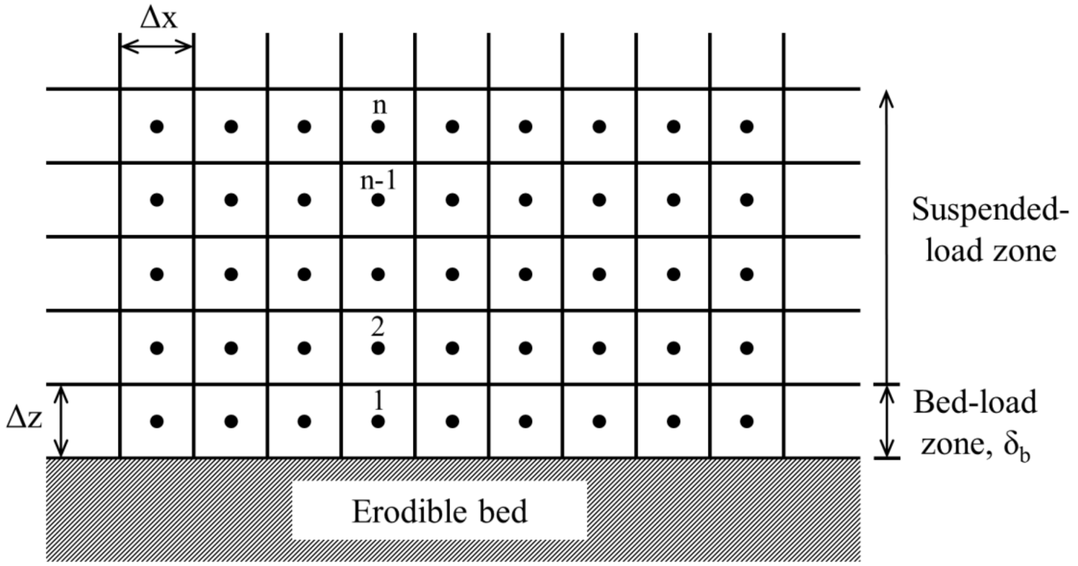

Fig. 5.2 Schematic definition of the bed-load and suspended-load zones in the finite-volume computational mesh

5.4.1 Discretization of Suspended-Load Transport Equation

The suspended-load transport equation, Eq. (5.1), can be written in the following form:

$$\frac{\partial c}{\partial t}+\nabla \bullet \left(u_j c\right)=\nabla \bullet \left(\varepsilon_s \frac{\partial c}{\partial x_j}\right)+\frac{\partial\left(\omega_s \delta_{j3}\right)c}{\partial x_j} \tag{5.7}$$

and integrating it over the control volume and using the Gauss's theorem yields

$$\frac{\partial(cV_P)}{\partial t}+\sum_{f=1}^{n}\mathbf{A}_f \bullet (\mathbf{u}c)_f=\sum_{f=1}^{n}\mathbf{A}_f \bullet \left(\varepsilon_s \nabla c\right)_f+\int \frac{\partial\left(\omega_s \delta_{j3}\right)c}{\partial x_j}dV \tag{5.8}$$

The convection term is rewritten as

$$\sum_{f=1}^{n}\mathbf{A}_f \bullet (\mathbf{u}c)_f=\sum_{f=1}^{n} Flux_f c_f \tag{5.9}$$

The fluxes are known from the hydrodynamic calculations. In the case of movable bed, the mesh moving velocity is considered, which is described later. The exponential scheme (Patankar, 1980) is used to estimate the face values of concentration.

Similar to the hydrodynamic model developed in the previous chapter, we consider the mesh orthogonality and non-orthogonality by dividing the diffusion term into two separate terms as follows:

$$\sum_{f=1}^{n}\varepsilon_{sf}\mathbf{A}_f \bullet (\nabla c)_f=\sum_{f=1}^{n}\varepsilon_{sf}\left[\mathbf{D}_f \bullet (\nabla c)_f+\mathbf{K}_f \bullet (\nabla c)_f\right] \tag{5.10}$$

where the first and second terms in the bracket are the orthogonal and non-orthogonal contributions, respectively. The non-orthogonal contribution is included in the source term. The orthogonal contribution can be written as

$$\mathbf{D}_f \bullet (\nabla c)_f=\left|\mathbf{D}_f\right|\frac{c_N-c_P}{\left|\mathbf{d}_f\right|} \tag{5.11}$$

where c_N and c_P are the concentration of neighbor cell and cell under consideration, respectively,

To discretize the last term on the right-hand side of Eq. (5.8), it is assumed that the settling velocity is a vector variable $\boldsymbol{\omega}_s=(0,0,\omega_{s,z})$. This assumption and using the Gauss's theorem yields

$$\int \frac{\partial\left(\omega_s \delta_{j3}\right)c}{\partial x_j} dV = \int \nabla \bullet (\boldsymbol{\omega}_s c) dV = \sum_{f=1}^{n} \mathbf{A}_f \bullet (\boldsymbol{\omega}_s c)_f \tag{5.12}$$

Eq. (5.12) is included in the source term. The upwind scheme is used to estimate the face concentration.

The temporal term in Eq. (5.8) is discretized using the first-order explicit Euler scheme as follows:

$$\frac{\partial (c V_P)}{\partial t} = \frac{c_P^{t+\Delta t} V_P^{t+\Delta t} - c_P^t V_P^t}{\Delta t} \tag{5.13}$$

In which the contribution of the previous time step is included in the source term.

The final discretized equation of suspended-load sediment transport can be formulated in the general form as follows:

$$a_P^c c_P = \sum_{N=1}^{nb} a_N^c c_N + S_u^c \tag{5.14}$$

where a_N^c are the coefficients of neighbor cells and

$$a_P^c = \sum_{N=1}^{nb} a_N^c - S_p^c \tag{5.15}$$

and the source terms are

$$S_u^c = \frac{c_P^t V_P^t}{\Delta t} + \sum_{f=1}^{n} \mathbf{A}_f \bullet (\boldsymbol{\omega}_s c)_f + \sum_{f=1}^{n} \varepsilon_{sf} \left(\mathbf{K}_f \bullet (\nabla c)_f \right) \quad , \quad S_p^c = -\frac{V_P^{t+\Delta t}}{\Delta t} \tag{5.16}$$

Because of the upwind scheme used for the settling velocity term, if the face value of concentration in the second term of S_u^c takes the value of neighbor cell, it is kept in the source term S_u^c; otherwise it is included in S_p^c.

Eq. (5.14) is solved explicitly. The calculated concentrations of neighbor cells at the previous time step are used to calculate the first term on the right hand side of Eq. (5.14). The source terms are also calculated based on the values calculated at the previous time step.

5.4.2 Discretization of Bed-Load Transport Equation

To integrate Eq. (5.2) over the control volume, the direction cosines are defined as a vector variable $\boldsymbol{\alpha}_b=(\alpha_{bx},\alpha_{by},0)$. Thus, the bed-load transport equation can be written as

$$\frac{\partial\left(q_b/u_b\right)}{\partial t}+\nabla\bullet\left(\boldsymbol{\alpha}_b q_b\right)=\frac{1}{L}\left(q_{b*}-q_b\right) \tag{5.17}$$

The direction cosine components are calculated using the near-bred (first vertical layer of computational mesh) flow velocity vector. The bed-load velocity u_b is formulated in Section 5.5.

Integrating Eq. (5.17) over the control volume and using the Gauss's theorem yields

$$\frac{\partial\left(V_P q_b/u_b\right)}{\partial t}+\sum_{f=1}^{n}\mathbf{A}_f\bullet\left(\boldsymbol{\alpha}_b q_b\right)_f=\frac{V_p}{L}\left(q_{b*}-q_b\right)_P \tag{5.18}$$

The term on the right-hand side of Eq. (5.18) is included in the source term. In addition, the bed-load rate of the previous time step is included in the source term as well. The face value of bed-load rate in the second term on the left-hand side of Eq. (5.18) is estimated using the upwind scheme.

The final discretized equation of bed-load sediment transport can be formulated as follows:

$$a_P^{q_b}q_{b,P}=\sum_{N=1}^{nb}a_N^{q_b}q_{b,N}+S_P^{q_b} \tag{5.19}$$

where the coefficients are

$$a_N^{q_b}=\phi_{upwinding}\left(\mathbf{A}_f\bullet\boldsymbol{\alpha}_{bf}\right)\quad,\qquad a_P^{q_b}=\sum_{N=1}^{nb}a_N^{q_b}-\overline{S}_P^{q_b} \tag{5.20}$$

where $\phi_{upwinding}$ is the up-winding coefficient which depends on the flow direction. When the flux at the face is negative $\phi_{upwinding}$=-1; otherwise $\phi_{upwinding}$=0. The source terms of the discretized equation are

$$S_P^{q_b} = \frac{V_P^t}{u_b \Delta t} q_{b,P}^t + \frac{V_P^t}{L} q_{b*,P} \quad , \quad \bar{S}_P^{q_b} = -\sum_{N=1}^{nb} \left(\mathbf{A}_f \bullet \boldsymbol{\alpha}_f \right) - \frac{V_P^{t+\Delta t}}{u_b \Delta t} - \frac{V_P^t}{L} \tag{5.21}$$

Similar to the suspended-load calculations, Eq. (5.19) is solved explicitly.

5.4.3 Discretization of Bed Change Equation

The bed change equation (5.3) is discretized as

$$\Delta z_{b,P} = \frac{\Delta t}{1 - p_m'} \left[D_{b,P}^{t+\Delta t} - E_{b,P}^{t+\Delta t} + \frac{1}{L} \left(q_{b,P}^{t+\Delta t} - q_{b*,P}^{t+\Delta t} \right) \right] \tag{5.22}$$

and the calculated bed change is used to update the bed elevation as $z_{b,P}^{t+\Delta t} = z_{b,P}^t + \Delta z_{b,P}$.

The near-bed concentration must be calculated in order to determine the near-bed sediment exchange flux in Eq. (5.22). Using the near-bed suspended-load boundary condition, Eq. (5.6), Wu et al. (2000a) derived the following relation for the near-bed concentration:

$$c_b = c_2 + c_{b*} \left(1 - e^{-(z_2 - z_b - \delta_b)\omega_s / \varepsilon_s} \right) \tag{5.23}$$

where subscript 2 stands for the cell above the boundary between the bed-load and suspended-load zones as shown in Fig. 5.2.

5.4.4 Computational Grid Adjustment

The bed changes calculated using Eq. (5.22) result in time evolution of bed topography which can affect the water surface profile and wave speed significantly. There are two approaches to handle this movable bed problem. The first approach is to use a fixed mesh with immersed boundary techniques (Peskin, 1972 and 1977) for the irregular and movable bed. In this approach, the mesh resolution near the bed is usually very fine, so that the flow calculation can provide smooth bed shear stress profile and in turn sediment entrainment flux. The second approach is to use a moving or adaptive mesh to conform with the irregular and movable bed. This approach does not need to refine the mesh near the bed as the first approach. Since a boundary fitted grid is used, the calculated flow field can have smooth bed shear stress required by sediment transport calculation. The second approach is used in this study, so that the mesh moves up and down to fit on the bed boundary. Therefore, at each time step, it is necessary to update the computational grid based on the calculated bed elevation and the flow and sediment transport equations are solved on the updated grid.

Figs. 5.3(a) and (b) indicate that the side faces of the computational cells comprise constant unit normal vectors, whereas the top and bottom faces may adopt new unit normal vectors imposed by the local bed slopes. Therefore, the top and bottom cell faces at the new computational time step may not hold the same geometrical properties as the previous time step, because of mesh moving. According to Fig. 5.3(a) and (b), if $\mathbf{n}_{\mathrm{top}}^{t}$ is the unit normal vector of the top face at time *t*, a new unit normal vector $\mathbf{n}_{\mathrm{top}}^{t+\Delta t}$ needs to be calculated at time $t=t+\Delta t$. To calculate the unit normal vectors, the face slopes must be estimated. As shown in Fig. 5.3 (c), the longitudinal and lateral bed slopes of every cell can be estimated using bed elevations at cell faces as formulated below:

$$\mathrm{SlopeX_P} = \frac{Z_{b,\mathrm{e}} - Z_{b,\mathrm{w}}}{\Delta x_{\mathrm{P}}} \ , \ \mathrm{SlopeY_P} = \frac{Z_{b,\mathrm{n}} - Z_{b,\mathrm{s}}}{\Delta y_{\mathrm{P}}} \tag{5.24}$$

where the bed elevations at cell faces are estimated using linear interpolation between bed elevations of cell under consideration P and the neighbor cell which possesses the same face.

The new estimated unit normal vectors are used to calculate the area of cell faces and the cell volume. The updated geometrical properties of computational cells, including the cell volume, face area and unit normal vector, are then used to discretize and solve the governing equations at the next time step. The cell volume changes must be taken into account when the temporal term of the governing equations are discretized. Therefore, for example, the discretized temporal term of the momentum equation, Eq. (4.22), is amended as

$$\frac{\partial\left(V_{\mathrm{P}}\mathbf{u}\right)}{\partial t}=\frac{V_{\mathrm{P}}^{t+\Delta t}\mathbf{u}_{\mathrm{P}}^{t+\Delta t}-V_{\mathrm{P}}^{t}\mathbf{u}_{\mathrm{P}}^{t}}{\Delta t} \tag{5.25}$$

Another outcome of moving mesh which must be addressed is the effect of the mesh velocity on the flow and consequent sediment transport calculations. Mesh adjustment in every time step introduces an external velocity added to the system with a magnitude depending on the updated coordinates of each control volume. For example, consider the individual cell P with coordinate $\mathbf{r}_P^t$ at time t and $\mathbf{r}_P^{t+\Delta t}$ at time $t+\Delta t$, the velocity vector associated with the change of coordinate of cell P can be calculated by $(\mathbf{r}_P^{t+\Delta t}-\mathbf{r}_P^t)/\Delta t$. The imposed mesh velocity must be taken into consideration when the convective fluxes in the governing equations are determined. Therefore, the convection term of the momentum equation, Eq. (4.18), is rewritten as

$$\begin{aligned}\sum_{f=1}^{n}\left(\mathbf{A}_f\bullet\mathbf{u}_f\right)\mathbf{u}_f=\sum_{f=1}^{n}\left(\mathbf{A}_f\bullet(\mathbf{u}_{\mathrm{flow},f}-\mathbf{u}_{\mathrm{mesh},f})\right)\mathbf{u}_f&=\sum_{f=1}^{n}\left(\mathbf{A}_f\bullet\mathbf{u}_{\mathrm{flow},f}-\mathbf{A}_f\bullet\mathbf{u}_{\mathrm{mesh},f}\right)\mathbf{u}_f\\&=\sum_{f=1}^{n}(Flux_f-\mathbf{A}_f\bullet\mathbf{u}_{\mathrm{mesh},f})\mathbf{u}_f\end{aligned} \tag{5.26}$$

where the mesh velocity vector $\mathbf{u}_{\mathrm{mesh},f}$ includes only the vertical velocity, $\mathbf{u}_{\mathrm{mesh},f}=(0,0,w_{\mathrm{mesh},f})$, since the mesh moves only up and down.

Described in the previous chapter the pressure equation is derived by replacing the face velocity values calculated by the momentum equation into the continuity equation. Therefore, since the momentum equation is corrected for moving mesh, the necessary amendments caused by the moving mesh are also addressed by the pressure equation of PISO method.

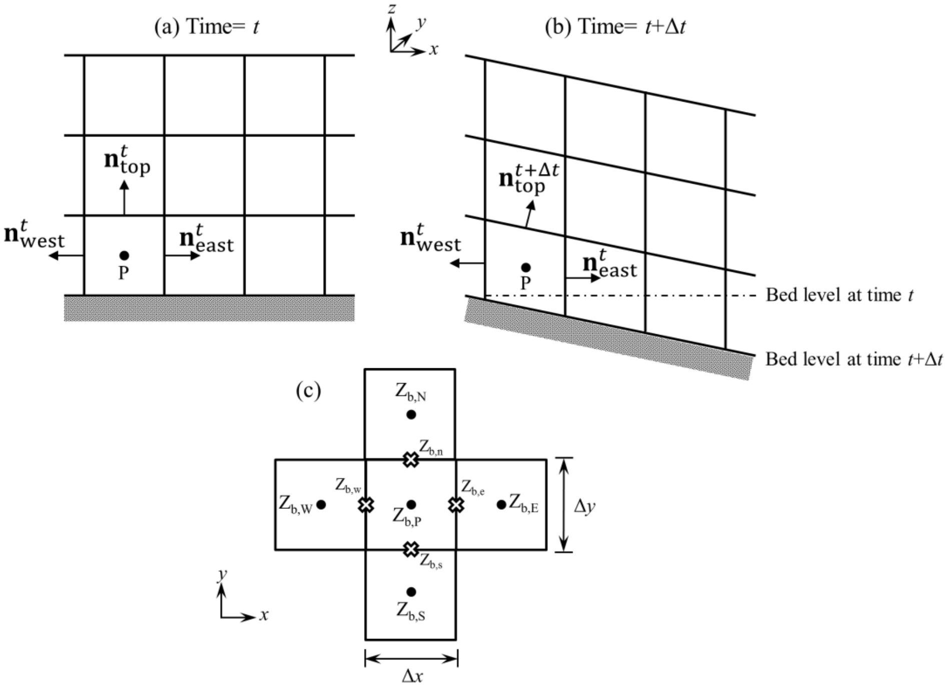

Fig. 5.3 (a-b) Side views of unit normal vector of cell faces, and (c) Plan view of stencil used to estimate bed slopes (black dots: bed elevation at cell centers, crosses: bed elevation at cell faces)

5.5 Model Parameters

In order to close the developed sediment transport model, several parameters, such as the suspended-load near-bed equilibrium concentration, bed-load transport capacity, bed shear stress, critical shear stress, sediment turbulent diffusivity, settling velocity, and adaptation length need to be determined. Next sub-sections elaborate the model parameters in details.

5.5.1 Equilibrium Transport Rate of Bed Load

The equilibrium transport rate of single-sized bed load, q_{b*}, is computed by the Wu et al. (2000b) equation:

$$q_{b*} = 0.0053\sqrt{\left(\gamma_s/\gamma - 1\right) g d^3}\, T^{2.2} \tag{5.27}$$

where q_{b*} is by volume per unit time and width (m^2/s), γ_s is the specific weight of sediment, γ is the specific weight of water, d is the sediment diameter assumed to be d_{50} of the sediment particles since the model adopts single-sized sediment, and T is the transport stage number defined as follows:

$$T = \frac{\tau_b}{\tau_{cr}} - 1 \tag{5.28}$$

where τ_b, which is the (effective) bed shear stress, and τ_{cr}, which is the critical shear stress allowing erosion, are described later.

5.5.2 Near-Bed Equilibrium Concentration of Suspended Load

In general, the near-bed equilibrium concentration of suspended load is related to the bed-load transport rate as

$$c_{b*} = \frac{q_{b*}}{u_b \delta_b} \tag{5.29}$$

where u_b is the bed-load velocity determined using the modified van Rijn formula (Wu, 2007) as

$$u_b = 1.64 T^{0.5} \sqrt{\left(\frac{\rho_s}{\rho} - 1\right) g d} \tag{5.30}$$

where ρ_s is sediment density.

Using Eqs. (5.29) and (5.30) the near-bed equilibrium suspended-load concentration is determined as

$$c_{b*} = \frac{0.0053}{1.64 \delta_b} T^{1.7} d \tag{5.31}$$

where c_{b*} is the volumetric concentration of suspended load at the interface of the bed-load and suspended-load zones.

5.5.3 Effective Bed Shear Stress

The effective bed shear stress τ_b can be defined as

$$\tau_b = \sqrt{\tau_{b,x}^2 + \tau_{b,y}^2} \ , \text{ with } \tau_{b,x} = C_{fb}\rho u U \text{ and } \tau_{b,y} = C_{fb}\rho v U \tag{5.32}$$

where τ_{bx} and τ_{by} are the longitudinal and lateral components of the effective bed shear stress, respectively, C_{fb} is the bed friction coefficient, and ρ is the water density.

In this study, the effective bed shear stress is modified to address the effects of local hydrodynamic pressure gradient, steep slope, and high sediment concentration on sediment transport. These effects can be ignored in steady flows in rivers with gentle bed slope and low sediment concentration but are not negligible in rapidly-varied flows such as dam-break flow on movable beds. In rapidly varied flows, the gradient of dynamic pressure causes a pressure-difference force on sediment particles. The effects of dynamic-pressure-difference force, gravity force over a steep slope, and high sediment concentration are taken into account as (Wu 2007):

$$\tau_{b,x} = k_t C_{fb}\rho u U + \tau_{cr}\frac{\sin(\varphi_x)}{\sin(\varphi_r)} - \frac{a\pi}{6} d \frac{\partial p_d}{\partial x} \ , \ \tau_{b,y} = k_t C_{fb}\rho v U + \tau_{cr}\frac{\sin(\varphi_y)}{\sin(\varphi_r)} - \frac{a\pi}{6} d \frac{\partial p_d}{\partial y} \tag{5.33}$$

where φ_x and φ_y are the bed slope angles in the x- and y-directions with the horizontal (positive values denoting downslope beds) respectively, φ_r is the sediment repose angle, p_d is the dynamic (non-hydrostatic) pressure near the bed and a is a coefficient assumed as $4/\pi$. Factor k_t was introduced by Wu and Wang (2007) due to high sediment concentration at the lower layer near the bed under dam-break flow conditions. Therefore, replacing the water density in the bed shear stress components, Eq. (5.32), with the mixture density near the bed leads to the following correction factor:

$$k_t = 1 + \frac{c_b \rho_s}{\left(1 - c_b\right)\rho} \tag{5.34}$$

5.5.4 Critical Shear Stress

The critical shear stress is calculated using the Wu et al. (2000b) relationship which was derived based on laboratory and field data as

$$\tau_{cr0} = 0.03\left(\gamma_s - \gamma\right)d \tag{5.35}$$

Since the original critical shear stress criterion was proposed for steady flows, estimating the critical shear stress in rapidly varied flows needs more considerations. The vertical component of the pressure-difference force changes the effective weight of particles in water and therefore the critical shear stress. Thus, the critical shear stress is corrected by introducing a correction factor as $\tau_{cr}=K_p\tau_{cr,0}$, where K_p is determined as (Wu 2007):

$$K_p = 1 + \frac{1}{(\rho_s - \rho)g}\frac{\partial p_d}{\partial z} \tag{5.36}$$

The submerged weight of moving particles above the bed produces a normal stress which is added to the critical shear stress (Bagnold 1954, Savari and Zech 2006, Zech et al. 2008). Therefore, the final relation for estimating the critical shear stress is:

$$\tau_{cr} = K_p \tau_{cr0} + (\rho_s - \rho) g H_s \tan\varphi_r \tag{5.37}$$

where H_s is the thickness of moving particles above the bed. Because the model calculates the suspended-load concentration and the bed-load transport rate separately, one can determine H_s as

$$H_s = q_b / u_b + \int_{z_b+\delta_b}^{z_s} c\,dz \tag{5.38}$$

5.5.5 Sediment Turbulent Diffusivity

The vertical profile of sediment turbulent diffusivity, ε_s, is usually related to the eddy viscosity by $\varepsilon_s = \nu_t/\sigma_c$, with σ_c being the Schmidt number which is between 0.5 and 1. This approach is adopted in the present model. An alternative way is the vertical profile of sediment diffusivity derived by van Rijn (1984b), which assumes a parabolic distribution in the lower half of the flow depth and a constant value in the upper half of the flow depth:

$$\varepsilon_s = \begin{cases} \kappa U_* \left(1-(z/h)\right) z/\sigma_s & z/h < 0.5 \\ 0.25\kappa U_* h/\sigma_s & z/h \geq 0.5 \end{cases} \tag{5.39}$$

where κ is the von Karman constant which typically is equal to 0.41 for clear water flow. Van Rijn (1984b) applied a damping factor to the von Karman constant in order to account for the effect of sediment concentration on the sediment-laden flow:

$$\kappa = 0.41\left[1+\left(c/c_0\right)^{0.8} - 2\left(c/c_0\right)^{0.4}\right] \tag{5.40}$$

where c is the sediment concentration by volume and c_0 is the maximum sediment concentration (=0.65).

5.5.6 Sediment Settling Velocity

The settling velocity in clear water is calculated using the following relation proposed by Wu and Wang (2006):

$$\omega_s = \frac{M\nu_m}{Nd}\left[\sqrt{\frac{1}{4}+\left(\frac{4N}{3M^2}D_*^3\right)^{1/n}} - \frac{1}{2}\right]^n \tag{5.41}$$

where $D_* = d[(\rho_s/\rho - 1)g/\nu_m^2]^{1/3}$, ν_m is the molecular viscosity of water, d is the nominal diameter or representative diameter in single-sized sediment transport calculations (in meter), $M = 53.5e^{-0.65SP}$, $N = 5.65e^{-2.5SP}$, and $n = 0.7+0.9S_P$ with S_P being the sediment particle shape factor. The effect of sediment concentration on the settling velocity is taken into account by the Richardson and Zaki (1954) relation as follows:

$$\omega_{sm} = (1-c)^4 \omega_s \tag{5.42}$$

where ω_{sm} is the settling velocity of sediment particles in turbid water.

5.5.7 Sediment Adaptation Length

The adaptation length is a characteristic distance for sediment to reach the equilibrium state from the non-equilibrium transport. It is an important parameter in the non-equilibrium sediment transport models. Several methods have been proposed to calculate the adaptation length. For example, the adaptation length of suspended load can be estimated as (Wu 2007)

$$L_s = \frac{uh}{\alpha \omega_s} \tag{5.43}$$

where α is the adaptation coefficient which is determined by calibration. Bell and Sutherland (1983) suggested that the bed load adaptation length L_b is related to the length of scour hole as a function of time t. Phillips and Sutherland (1989) proposed that L_b is a function of the particle size and the excess shear stress. The bed load adaptation length may take the average saltation step length of sand or the length of sand ripples if the bed is mainly covered by sand ripples. This approach was adopted by Nakagawa and Tsujimoto (1980) and Wu et al. (2000a). On the other hand, the bed-load adaptation length can be determined by model calibration based on measured data.

The existing formulas for calculating the adaptation length are based on experiments conducted in steady or quasi-steady flow conditions and thus may not be applicable to rapidly varied unsteady flows such as dam-break flow. The model developed in this study takes a constant calibrated value for the adaptation length of sediment.

5.5.8 Calibration Parameters

The developed model contains several uncertain parameters which can be investigated by sensitivity analysis. The most important parameters are the bed friction coefficient C_{fb} and the sediment adaptation length L. Savary and Zech (2006) showed that the bed friction coefficient can take a broad range of values based on the flow conditions and diameter of sediment particles. They calibrated the bed friction coefficient between about 0.07 and 0.25. Wu et al. (2012) calibrated the bed-load adaptation length as 0.025 m in their 2-D movable-bed dam-break flow model. Zhang et al. (2013) derived a theoretical relation to estimate the bed-load adaptation length. They used the proposed relation in a 1-D model and concluded that the bed-load adaptation length takes a small and approximately constant value at high shear stress zones. In this study, the bed friction coefficient and adaptation length are calibrated based on experimental measured data of dam-break flow.

5.6 Model Test

The developed model is tested using several laboratory experiments. The first test investigates the net entrainment of sediment by steady flow in a straight flume. In the second test case the model is tested using initial stages of dam-break flow over movable beds covered by sand and PVC pellets. Dam-break flow over movable bed in an abruptly expanded channel is the third case tested by the model. The last test is a partial dam-break flow over movable bed.

The simulations are carried out using two different computers including a desktop computer with operating system Windows 7, processor Intel Core i7-3.20 GHz, and Memory

(RAM) 24 GB, and a local server computer “Styx” at the National Center for Computational Hydroscience and Engineering, The University of Mississippi. The operating system of the server computer is Microsoft Windows Server 2012 Standard with processor Intel Xeon Core E5-3.10 GHz, and Memory (RAM) 128 GB. The source code is written in FORTRAN 90 programming language and runs on single CPU core.

5.6.1 Net Entrainment in a Straight Flume

The model is tested using an experiment reported by van Rijn (1981). The experimental study employed a flume 30 long, 0.5 m wide and 0.7 m deep. Clear water was initially flowed over the sand bed of the flume and entrained sediment into suspension until the full transport capacity was acquired. The bed material consisted of sand particles with d_{50}=0.23. The water depth in the flume was 0.25 m and the mean velocity 0.67 m/s. Since the model considers single-sized sediment transport, a representative particle size of 0.2 mm is used, following Wu et al. (2000a). The computational domain is divided to 252,000 hexahedral cells. The model uses the sediment density, shape factor, and porosity equal to 2650 kg/m^3, 0.7, and 0.4, respectively. The Schmidt number is equal to 0.8 in this test and other tests in the next sub-sections. The coefficient C_{fb} is calibrated as 0.05. The bed-load adaptation length is 0.025 m.

Fig. 5.4 compares the calculated and measured vertical profiles of sediment concentration at four different cross sections. It can be seen that the general agreement is fairly good. The sediment concentration at the boundary between the suspended-load and bed-load zones tends to a high concentration, whereas it tends to zero at the water surface.

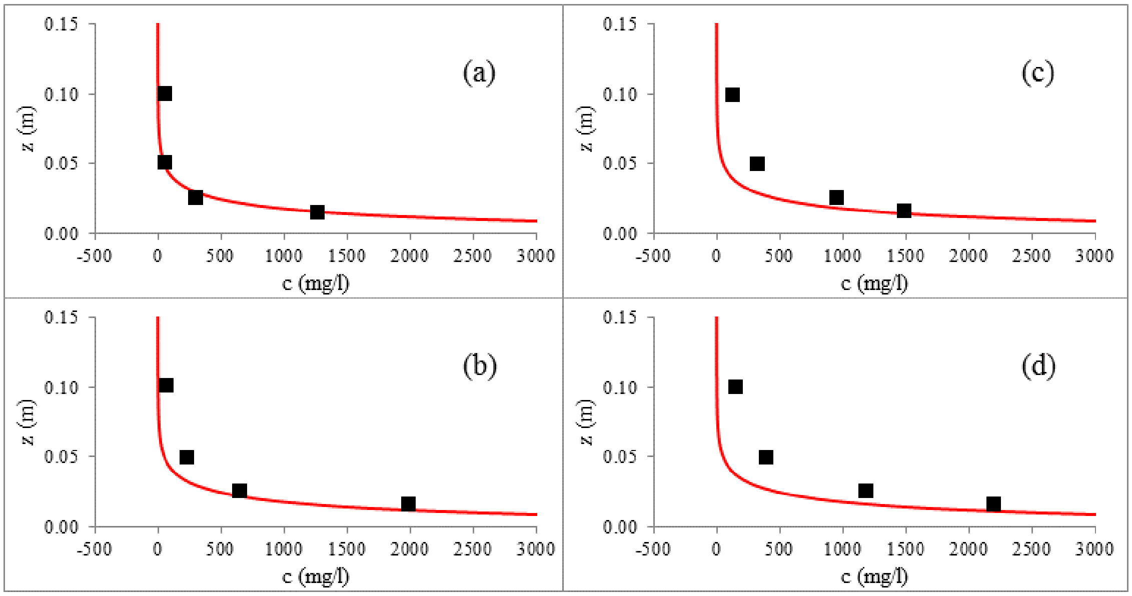

Fig. 5.4 Vertical distribution of sediment concentration at (a) x/*h*=4, (b) x/*h*=10, (c) x/*h*=20, and (d) x/*h*=40 (solid line: calculated, squares: measurements from Van Rijn 1981)

5.6.2 Initial Stage of Dam-Break Flow over Movable Beds

The model is tested using two experimental cases of small-scale dam-break flows on movable beds. These cases are chosen to investigate the ability of the model to predict the near-field response of a movable bed to dam-break waves. The first experiment was carried out at the Université Catholique de Louvain (UCL) (Spinewine and Zech, 2007). The experiment was performed in a flume 6 m long, 0.25 m wide and 0.7 m high and the entire bed was covered by natural sand. A gate was located at the center of the flume. The gate was 6 mm thick and made of a layered aluminum structure fitted on its circumference with a hollow PVC seal. In the experiment the instantaneous dam collapse was duplicated by a lowering of the gate to minimize perturbation to the sediments and water during the gate removal. Different initial conditions were investigated by adjusting the upstream and downstream water and sediment depths. Herein experiment 'sand (a)' which is shown in Fig. 5.5, is chosen to validate the ability of the developed model to simulate initial stages of dam-break flow over movable beds. The initial water depth in the reservoir was 0.35 m and the downstream reach was dry. The flume was covered by saturated uniform coarse sand. The sediment particles had the following properties: d_{50}=1.82 mm, density=2683 kg/m^3, friction angle=30°, and porosity=47%.

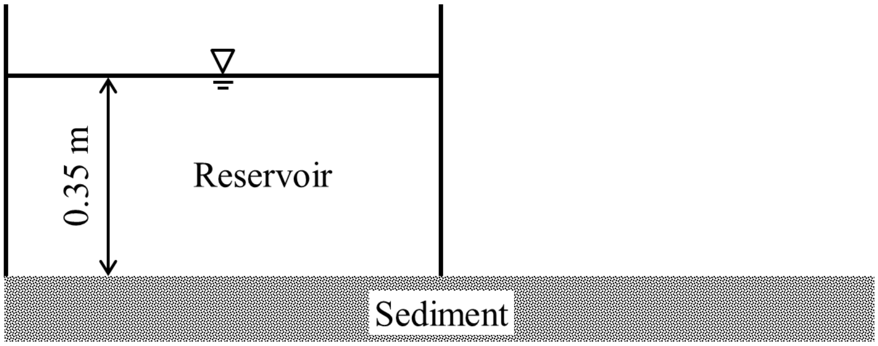

Fig. 5.5 Initial dam-break configuration conducted by Spinewine and Zech (2007)

The computational domain contains 37 vertical layers and the grid spacing is equal to 1.5 and 1 cm in the horizontal and vertical directions, respectively. The bed friction coefficient C_{fb} and the adaptation length L are set equal to 0.15 and 0.025 m, respectively. These values were chosen by a calibration process. The same adaptation length was used by Wu et al. (2012) in their 2-D dam-break flow model on movable bed covered by sand with nearly similar properties to the sand used in this experimental case. The simulations were carried out on the desktop computer and the average execution time was about 25 min for 1.6 s simulation.

The comparisons between the measured and calculated water surface and bed profiles are shown in Fig. 5.6 and 5.7. The comparison demonstrates the ability of the model to simulate the initial stages of water surface profile, bed changes, and bed forms caused by dam-break flow fairly well.

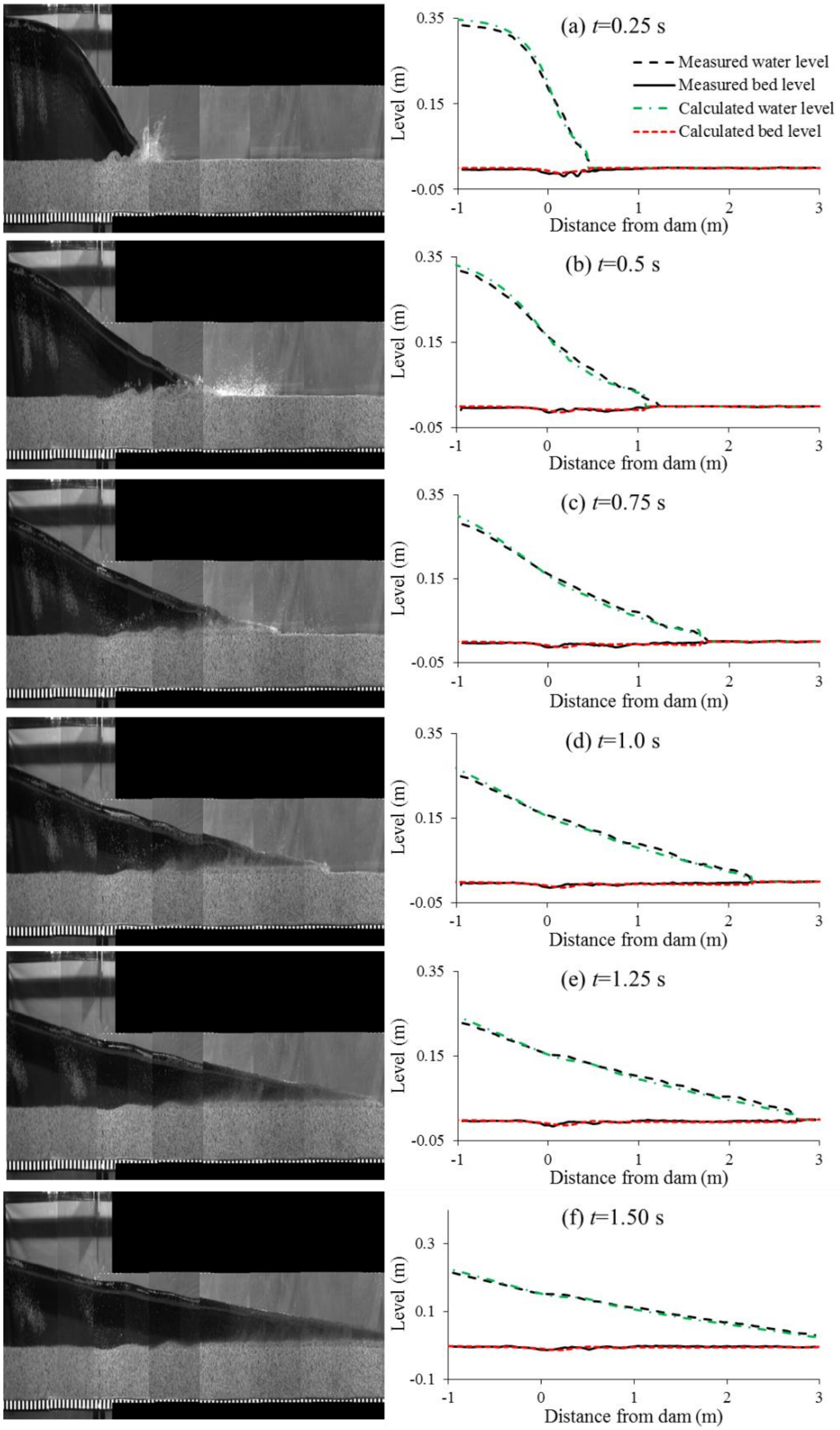

Fig. 5.6 Comparison between measured and calculated (using C_{fb}=0.15 and L=0.025 m) water surface and bed profiles (measurements and snapshots from Spinewine and Zech, 2007)

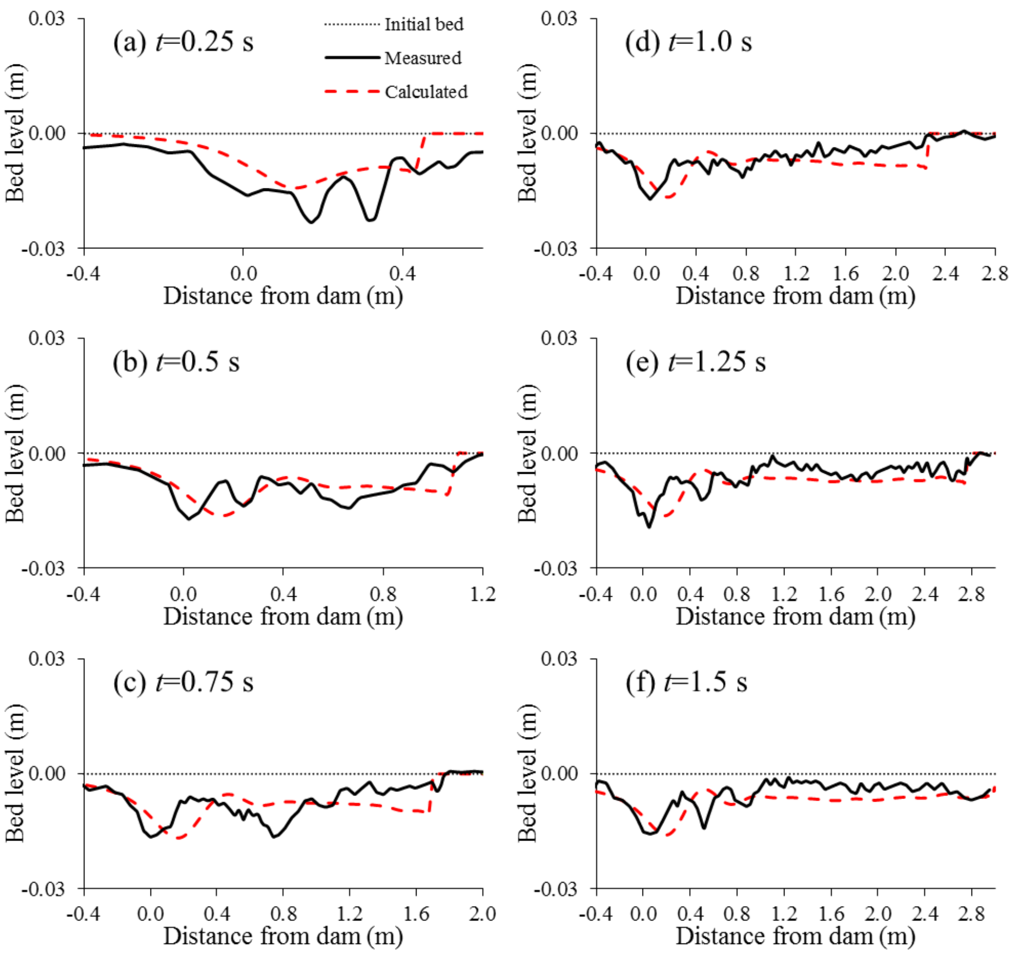

Fig. 5.7 Comparison between measured and calculated (using C_{fb}=0.15 and L=0.025 m) bed profiles (measurements from Spinewine and Zech, 2007)

The sensitivity of the model to the adaptation length is investigated. The comparison of calculated bed profiles for adaptation lengths of 0.025, 0.05, and 0.1 m are shown in Fig. 5.8. The friction coefficient was kept equal to 0.15. The comparison reveals that the effect of adaptation length on bed elevation is considerable. A larger adaptation length results in less bed erosion. Moreover, when the model uses a smaller adaptation length, the bed forms generated by the dam-break wave are more intense.

Sediment transport caused by dam-break flow is in strongly non-equilibrium state and it is necessary to estimate the sediment adaptation length carefully.

The model sensitivity to the bed friction coefficient is investigated by changing the bed friction coefficient while the adaptation length is kept the same. Fig. 5.9 shows the comparison of the bed profiles calculated with different values (0.1, 0.15, and 0.2) of bed friction coefficient. As the bed friction coefficient increases, the effective bed shear stress increases and in turn more erosion occurs. The effect of bed friction coefficient on the bed elevation change is more significant during the initial stages of dam break (until t=0.5 s) when the sediment transport process is highly in non-equilibrium state. After the sudden opening of the gate, the dam-break wave front, which contains of clear water, entrains considerable amount of sediment particles from the bed and causes deep erosion near the gate site. As the wave propagates downstream, the water continues to entrain more sediment particles and thus acts as a debris flow with high sediment contraction, in which the difference between the actual and equilibrium sediment concentrations becomes less. In other words, the actual sediment concentration in the downstream wave front is closer to the equilibrium state, which results to less bed erosion, compared with the significant erosion near the gate site.

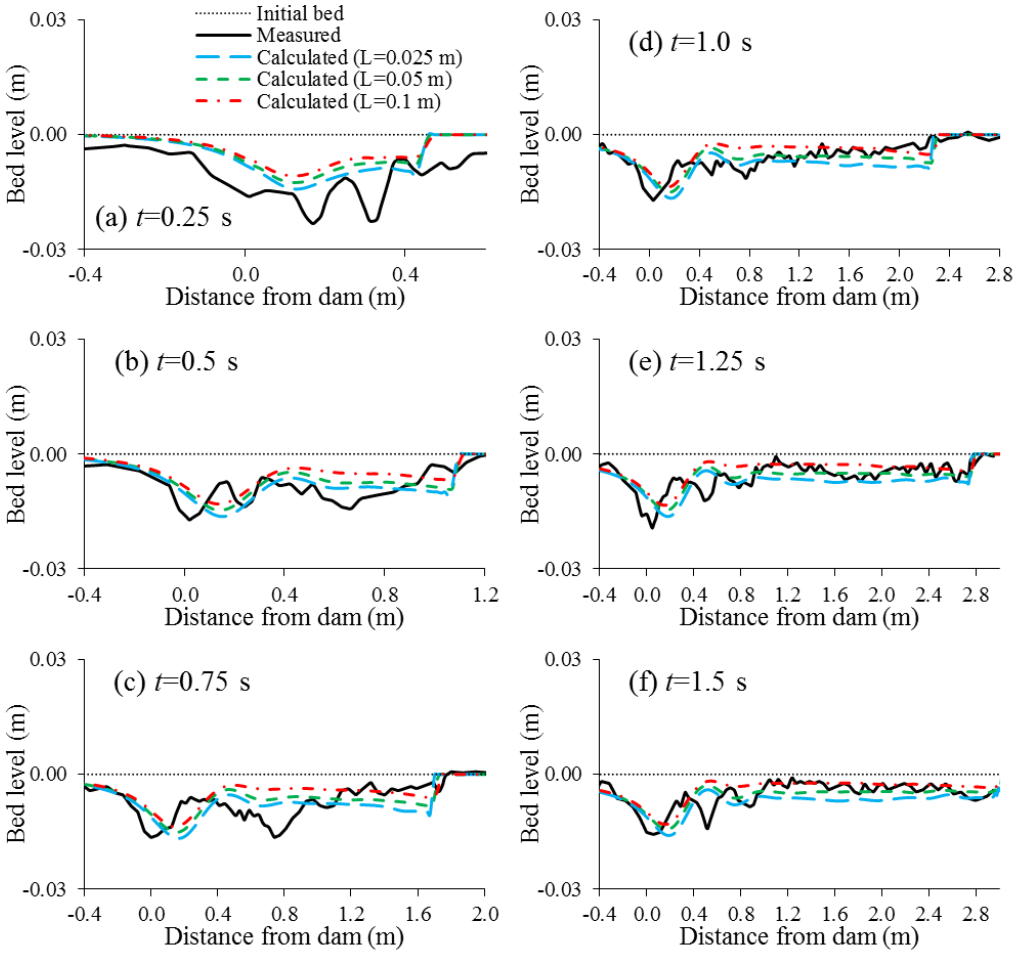

Fig. 5.8 Sensitivity analysis of bed elevation change to varying adaptation length

(C_{fb}=0.15, measurements from Spinewine and Zech, 2007)

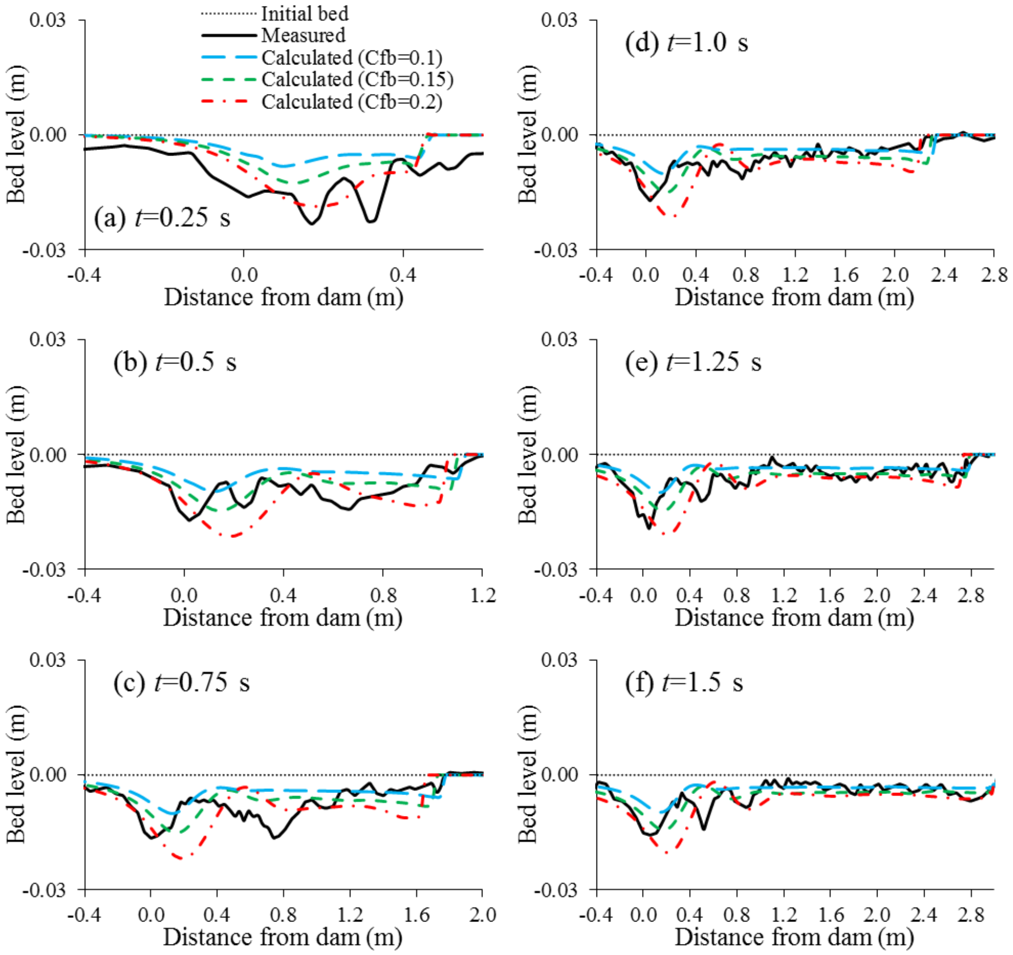

Fig. 5.9 Sensitivity analysis of bed elevation change to varying bed friction coefficient

(L=0.05 m, measurements from Spinewine and Zech, 2007)

The model is also tested using the small-scale experimental dam-break flow on movable beds performed in Louvain-la-Neuve, UCL (Fraccarollo and Capart, 2002). The test reach was 2.5 m long, 0.1 m wide, and 0.35 m high. The flume bed was covered by light cylindrical Polyvinyl Chloride (PVC) pellets with an equivalent spherical diameter of 3.5 mm, density of 1540 kg/m^3, and fall velocity of 18 cm/s. The sediment porosity was not reported in the original paper and herein it is assumed to be equal to 50%. This value falls in the range of porosity of PVC pellets used by Spinewine and Zech (2007) and Capart and Young (1998).The initial water depth in the reservoir was 0.1 m and the downstream was dry. The computational domain contains hexahedral cells with grid spacing equal to 0.75 cm in horizontal and vertical directions. The computational mesh uses 16 vertical layers. The friction coefficient and adaptation length are calibrated as 0.35 and 0.05 m, respectively. The bigger values of friction coefficient and adaptation length are because the PVC pellets are bigger in diameter compared to the natural sand used in the previous test. A bigger adaptation length was used by Wu and Wang (2007) for PVC pellets. The simulations were carried out on the desktop computer and the average execution time was about 5 min for 1.1 s simulation.

The calculated water surface and bed profiles are compared with measured ones in Fig. 5.10. The bed profiles are predicted by the model accurately. The water surface forms a hydraulic jump at the gate location. It can be seen that the model underestimates the height of the jump especially in the very beginning of the simulation. Since the bed is covered by light PVC particles, the bed is eroded significantly immediately after gate opens. The eroded particles are entrained by the flow and transported with high intensity near the wave front. The trapped particles by the dam-break wave occupy the whole flow depth densely near the wave front which can be interpreted as nearly water and debris. Therefore, the wave front behaves as debris flow (Capart and Young 1998). Under debris flow condition, intense grain-grain interactions occur which leads to an injection of vorticity and air bubbles into the water. Figure 5.11 shows the existence of dense particles near the wave front.

The sensitivity of calculated bed profiles to the adaptation length and the bed friction coefficient is shown in Figs. 5.12 and 5.13. A smaller adaptation length results in more erosion. The sensitivity analysis of the bed friction coefficient indicates that using a small value results in a reduction of the effective shear stress and in turn underestimation of the erosion magnitude, especially in the vicinity of the dam location. However, the bed profiles downstream of the dam location are not significantly different, because of the fact that the wave front carries sediment particles with a high concentration acting as a debris flow, the difference between the actual and equilibrium sediment concentrations is less (or the actual sediment concentration is close to the equilibrium state).

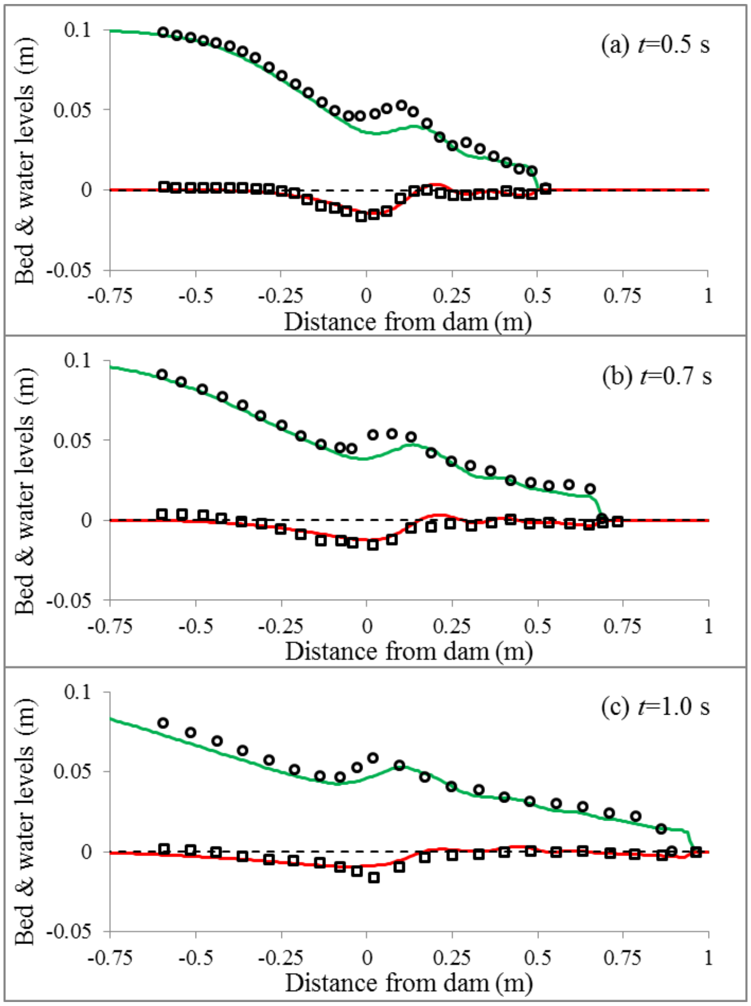

Fig. 5.10 Comparison between measured (symbols) and calculated (using C_{fb}=0.35 and L=0.05 m; solid lines) water surface and bed profiles (measurements from Fraccarollo and Capart, 2002)

Fig. 5.11 Wave front with high sediment load at the initial stage of gate removal *t*=0.25 s (picture from Fraccarollo and Capart, 2002)

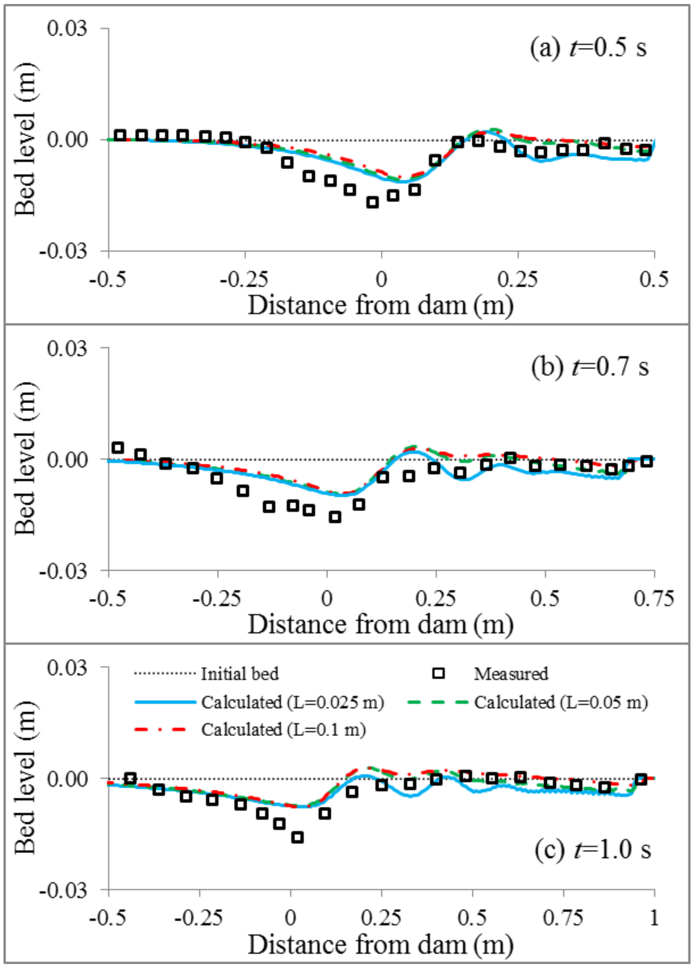

Fig. 5.12 Sensitivity analysis of bed elevation change to varying adaptation length (C_{fb}=0.2, measurements from Fraccarollo and Capart, 2002)

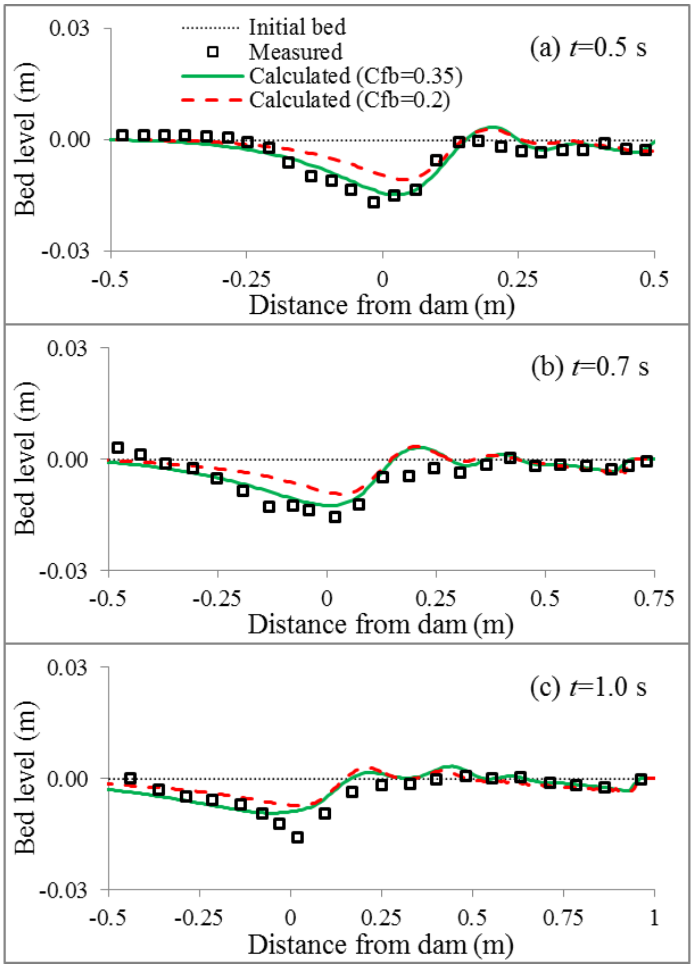

Fig. 5.13 Sensitivity analysis of bed elevation change to varying bed friction coefficient

(*L*=0.05 m, measurements from Spinewine and Zech, 2007)

5.6.3 Dam-Break Flow over Movable Bed in an Abruptly Expanded Channel

The model is also tested using an experiment of dam-break flow over a movable bed in an abruptly expanded channel to investigate the far-field responses of an erodible bed to dam-break waves. The experiment was conducted at the UCL, Belgium (Goutiere et al. 2011) by means of a 6 m long flume with an abrupt expansion from 0.25 to 0.5 m, located 1 m downstream of the gate as shown in Fig. 5.14. The side walls of the flume were made of glass. The dam break was simulated by a rapid downward movement of a thin gate located 1 m upstream of the expansion. The entire flume bed was covered by 0.1 m thick uniform coarse sand which was fully saturated. The sediment properties were: a median diameter of 1.72 mm, a specific density of 2.63, and a deposit porosity of 39%. The initial water depths upstream and downstream of the gate were 0.25 and 0 m, respectively. The downstream end of the flume was a free outlet. The horizontal grid spacing is equal to 1 cm downstream of the gate and increased gradually in upstream direction. The vertical grid consists of 27 layers with the grid spacing equal to 1 cm. The calibrated bed friction coefficient and adaptation length are 0.2 and 0.025 m, respectively. The simulations were carried out on the desktop computer. The average execution time was about 107 hr to simulate this experimental test which lasted 12 s.

The water surface time series were measured by nine ultrasonic gages placed downstream of the gate. The positions of gages are summarized in Table 5.1. The morphological changes generated by the dam-break flow were also measured downstream of the expansion.

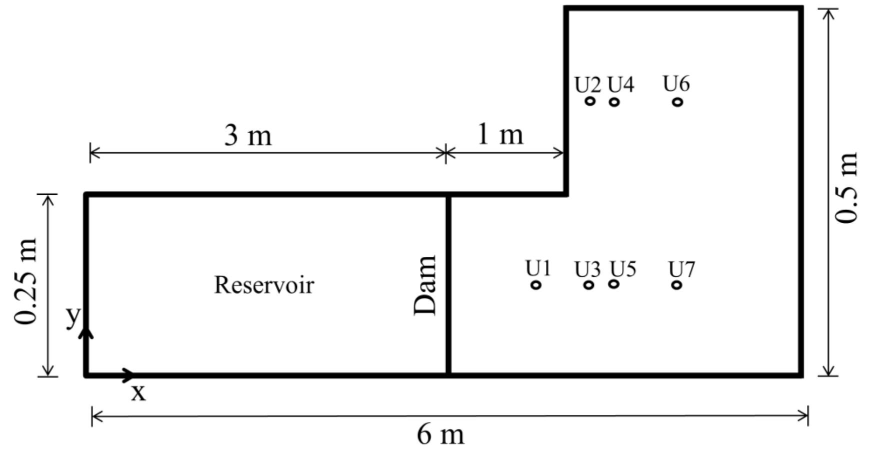

Fig. 5.14 Plan view of experimental setup (dam-break flow over movable bed in an abruptly expanded channel)

Table 5.1 Location of measurement gages

Position (m)	U1	U2	U3	U4	U5	U6	U7
x	3.75	4.2	4.2	4.45	4.45	4.7	4.7
y	0.125	0.375	0.125	0.375	0.125	0.375	0.125

Fig. 5.15 shows the calculated water surface level at t=2.3 s. Once the dam-break wave arrives at the expansion it spreads to the left side of the flume. The diverted wave hits the left wall downstream of the expansion and generates a hydraulic jump. Fig. 5.16 shows the comparison between measured and calculated water surface time series at gages U1, U2, U3, U6, and U7. It can be seen that the peak value of water level and the propagation trend of the wave are predicted well by the model.

Fig. 5.17 and 5.18 show the magnitude of resultant velocity near the flume bed and the flow pattern at t=3.3 s, respectively. The velocity magnitude is big at the expansion zone and becomes small downstream of the expansion. Flow recirculation occurs at the corner of expansion.

The final bed topography calculated by the model is compared with the measured one in Fig. 5.19. Both measured and calculated maps show erosion near the corner of the expansion and deposition at downstream of the expansion zone. As the dam-break wave propagates in the straight flume before the expansion, the lateral component of shear force is insignificant. When the wave reaches to the expansion zone, the wave is diverted to the left side of the flume and the lateral component of shear force becomes significant. The bed shear force magnitude and gradient increase and therefore bed erosion occurs in regions close to the expansion. As the wave propagates farther downstream, the flow strength decreases and the entrained sediment particles deposit. Figs. 5.20 and 5.21 compare the measured and calculated final bed level profiles at six cross sections downstream of the expansion for different values of adaptation length and bed friction coefficient. The comparisons show that the model is able to predict generally well the magnitude and distribution of erosion and deposition, and in turn the bed topography.

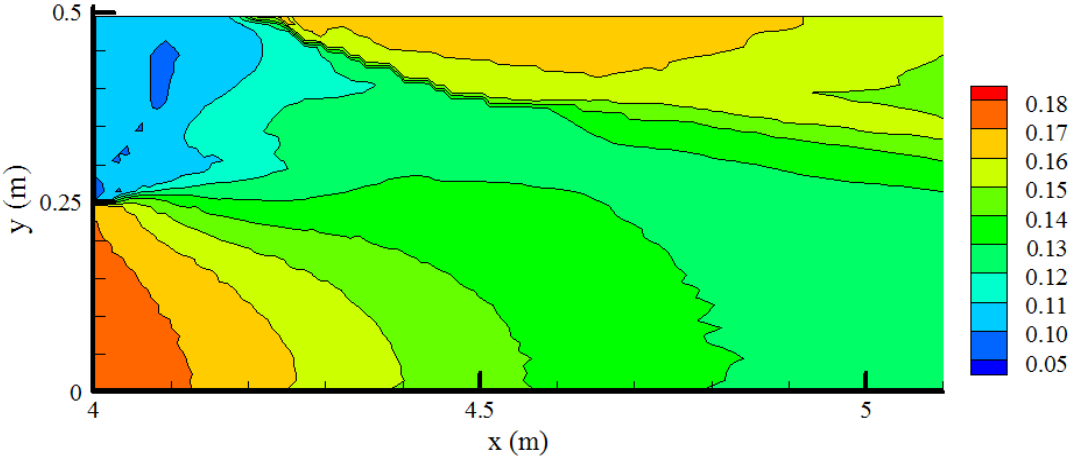

Fig. 5.15 Calculated water surface level (in meter) downstream of the expansion zone at t=2.3 s (C_{fb}=0.2 and L=0.025 m)

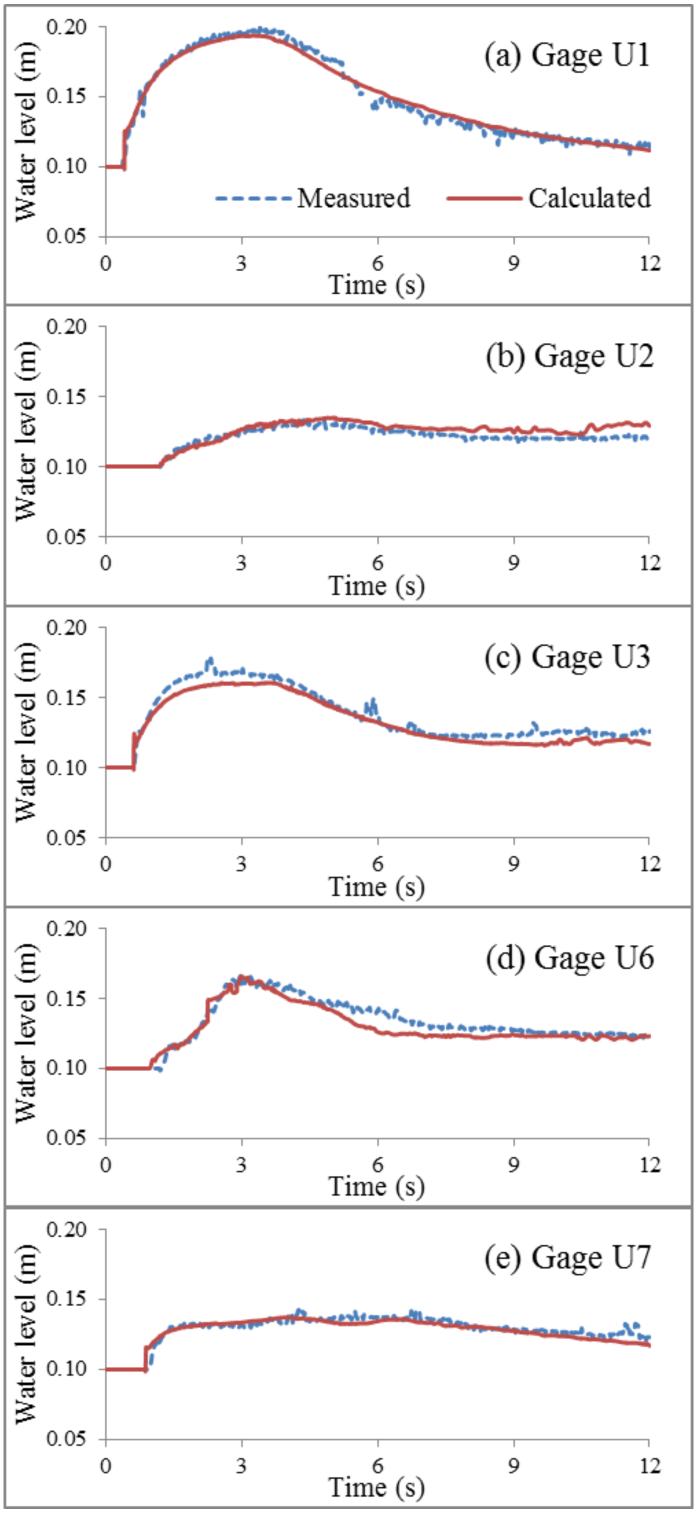

Fig. 5.16 Measured and calculated water surface time series (C_{fb}=0.2 and L=0.025 m)

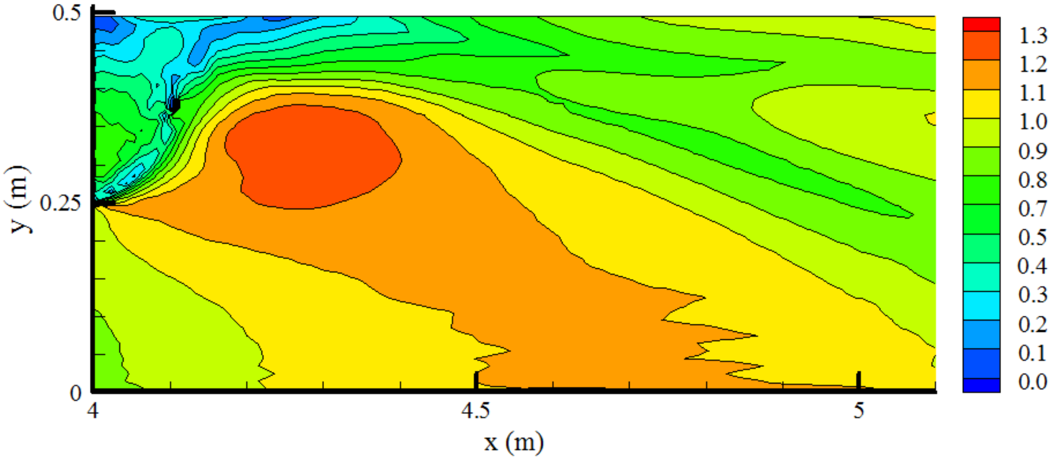

Fig. 5.17 Magnitude of calculated resultant velocity (in m/s) near the bed downstream of the expansion zone at t=3.3 s (C_{fb}=0.2 and L=0.025 m)

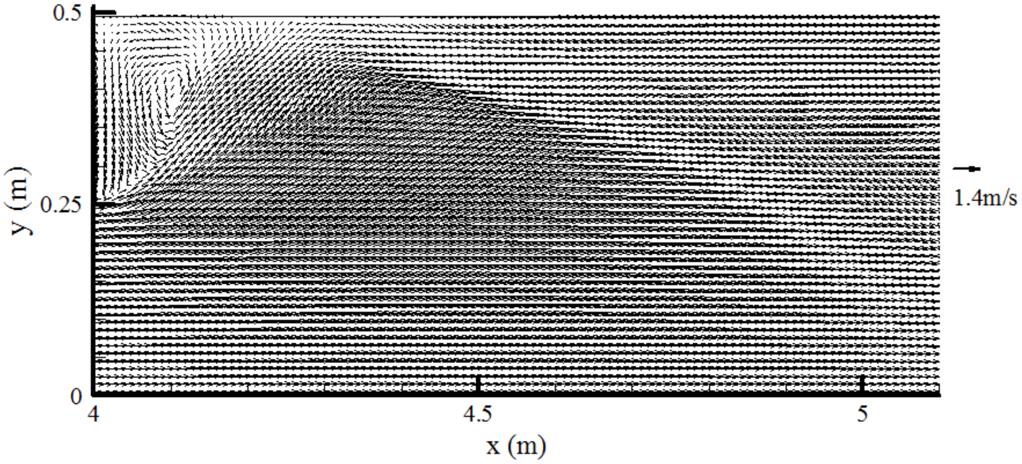

Fig. 5.18 Flow pattern downstream of the expansion zone at t=3.3 s (C_{fb}=0.2 and L=0.025 m)

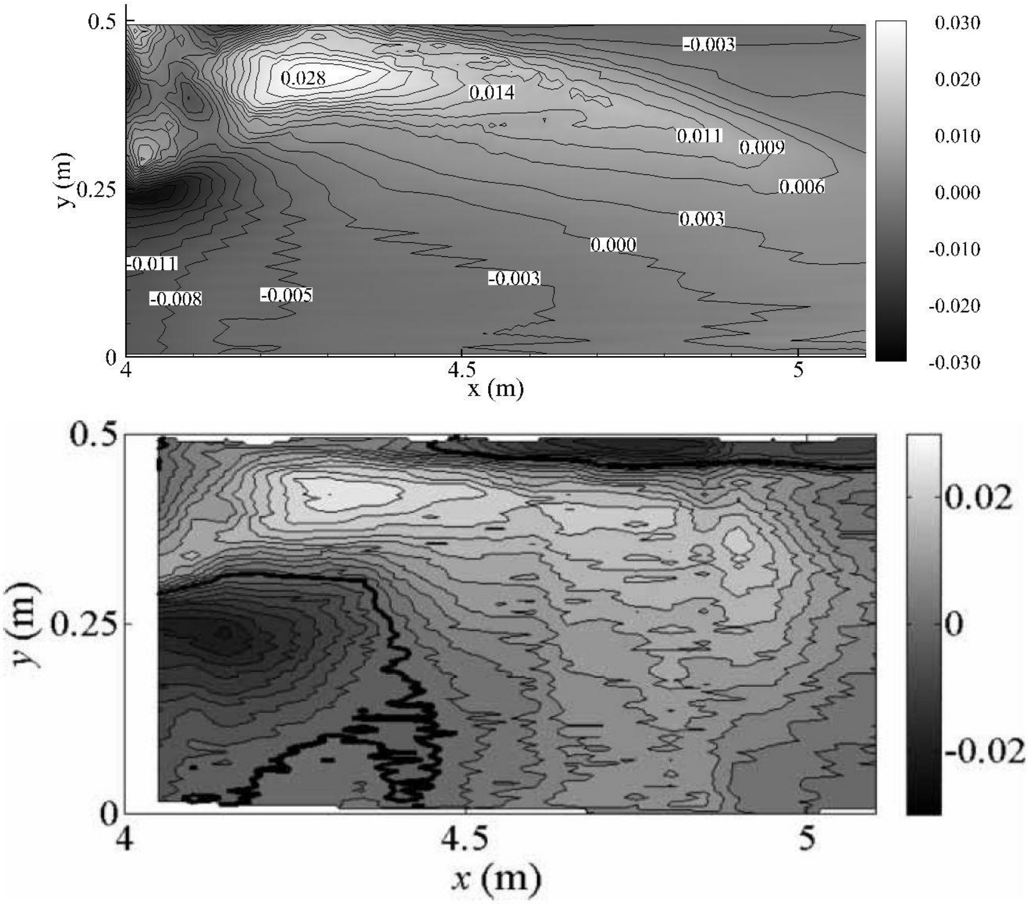

Fig. 5.19 Final bed topographies (units in meter) downstream of the expansion, top map: calculated (using C_{fb}=0.2, L=0.025 m), bottom map: measured (measurements from Goutiere et al. 2011)

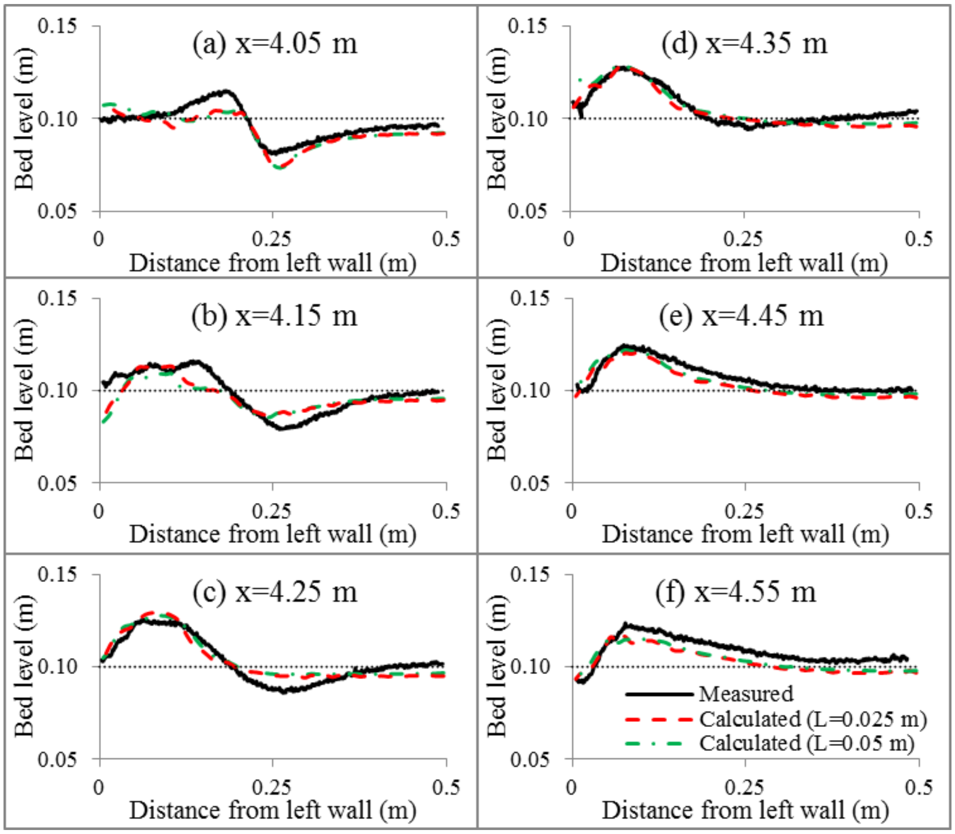

Fig. 5.20 Measured and calculated cross sections of final bed

(C_{fb}=0.2, dotted line: initial bed level)

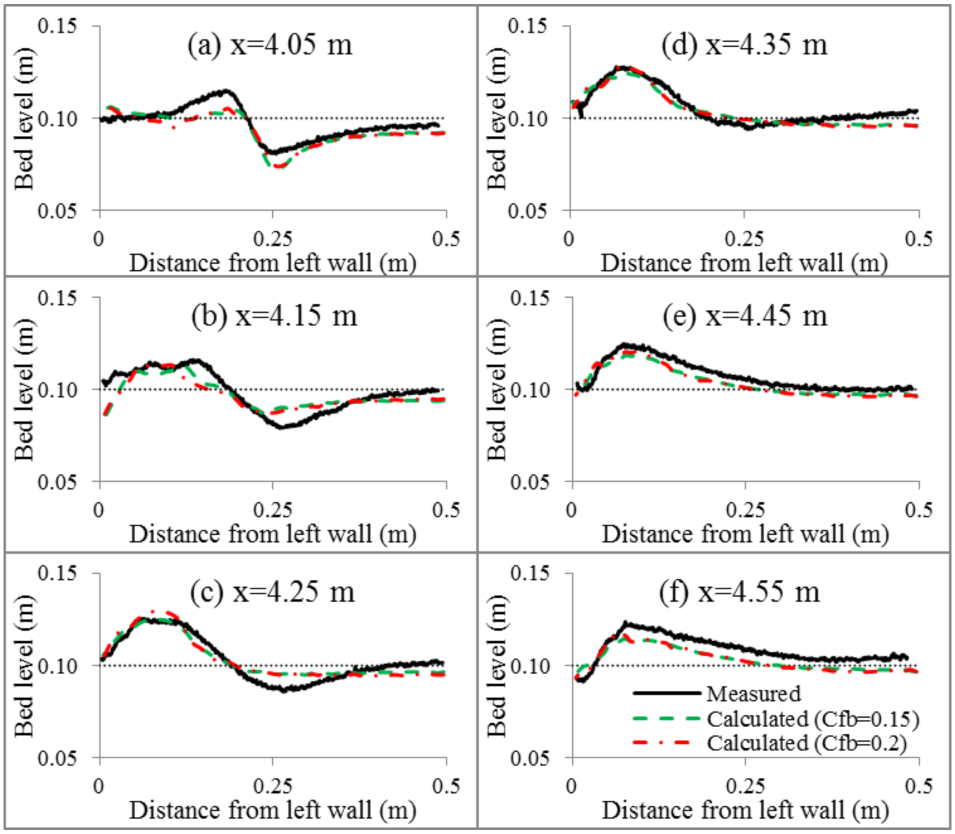

Fig. 5.21 Measured and calculated cross sections of final bed

(*L*=0.025 m, dotted line: initial bed level)

5.6.4 Partial Dam-Break Flow over Movable Bed

The model is also tested using a benchmark experiment carried out at the Hydraulic Unit of the Mechanical and Civil Engineering Laboratory, UCL, to investigate partial dam-break flow over movable bed (IAHR working group, 2012). The flume was 36 m long and 3.6 m wide, as shown in Fig. 5.22. The partial dam break was represented by two impervious blocks and a 1-m wide gate placed between the blocks 12 m from the upstream flume end. The gate was pulled up rapidly to mimic an instantaneous dam break event. The rigid bed of the flume was covered with an 85-mm-thick sand layer extended from 1 m upstream of the gate to 9 m downstream of the gate. The used sand was uniform, fully saturated and uncompacted. The median diameter of sediment was 1.61 mm, specific gravity 2.63, and initial porosity 0.42. The physical boundaries consisted of a closed wall at the upstream flume end and a weir and sediment entrapment system at the downstream end. The experiment lasted for 20 s. The initial water depth inside the reservoir was 0.47 m and the downstream reach was dry. The time evolution of water level was measured using Baumer™ ultrasonic probes at eight gages located downstream of the gate shown in Fig. 5.18. At the end of the experiment the bed elevation was measured using a Delft bed profiler over the whole flume width between 0.5 m and 8 m downstream of the gate. The repeatability of the experiment was investigated by comparing the measured water level time series and bed profiles from different experimental runs. The computational mesh consists of about 700,000 hexahedral cells with non-uniform horizontal grid spacing between 25 and 5 cm and of 21 uniform vertical layers with grid spacing equal to 2.5 cm. The horizontal grid spacing near the gate is 5 cm and increases in downstream and upstream directions. The calibrated bed friction coefficient and adaptation length are 0.2 and 0.025 m, respectively. The simulations were carried out on the local server computer and the average execution time was about 136 hr for 20 s simulation.

Fig. 5.23 shows the snapshot of the calculated water surface level downstream of the partial opening at t=3 s. As the dam-break wave propagates downstream of the dam it spreads to the sides of the flume, hits the side walls, and generates hydraulic jumps. The time evolution of water surface is shown in Fig. 5.24. The water surface time series show slightly oscillatory behavior at gages 2 and 3 which might be because of the rapid changes of bed elevation in the vicinity of the partial opening. The oscillatory behavior of measured and calculated water surfaces is more significant at the corner of partial opening where gages 1 and 4 are located. IAHR working group (2012) demonstrated that the measured water surface level at gage 1 shows similar oscillatory pattern in different experimental runs.

The magnitude of the resultant velocity near the bed at *t*=3 s is shown in Fig. 5.25. It indicates that the velocity magnitude is high near the opening which leads to high bed shear stress and strong bed erosion as shown in Fig. 5.26 which compares the measured and calculated final bed topographies. Both measured and calculated results show significant erosion downstream of the dam and deposition at zones near the side walls of the flume. The significant erosion occurs in front of the partial opening as a result of high bed shear stress. As dam-break wave spreads to the sides of the flume the flow strength decreases and deposition occurs at downstream and sides of the flume.

Fig. 5.27 shows the measured and calculated bed profiles along the longitudinal sections of y=0.2, 0.7 and 1.45 m away from the flume center. The measured bed profiles are plotted for two different experimental runs. IAHR working group (2012) showed that the measured bed profiles differ in different runs with the same experiment setup. The calculated bed profiles are plotted for two different values of adaptation length. The comparison between measured and calculated bed profiles reveals that the magnitude of bed erosion in front of the opening and deposition at downstream calculated by *L*=0.05 m is slightly smaller than the calculated ones by *L*=0.025 m.

Fig. 5.28 shows the sensitivity of calculated bed profile to bed friction coefficient, which is set as 0.1 and 0.2. The change in bed friction coefficient from 0.2 to 0.1 results in significantly less bed erosion and deposition. The smaller value of bed friction coefficient leads to underestimating the effective bed shear stress which is the driving force to erode the bed, and consequently generates less deposition at downstream of the flume. Therefore, calibrating the bed friction coefficient plays an important role in predicting the magnitude of bed erosion and deposition. In addition, the discrepancy in bed profiles measured by different experimental runs reveals the fact that sediment transport under dam-break flows is highly complex and depends on probabilistic factors.

Considering the complicated aspects of sediment transport under dam-break flow, the model reproduces the erosion and deposition patterns generally well.

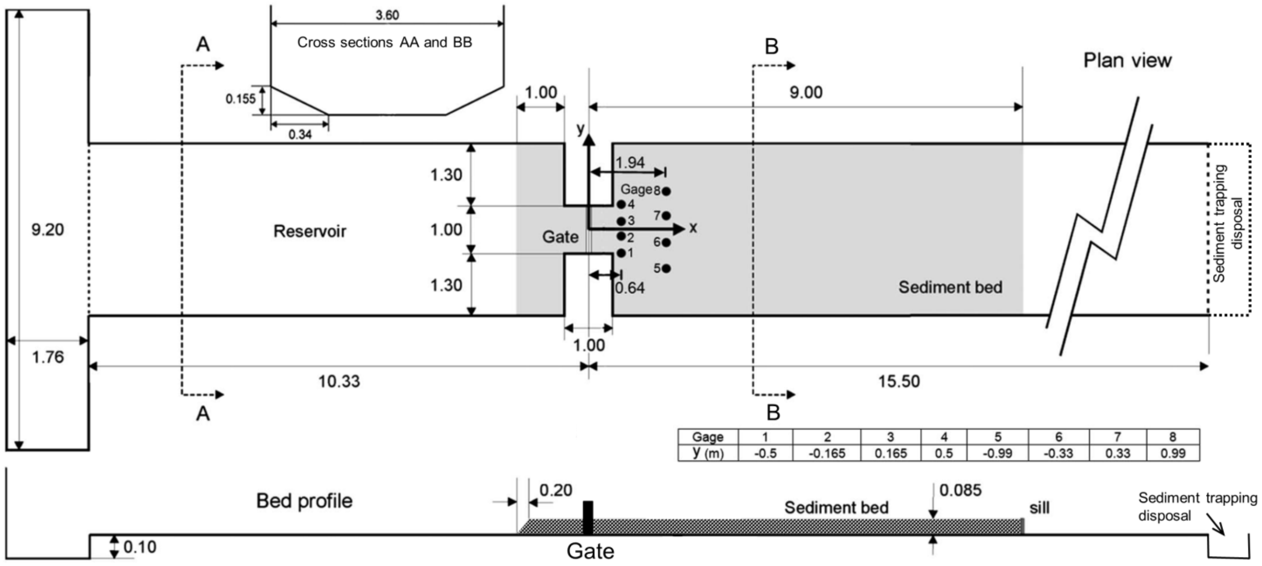

Gage	1	2	3	4	5	6	7	8
y (m)	-0.5	-0.165	0.165	0.5	-0.99	-0.33	0.33	0.99

Fig. 5.22 Plan view of experimental setup (partial dam-break flow over movable bed)

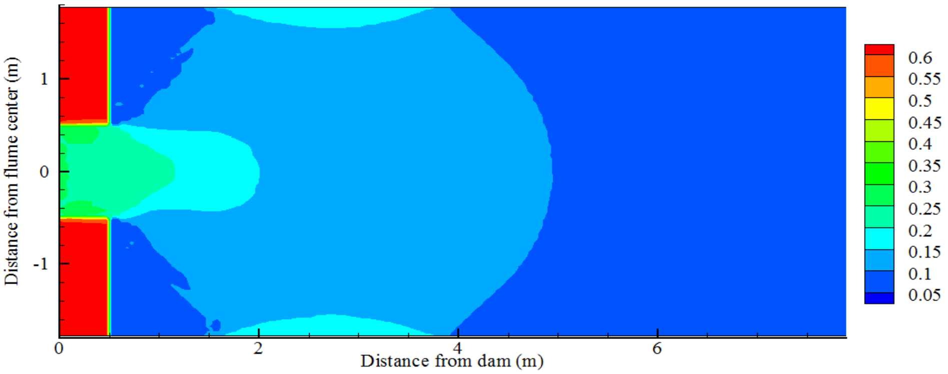

Fig. 5.23 Calculated water surface level (in meter) downstream of the dam at t=3 s

(C_{fb}=0.2 and L=0.025 m)

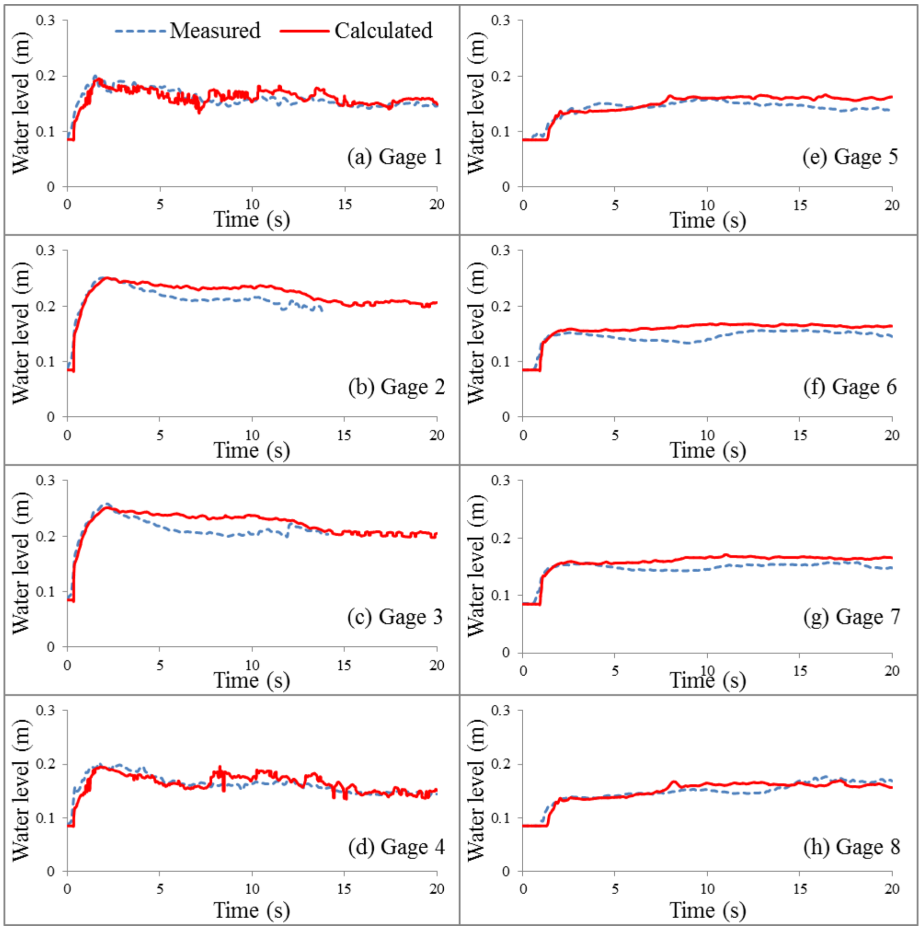

Fig. 5.24 Measured and calculated water surface time series (C_{fb}=0.2 and L=0.025 m)

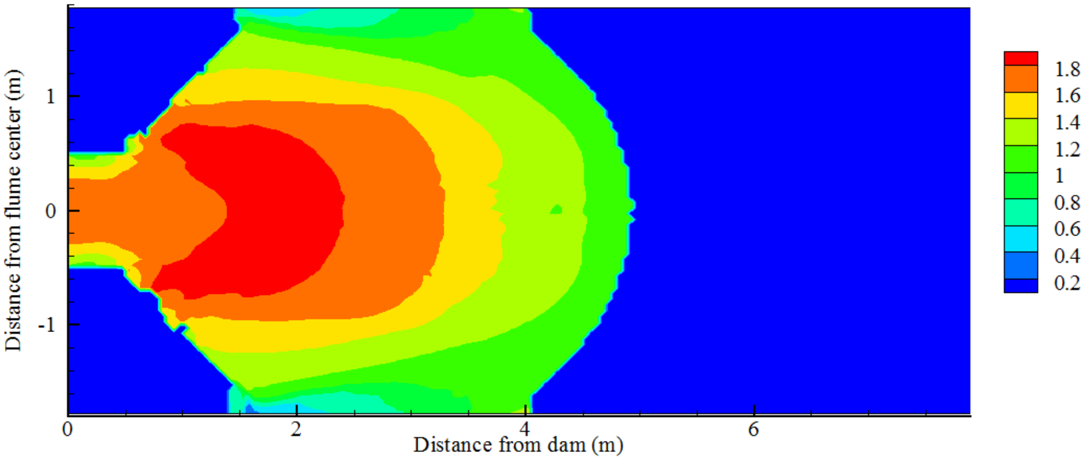

Fig. 5.25 Magnitude of calculated resultant velocity (in m/s) near the bed downstream of the dam at t=3 s (C_{fb}=0.2 and L=0.025 m)

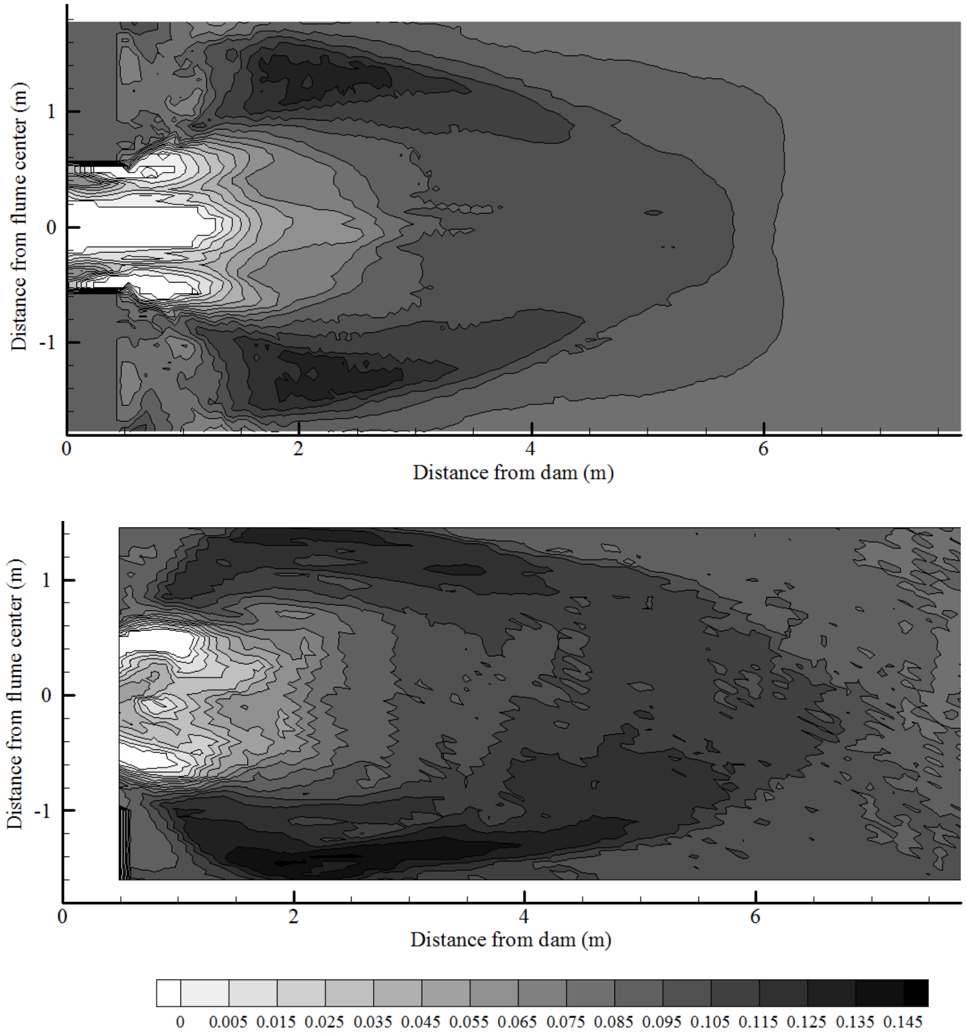

Fig. 5.26 Final bed topographies (units in meter) downstream of the dam, top map: calculated (using C_{fb}=0.2, L=0.025 m), bottom map: measured (IAHR working group, 2012)

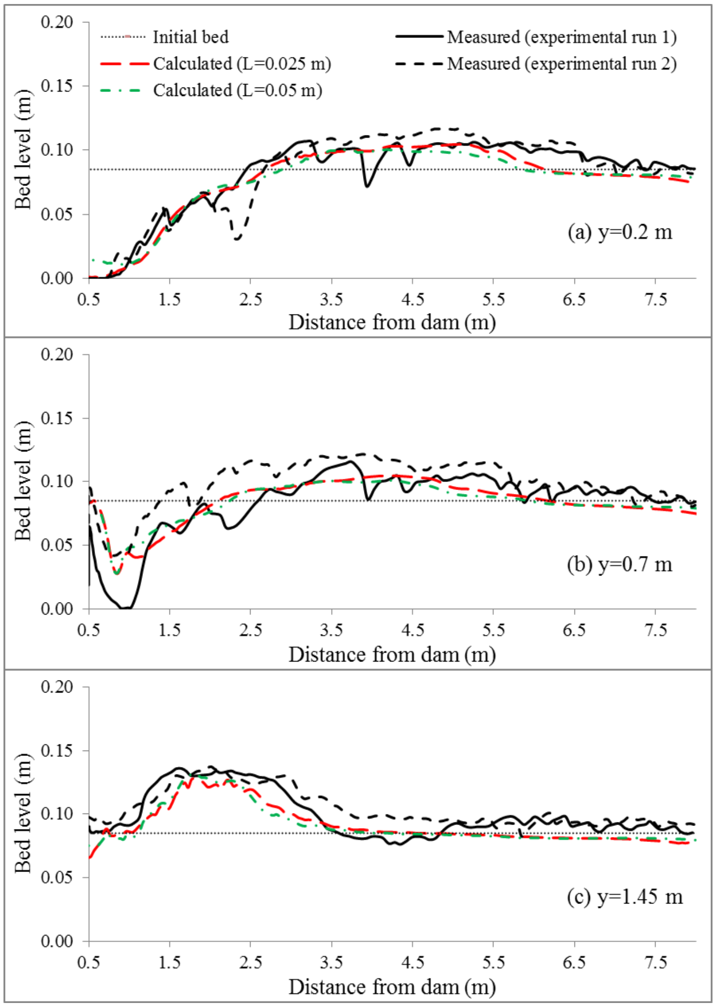

Fig. 5.27 Measured and calculated final longitudinal bed profiles (C_{fb}=0.2)

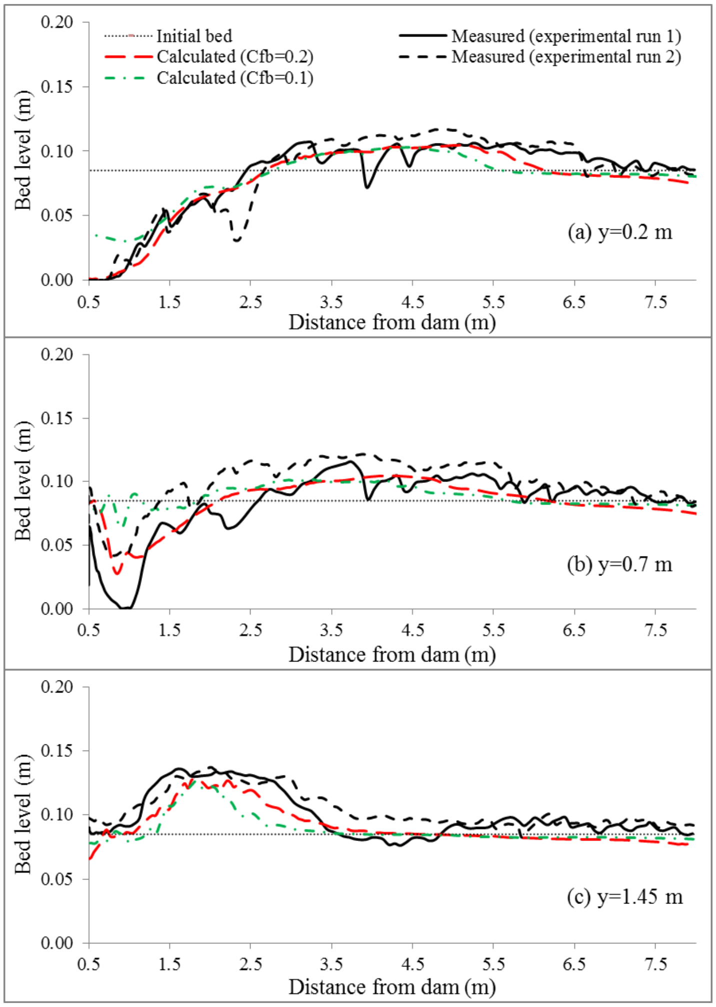

Fig. 5.28 Measured and calculated final longitudinal bed profiles (*L*=0.025 m)

5.7 Summary

In this chapter, a 3-D sediment transport model was developed to calculate bed changes induced by dam-break flows. The model solves governing equations of suspended-load, bed-load transport, and bed change. The developed sediment transport model is integrated with the 3-D finite-volume hydrodynamic model presented in Chapter 4 in order to simulate dam-break flows on movable beds. To consider the effects of bed changes on hydrodynamic calculations, the model uses a moving grid technique to update the computational grid to fit with the calculated bed topography at every time step. The grid vertical velocity generated by the moving mesh is added to the convective terms, and the cell volume change is considered in discretization of the temporal terms.

The integrated hydrodynamic and sediment transport model is tested using several experimental dam-break flows on movable beds. The model is tested using two small scale experimental dam-break flows on beds covered by natural sand and PVC pellets. The model was also tested using two 3-D experimental dam-break flows on movable beds covered by natural sand. The comparisons showed a good agreement between measured and calculated water surface time series and bed profiles.

CHAPTER 6

SUMMARY, CONSLUSIONS, AND FUTURE RESEARCH

6.1 Summary and Conclusions

In this PhD dissertation dam-break flows on fixed and movable beds were studied numerically. The first achievement, as presented in Chapter 3, was developing a 3-D numerical model based on the finite-difference method with rectilinear grid to study propagation of dam-break waves over non-erodible beds with simple geometry. The model solves the RANS equations explicitly by means of SOR method and uses the Smagorinsky turbulence model to calculate the eddy viscosity. The SOLA-VOF technique is adopted to track the water surface movements. It was found that the VOF stability condition is dominant to control the computational time step. The model was tested using several experimental dam-break flows. The calculated results revealed the capability of VOF technique to treat the moving boundary problem raised by rapid movements of water surface in dam-break flows.

The major goal sought by this dissertation was developing a 3-D numerical model of dam-break flows over irregular and movable beds. The finite-difference model explained above, which uses the rectilinear grid, is not convenient to extend to the case of irregular and movable beds and integrate with sediment transport calculations. Therefore, as presented in Chapter 4, a new 3-D numerical model was developed to simulate dam-break flows on irregular fixed beds. The model solves the RANS equations using an explicit finite-volume method based on collocated mesh that fits on irregular beds. The velocity and pressure coupling is achieved using the PISO algorithm and the Rhie and Chow's momentum interpolation. The Smagorinsky turbulence model is used to estimate the eddy viscosity. At the free surface boundary the VOF technique is adopted to trace the changes of water surface due to strong unsteady behavior of dam-break flows. An explicit version of the CICSAM algorithm is proposed and used to solve the VOF advection equation since it is applicable to arbitrary meshes.

The newly developed 3-D finite-volume hydrodynamic model was tested successfully using several experimental dam-break flows on flat and irregular beds. The model was tested first by small-scale dam-break flows over flat beds to investigate the accuracy of the model to simulate the initial stages of dam-break flows. The second test was the propagation of breaking solitary wave over sloping beach using a boundary-fitted mesh. The model was also tested using the dam-break flows on irregular beds consisted of trapezoidal and triangular steps. Finally the developed model was tested using a dam-break flow over an isolated rectangular block and a partial dam-break flow. The comparisons between measured and calculated water levels, pressures and velocities, which were in good agreement, indicated the successful application of the proposed explicit versions of PISO and CICSAM methods. These solution methods are originally implicit approaches.

To extend the finite-volume model to a dam-break flow model applicable on movable beds due to sediment transport, the bed changes caused by erosion and sediment deposition must be calculated. Therefore, the final achievement of this dissertation was developing a sediment transport model integrated with the above 3-D finite-volume hydrodynamic model, as presented in Chapter 5. The sediment transport model solves the governing equations of suspended-load and bed-load transport separately based on the flow properties calculated by the hydrodynamic model. Bed shear stress and critical shear stress were modified for rapidly-varying flows and bed with steep slopes. The calculated sediment concentration and transport rate are used to estimate the bed changes. Since the time evolution of bed topography affects the hydrodynamic calculations, the model uses a moving grid technique to update the computational grid to fit on the calculated bed topography at every time step. The grid vertical velocity generated by the moving mesh is added to the convective terms of the governing equations. Furthermore, any volume change of computational cells due to updating the grid is taken into consideration when the temporal terms of the hydrodynamic and sediment transport equations are discretized.

The integrated 3-D finite-volume flow and sediment transport model was further tested by several experimental dam-break flows on movable beds and the results were discussed in Chapter 5. In the first two cases the model was tested using small-scale dam-break flows on erodible beds covered by sand and PVC pellets. The model was tested using additional two experiments of dam-break flows on movable beds with strong 3-D features. The 3-D cases included a dam-break flow over movable bed in an abruptly widening channel and a partial dam-break flow over movable bed. The comparisons between the measured and calculated bed and water surface profiles revealed the validity of the developed model to simulate dam-break flows on movable beds.

The successful application of the model to experimental dam-break flows on movable beds validated the innovative approach used by this dissertation to divide the computational domain into bed-load and suspended-load zones. The bed-load transport equation was solved in the first layer of the computational mesh whereas the suspended-load was solved in the computational domain above the first layer. Moreover, the proposed moving grid technique to track the bed surface boundary changes showed a successful implementation along with the VOF technique, which tracks the water surface boundary changes.

In conclusion, the present dissertation is a pilot study on 3-D numerical modeling of dam-break flows over movable beds. The successful application of the model to the experimental cases promises the future achievements in 3-D numerical modeling of rapidly-varying flows on movable beds in field cases.

6.2 Future research

The future research related to this dissertation can be suggested as follows:

1) The accuracy and performance of the hydrodynamic model developed in this dissertation can be investigated by adopting other existing solution methods. Firstly, it is suggested to adopt other classes of turbulence models instead of the Smagorinsky model. Secondly, higher-order time and space discretization methods might be used to increase the model accuracy. Thirdly, instead of the PISO method, other pressure-velocity coupling methods can be used.
2) In rivers, streams, lakes, reservoirs, and coastal waters, the bed may be made of multiple-sized sediments, whereas the developed sediment transport model in this study deals with single-sized sediment particles. By extending the developed model to a multiple-sized sediment transport model, the effects of bed-material sorting, mixing layer thickness, presence of armor layer, and hiding and exposure mechanism on sediment transport under dam-break flows can be studied.

3) The developed sediment transport model deals only with non-cohesive sediment particles, whereas fine cohesive sediments, such as clay and fine silt, exist in rivers, streams, lakes, reservoirs, estuaries and coastal waters. Therefore, the developed model can be extended to simulate non-cohesive/cohesive sediment transport under dam-break flows.

4) In real dam-break flow events, it is crucial to provide accurate and fast simulation to meet the time constraints in emergency situations. Since the presented models in this dissertation have been developed based on serial programming in single-core CPU without any parallelization, simulation of a large-scale dam-break flow can be computationally expensive. Therefore, another future research related to this dissertation is to reduce the computational expenses by taking advantages of parallel programming in GPU or OpenMP programming in multi-core processors.

BIBLIOGRAPHY

Altinakar, M. S., McGrath, M. Z., Ramalingam, V. P., Singh, J., Ding, Y., and Inman, M. (2012). “Advances in 2D flood modeling and mapping technology fo dam and levee safety.” *Proceedings of the 10th International Congress on Advances in Civil Engineering*.

American Society of Civil Engineers. (2013). “2013 report card for America's infrastructure.”

Aulisa, E., Manservisi, S., Scardovelli, R., and Zaleski, S. (2007). “Interface reconstruction with least-squares fit and split advection in three-dimensional Cartesian geometry.” *Journal of Computational Physics*, Vol. 225(2), pp 2301-2319.

Bagnold, R. A. (1954). “Experiments on a gravity-free dispersion of large solid spheres in a Newtonian fluid under shear.” *Proceedings of the Royal Society A*, Vol. 225(1160), pp 49-63.

Bell, R. G. and Sutherland, A. J. (1983). “Non-equilibrium bed load transport by steady flows.” *Journal of Hydraulic Engineering*, Vol. 109(3), pp 351-367.

Bellos, C. V. and Sakkas, J. G. (1987). “1-D dam-break flood-wave propagation on dry bed.” *Journal of Hydraulic Engineering*, Vol. 113(12), pp 1510-1524.

Cao, Z., Pender, G., Wallis, S., and Carling, P. (2004). “Computational Dam-Break Hydraulics over Erodible Sediment Bed.” *Journal of Hydraulic Engineering*, Vol. 130(7), pp 689-703.

Capart, H., and Young D. L. (1998). “Formation of jump by the dam-break wave over a granular bed.” *Journal of Fluid Mechanics*, Vol. 372, pp 165-187.

Capart, H., and Young D. L. (2002). “Two-layer shallow water computations of torrential flows.” *Proceedings of River flow*, Vol. 2, pp 1003-1012.

Chorin, A. J. (1968). “Numerical solution of the Navier-Stokes equations.” *Mathematics of Computation*, Vol. 22(104), 745–762.

Crumpton, P. I., Moiner, P., and Giles, M. B. (1997). “An unstructured algorithm for High Reynolds number flows on highly-stretched grids.” *Proceedings of 10th International Conference on Numerical Methods in Laminar and Turbulent Flow*, Swansea, Wales.

Fekken, G. (2004). “Numerical simulation of free-surface flow with moving rigid bodies.” *Ph.D. thesis*, University of Groningen, Netherlands.

Ferrari, A., Fraccarollo, L., Dumbser, M., Toro, E.F., and Armanini, A. (2010). “Three-dimensional flow evolution after a dam break.” *Journal of Fluid Mechanics*, Vol. 663, pp 456-477.

Fraccarollo, L. and Toro, E. F. (1995). “Experimental and numerical assessment of the shallow water model for two-dimensional dam-break type problems.” *Journal of Hydraulic Research*, Vol. 33(6), pp 843-864.

Fraccarollo, L. and Capart, H. (2002). “Riemann wave description of erosional dam break flows.” *Journal of Fluid Mechanics*, Vol. 461, pp 183-228.

Gingold, R. A. and Monaghan, J. J. (1977). “Smoothed particle hydrodynamics: Theory and application to non-spherical stars.” *Monthly Notices of the Royal Astronomical Society*, Vol. 181, pp 375-389.

Gleick, P. H. (1993). “Water in crisis: A guide to the world’s freshwater resources.” Oxford University Press, pp 13, Table 2.1.

Goutiere, L., Soares-Frazao, S., and Zech, Y. (2011). “Dam-break flow on mobile bed in abruptly widening channel: experimental data.” *Journal of Hydraulic Research*, Vol. 49(3), pp 367-371.

Harlow, F. H. and Welch, J. E. (1965). “Numerical calculation of time-dependent viscous incompressible flow of fluid with free surface.” *Physics of Fluids*, Vol. 8(12), pp 2182-2189.

Haselbacher, A. and Blazek, J. (2000). “Accurate and efficient discretization of Navier Stokes equations on mixed grids.” *American Institute of Aeronautics and Astronautics Journal*, Vol. 38(11), pp 2094-2102.

Hicks, F. E., Steffler, P. M., and Yasmin, N. (1997). “One-dimensional dam-break solutions for variable width channels.” *Journal of Hydraulic Engineering*, Vol. 123(5), pp 464-468.

Hirt, C. W. and Nichols, B. D. (1981). “Volume of fluid (VOF) method for the dynamics of free boundaries.” *Journal of Computational Physics*, Vol. 39(1), pp 201-225.

IAHR working group for dam-break flows over mobile beds. (2012). “Dam-break flows over mobile beds: experiments and benchmark tests for numerical models.” *Journal of Hydraulic Research*, Vol. 50(4), pp 364-375.

Interagency Committee on Dam Safety. (2004). “Federal guidelines for dam safety: hazard potential classification system for dams.” FEMA.

Issa, R. I. (1986). “Solution of the implicitly discretized fluid flow equations by operator spliting.” *Journal of Computational Physics*, Vol. 62(1), pp 40-65.

Jang, D. S., Jetli, R., and Acharya, S. (1986). “Comparison of PISO, SIMPLER, and SIMPLEC algorithms for the treatment of the pressure-velocity coupling in steady flow problems.” *Numerical Heat Transfer*, Vol. 10(3), pp 209-228.

Jasak, H. (1996). “Error analysis and estimation for the Finite Volume method with applications to fluid flows.” *Ph.D. thesis*. University of London, UK.

Jha, A. K., Akiyama, J., and Ura, M. (1995). “First- and second-order flux difference splitting schemes for dam-break problem.” *Journal of Hydraulic Engineering*, Vol. 121(12), 877-884.

Kao, H-M. and Chang, T-J. (2012). “Numerical modeling of dam-break-induced flood and inundation using smoothed particle hydrodynamics.” *Journal of Hydrology*. Vol. 448-449, pp 232-244.

Katopodes, N. D. and Wu, C. (1986). “Explicit computation of discontinuous channel flow.” *Journal of Hydraulic Engineering*, Vol. 112(6), pp 456-474.

Kleefsman, K. M. T., Fekken, G., Veldman, A. E. P., Iwanowski, B. and Buchner, B. (2005). “A volume-of-fluid based simulation method for wave impact problems.” *Journal of Computational Physics*, Vol. 206(1), pp 363-393.

Kocaman, S. (2007). “Experimental and theoretical investigation of dam-break problem.” *Ph.D. thesis*. University of Cukurova, Adana, Turkey [in Turkish].

Kothe, D. B., Rider, W. J., Mosso, S. J., Brock, J. S., and Hochstein, J. I. (1996). "Volume tracking of interfaces having surface tension in two and three dimensions." Technical report AIAA 96-0859 , Los Alamos, NM.

Kuiry, S. N., Pramanik, K. and Sen, D. (2008). "Finite volume model for shallow water equations with improved treatment of source terms." *Journal of Hydraulic Engineering*, Vol. 134(2), pp 231-242.

Lauber, G. and Hager, W. H. (1998). "Experiments to dam-break wave: horizontal channel." *Journal of Hydraulic Research*, Vol. 36(3), pp 291-307.

Li, Y. and Raichlen, F. (2002). "Non-breaking and breaking solitary wave run-up." *Journal of fluid mechanics*, Vol. 456, pp 295-318.

Lin, P., Wu, Y., Bai, J., and Lin Q. (2011). "A Numerical Study of Dam-Break Flow and Sediment Transport from a Quake Lake." *Journal of Earthquake and Tsunami*, Vol. 5(5), pp 401-428.

Lucy, L. B. (1977). "A numerical approach to the testing of the fission hypothesis." *Astronomical Journal*, Vol. 82, pp 1013-1024.

Mahdavi, A. and Talebbeydokhti, N. (2009). "Modeling of non-breaking and breaking solitary waves run-up using FORCE-MUSCL scheme." *Journal of Hydraulic Research*, Vol. 47(4), pp 476-485.

Marsooli, R., Zhang, M., and Wu, W. (2011). "Vertical and horizontal two-dimensional numerical modeling of dam-break flow over fixed beds." *Proceedings of World Environmental and Water Resources Congress*, ASCE, Palm Springs, CA., U.S.A.

Mohapatra, P. K., Eswaran, V., and Bhallamudi, S. M. (1999). “Two-dimensional analysis of dam-break flow in vertical plane.” *Journal Hydraulic Engineering*, Vol. 125(2), pp 183-192.

Muzaferija, S. and Peric, M. (1998). “Computation of free-surface flows using interface tracking and interface-capturing methods.” in O. Mahrenholtz and M. Markiewicz (eds.), Nonlinear water wave interaction, Computational Mechanics Publications, Southampton, UK., pp 59-100.

Muzaferija, S., Peric, M., Sames, P., and Schellin, P. (1998). “A two-fluid Navier Stokes solver to simulate water entry.” *Twenty-Second Symposium on Naval Hydrodynamics*, Washington, DC, pp. 638–649.

Nakagawa, H. and Tsujimoto, T. (1980). “Sand bed instability due to bed load motion.” *Journal of the Hydraulics Division*, Vol. 106(12), pp 2029-2051.

Nichols, B. D. and Hirt, C. W. (1971). “Improved free surface boundary conditions for numerical incompressible-flow calculations.” *Journal of Computational Physics*, Vol. 8(3), pp 434-448.

Nichols, B. D., Hirt, C. W., and Hotchkiss, R. S. (1980). “SOLA-VOF: A solution algorithm for transient fluid flow with multiple free boundaries.” Los Alamos Scientific Laboratory Report, LA-8355, Los Alamos, NM.

Noh, W. F., and Woodward, P. (1976). “SLIC (Simple Line Interface Calculation).” *Proceedings of the Fifth International Conference on Numerical Methods in Fluid Dynamics*, Vol. 59, pp 330-340.

Oertel, M. and Bung, D. B. (2012). “Initial stage of two-dimensional dam-break waves: laboratory versus VOF.” *Journal of Hydraulic Research*, Vol. 50(1), pp 89-97.

Osher, S. and Sethian, J.A. (1988). “Fronts propagation with curvature-dependent speed: algorithms based on Hamilton-Jacobi formulation.” *Journal of Computational Physics*, Vol. 79(1), pp 12-49.

Ozmen-Cagatay, H. and Kocaman, S. (2010). “Dam-break flows during initial stage using SWE and RANS approaches.” *Journal of Hydraulic Research*, Vol. 48(5), pp 603-611.

Ozmen-Cagatay, H. and Kocaman, S. (2011). “Dam-break flow in the presence of obstacle: experiment and CFD simulation.” *Engineering Applications of Computational Fluid Mechanics*, 5(4), 541-552.

Patankar, S. V. (1980). “Numerical Heat Transfer and Fluid Flow.” Hemisphere Publishing Corporation, Taylor & Francis Group, New York, NY.

Patankar, S. V. and Spalding, D. B. (1972). “A calculation procedure for heat, mass and momentum transfer in three-dimensional parabolic flows.” *International Journal of Heat and Mass Transfer*, Vol. 15(10), pp 1787-1806.

Peskin, C. S. (1972). “Flow patterns around heart valves: a numerical method.” *Journal of Computational Physics*, Vol. 10(2), pp 252-271.

Peskin, C. S. (1977). “Numerical analysis of blood flow in the heart.” *Journal of Computational Physics*, Vol. 25(3), pp 220-252.

Phillips, B. C. and Sutherland, A. J. (1989). “Spatial lag effects in bed load sediment transport.” *Journal of Hydraulic Research*, Vol. 27(1), pp 115-133.

Pilliod Jr., J. E. and Puckett, E. G. (2004). “Second-order accurate volume-of-fluid algorithms for tracking material interfaces.” *Journal of Computational Physics*, Vol. 199(2), pp 465-502.

Que, Y-T. and Xu, K. (2006). “The numerical study of roll-waves in inclined open channels and solitary wave run-up.” *International Journal for numerical methods in fluids*, Vol. 50(9), pp 1003-1027.

Rajar, R. (1978). “Mathematical simulation of dam-break flow.” *Journal of the Hydraulics Division*, Vol. 104(7), pp 1011-1026.

Richardson, J. F., and Zaki, W. N. (1954). “Sedimentation and fluidization; part I.” *Transactions of the Institution of Chemical Engineers*, Vol. 32, pp 35-53.

Ritter, A. (1892). “Die Fortpflanzung der Wasserwellen.” *Vereine Deutscher Ingenieure Zeitswchrift*, 36(2), 33, pp 947-954 (in German).

Rhie, C. M., and Chow, W. L. (1983). “Numerical study of the turbulent flow past an isolated airfoil with trailing-edge separation.” *American Institute of Aeronautics and Astronautics Journal*, Vol. 21(11), pp 1525–1532.

Savary, C., and Zech, Y. (2006). “Can a two-layer morphological model compete with common sediment transport formulae?” *Proceedings of River Flow*, pp 825–832.

Savic, Lj., and Holly Jr, F. M. (1993). “Dambreak flood waves computed by modified Godunov method.” *Journal of Hydraulic Research*, Vol. 31(2), pp 187–204.

Scardovelli, R. and Zaleski, S. (2000). "Analytical relations connecting linear interfaces and volume fractions in rectangular grids." *Journal of Computational Physics*, Vol. 164(1), pp 228-237.

Smagorinsky, J. (1963). "General circulation experiments with the primitive equations; I. the basic experiment." *Monthly Weather Review*, Vol. 91(3), pp 99-164.

Spinewine, B. (2005). "Two-layer flow behavior and the effects of granular dilatancy in dam-break induced sheet-flow" *PhD Thesis*, University Catholique de Louvain-la-Neuve, Belgium.

Spinewine, B., and Zech, Y. (2007). "Small-scale laboratory dam-break waves on movable beds." *Journal of Hydraulic Research*, Vol. 45, pp 73-86.

Stansby, P. K., Chegini, A., and Barnes, T. C. D. (1998). "The initial stages of dam-break flow." *Journal of Fluid Mechanics*, Vol. 374, pp 407-424.

Synolakis, C.E. (1986). "The Run-up of Long Waves." *PhD Thesis*, California Institute of Technology, USA.

Synolakis, C. E. (1987). "The Run-up of solitary waves." *Journal of fluid mechanics*, Vol. 185, pp 523-545.

Torey, M. D., Cloutman, L. D., Mjolsness, R.C., and Hirt, C. W. (1985). "NASA-VOF2D: A computer program for incompressible flows with free surfaces." Los Alamos National Laboratory Report, LA-10612-MS.

Ubbink, O. (1997). "Numerical prediction of two fluid systems with sharp interfaces." *Ph.D. Thesis*, University of London, UK.

Ubbink, O. and Issa, R.I. (1999). “A method for capturing sharp fluid interfaces on arbitrary meshes.” *Journal of Computational Physics*, Vol. 153(1), pp 26-50.

Van Doormaal, J. P. and Raithby, G. D. (1984). “Enhancements of the SIMPLE method for predicting incompressible fluid flows.” *Numerical Heat Transfer*, Vol. 7(2), pp 147-163.

Van Rijn, L. C. (1981). “Entrainment of fine sediment particles; development of concentration profiles in a steady, uniform flow without initial sediment load.” Rep. No M1531, Part II, Delft Hydraulic Lab., Delft, The Netherlands.

Van Rijn, L. C. (1984a). “Sediment transport. Part I: Bed load transport.” *Journal of Hydraulic Engineering*, Vol. 110(10), pp 1431-1456.

Van Rijn, L. C. (1984b). “Sediment transport. Part II: suspended load transport.” *Journal of Hydraulic Engineering*, Vol. 110(11), pp 1613-1641.

Wang, J. S., Ni, H. G., and He, Y. S. (2000). “Finite-difference TVD scheme for computation of dam-break problems.” *Journal of Hydraulic Engineering*, Vol. 126(4), pp 253-262.

Weiss, J. M., Maruszewski, J. P., and Smith, W. A. (1999). “Implicit solution of preconditioned Navier-Stokes equations using algebraic multigrid.” *American Institute of Aeronautics and Astronautics Journal*, Vol. 37(1), pp 29-36.

Weymouth, G. D. and Yue, D. K. P. (2010). “Conservative volume-of-fluid method for free surface simulations on Cartesian-grids.” *Journal of Computational Physics*, Vol. 229(8), pp 2853-2865.

Wu, W. (2007). “Computational River Dynamics.”, Taylor & Francis, London, UK.

Wu, W. and Wang, S. S. Y. (2006). “Formulas for sediment porosity and settling velocity.” *Journal of Hydraulic Engineering*, Vol. 132(8), pp 858-862.

Wu, W. and Wang, S. S. Y. (2007). “One-Dimensional Modeling of Dam-Break Flow over Movable Beds.” *Journal of Hydraulic Engineering*, Vol. 133(1), pp 48-58.

Wu, W., Rodi, W., and Wenka, T. (2000a). “3D numerical modeling of flow and sediment transport in open channels.” *Journal of Hydraulic Engineering*, Vol. 126(1), pp 4-15.

Wu, W., Wang, S. S. Y., and Jia, Y. (2000b). “Nonuniform sediment transport in alluvial rivers.” *Journal of Hydraulic Research*, Vol. 38(6), pp 427-434.

Wu, W., Marsooli, R., and He, Z. (2012). “A depth-averaged two-dimensional model of unsteady flow and sediment transport due to non-cohesive embankment break/breaching.” *Journal of the Hydraulic Engineering*, Vol. 138(6), pp 503-516.

Xia, J., Lin. B., Falconer, A., and Wang, G. (2010). “Modeling dam-break flows over mobile beds using a 2D coupled approach.” *Advances in Water Resources*, Vol. 33(2), pp 171-183.

Yang, C., Lin. B., Jiang, C., and Liu, Y. (2010). “Predicting near-field dam-break flow and impact force using a 3D model.” *Journal of Hydraulic Research*, Vol. 48(6), pp 784-792.

Yin, R. and Chow, W. K. (2003). “Comparison of four algorithms for solving pressure-velocity linked equations in simulating atrium fire.” *International Journal on Architectural Science*, Vol. 4(1), pp 24-35.

Ying, X. and Wang, S. S. Y. (2008). “Improved implementation of the HLL approximate Riemann solver for one-dimensional open channel flows.” *Journal of Hydraulic Research*, Vol. 46(1), pp 21-34.

Ying, X., Khan, A. A., and Wang, S. S. Y. (2004). “Upwind conservative scheme for the Saint Venant equations.” *Journal of Hydraulic Engineering*, Vol. 130(10), pp 977-987.

Youngs, D. L. (1982). “Time-Dependent multi-material flow with large fluid distortion.” Numerical Methods for Fluid Dynamics, K.W. Morton and M.J. Baines (eds.), New York Academic Press, pp 273-285.

Youngs, D. L. (1984). “An Interface Tracking Method for a 3D Eulerian Hydrodynamics Code.” Technical Report 44/92/35, AWRE.

Zhang, S., Duan, J., and Strelkoff, T. (2013). “Grain-scale nonequilibrium sediment-transport model for unsteady flow.” *Journal of Hydraulic Engineering*, Vol. 139(1), pp 22-36.

Zech, Y., Soarez-Frazao, S., Spinewine, B., and Le Grelle, N. (2008). “Dam-break induced sediment movement: experimental approaches and numerical modeling.” *Journal of Hydraulic Research*, Vol. 46(2), pp 176-190.

VITA

Reza Marsooli

Email: rezamarsooli@gmail.com

EDUCATION

- Ph.D. in Computational Hydroscience.
  - National Center for Computational Hydroscience and Engineering (NCCHE), The University of Mississippi, MS, USA.
  - 2009-2013.
  - Dissertation title: 3-D numerical model of dam-break waves over movable beds.
  - Supervisor: Weiming Wu, Research Associate Professor.
- M.S. in Civil-Water Engineering.
  - University of Tabriz, Tabriz, Iran.
  - 2005-2007.
  - Thesis title: Application of river sediment specific discharge in analysis of dam reservoirs sedimentation.
  - Supervisor: Mohammad T. Alami, Associate Professor.
- B.S. in Civil Engineering.
  - Central Tehran Branch, Azad University, Tehran, Iran.
  - 2000-2004

AWARDS

- Outstanding Research Assistant Award, 2012, National Center for Compuatinal Hydraoscience and Engineering (NCCHE), The University of Mississippi, MS, USA.
- Research Assistantship, Fall 2009 to Spring 2013, National Center for Compuatinal Hydraoscience and Engineering (NCCHE), The University of Mississippi, MS, USA.
- Graduate Research Assistantship provided by the Graduate School, Summer 2012, The University of Mississippi, MS, USA.
- Dissertation Fellowship provided by the Graduate School, Spring 2013, The University of Mississippi, MS, USA.
- Senator of the Engineering Sciences Department, Graduate Student Council, 2011-2012, The University of Mississippi, MS, USA.
- Senator of the Engineering Sciences Department, Graduate Student Council, 2010-2011, The University of Mississippi, MS, USA.
- Best logo design for the Graduate Student Council, 2011, The University of Mississippi, MS, USA.
- Reviewer of several papers for the Journal of Hydraulic Engineering, Natural Hazards, Estauries and Coasts, etc.

RESEARCH AND TEACHING EXPERIENCE

- Research Assistant, National Center for Computational Hydroscience and Engineering (NCCHE), The University of Mississippi, USA, 2009 to 2013, developing numerical models to simulate dam-break flows, sediment transport, vegetated channels, etc. (for example: Phase II of SERRI Project No. 80037: Investigation of Surge and Wave Reduction by Vegetation, Interaction of Hydrodynamics, Vegetation and Soil. Summer 2012, The University of Mississippi, MS, USA.)
- Research Hydraulic Engineer, Sazabandish Consulting Engineering Corporation, Tehran, Iran, 2006-2009 (research on water distribution networks and sewer systems and teaching hydraulic design of water and sewer systems using WaterGEMS, SewerCAD, and Spreadsheet).

FIELDS OF INTERESTS

- Numerical Modeling of Surface Flows and Sediment Transport.
- Numerical Modeling of Dam/Levee Break and Breach Flows over Fixed and Movable Beds.
- Numerical Modeling of Tsunami, Storm Surge, Wave, and Coastal Flooding.
- Sediment Transport and River Hydraulics.
- Ocean and Coastal Engineering.
- Groundwater Modeling.
- River, Stream Bank, and Beach Restoration

- Parallel Programming on CPU and GPU.
- Artificial Neural Networks (ANN).
- Water and Sewer Systems.

TEACHING INTERESTS

- Numerical Modeling of Surface Flows.
- Sediment Transport Hydraulics.
- Computational Fluid Dynamics.
- Open Channel Flows.
- Fluid Mechanics.
- Hydrology.

PUBLICATIONS

- Book chapters
    - Reza Marsooli and Weiming Wu, 2012, “3-D Finite-Difference Dam-Break Wave Model Based on Volume-of-Fluid Surface Tracking Method,” *Wave Propagation*, Academy Publish, Cheyenne, WY, USA, in press.
    - Weiming Wu, Zhiguo He, Qianru Lin, Alejandro Sanchez, and Reza Marsooli, 2013, “Non-Equilibrium Sediment Transport Modeling — Extensions and Applications,” *Sediment Transport: Monitoring, Modeling and Management*, Abdul Khan and Weiming Wu (eds.), Nova Science Publishers, NY, USA.
- Journal papers
    - Reza Marsooli and Weiming Wu, 2013, “3-D Finite-Volume Model of Dam-Break Flow over Uneven Beds Based on VOF Method”, *Journal of Hydraulic Engineering*, Under Review.
    - Reza Marsooli and Weiming Wu, 2013, “3-D Finite-Volume Model of Dam-Break Flow on Movable Beds”, *Journal of Hydraulic Engineering*, Under Review.
    - Weiming Wu and Reza Marsooli, 2012, “A Depth-Averaged 2-D Shallow Water Model for Breaking and Non-breaking Long Waves Affected by Rigid Vegetation”, *Journal of Hydraulic Research*, 50(6), 558-575.
    - Weiming Wu, Reza Marsooli, and Zhiguo He, 2012, “Depth-Averaged Two-Dimensional Model of Unsteady Flow and Sediment Transport due to Noncohesive Embankment Break/Breaching”, *Journal of Hydraulic Engineering*, 138(6), 503-516.

- IAHR Working Group for Dam-Break Flows over Mobile beds, 2012, “Dam-Break flows over mobile beds: experiments and benchmark tests for numerical models”, *Journal of Hydraulic Researh*, 50(4), 364-375.
- Chih Ted Yang and Reza Marsooli, 2010, “Recovery factor for non-equilibrium sedimentation processes”, *Journal of Hydraulic Research*, 48(3), 409–413.
- Chih Ted Yang, Reza Marsooli, and Mohammad T. Alami, 2009,“Evaluation of Total Load Sediment Transport Formulas using ANN”, *International Journal of Sediment Research*, 24(3), 274-286

- Conference papers
  - Reza Marsooli and Weiming Wu, 2013, “3-D Finite-Volume Simulation of Dam-Break flows on Movable beds”, *EWRI Congress*, Cincinnati, OH, USA, May 19-23.
  - Reza Marsooli and Weiming Wu, 2012, “Three-Dimensional Numerical Simulation of Dam Break Flow Based on a Volume of Fluid Approach”, *Third International Symposium on Shallow Flows*, Iowa City, IA, USA, June 4-6.
  - Reza Marsooli and Weiming Wu, 2011, “Simulation of Dam Break Waves over Fixed Beds Using a Vertical 2D Numerical Model Based on VOF Method”, *MAES Conference*, Memphis, TN, USA, May 3.
  - Reza Marsooli, Mingliang Zhang, and Weiming Wu, 2011, “Vertical and Horizontal Two-Dimensional Numerical Modeling of Dam-Break Flow over Fix Beds”, *EWRI Congress*, Palm Springs, CA, USA, May 22-26.
  - Weiming Wu and Reza Marsooli, 2010, Benchmark (Blind) Test of Wu’s depth-averaged 2D model for dam-break flow over movable bed. NSF-PIRE 2010 Workshop ‘Dam-break flow on mobile bed’, private communication at http://www.uclouvain.be/ 373040.html, 19 p.
  - Amir H. Asadiany Yekta, Reza Marsooli, and Foad Soltani, 2010, “Suspended sediment estimation of Ekbatan reservoir sub basin using Artificial Neuro-Fuzzy Inference Systems (ANFIS), Artificial Neural Networks (ANN), and sediment rating curves“ *International Conference on Fluvial Hydraulics*, Braunschweig, Germany, September 8-10, 807-813.
  - Amir H. Asadiany Yekta, Reza Marsooli, and Mohammad T. Alami, 2008, “Prediction of reservoir sedimentation with an artificial neural network trained using GSTARS3 mathematical model (Case study: Kardeh Dam)”, *International Conference on Fluvial Hydraulics*, Cesme, Izmir, Tutrkey, September 3-5, Vol. 2, 1181-1190.
  - Reza Marsooli and Mostafa Aliakbari, 2008, “Camparison and optimum choise of sewer networks in small societies”, *4th National Congress on Civil Engineering*, University of Tehran, Tehran, Iran, May 6-8, Paper code: 77.
  - Mohammad T. Alami, Reza Marsooli, and Amir H. Asadiany Yekta, 2008, “Application and assessment of GSTARS3 in reservoir sedimentation

simulation”, *4th National Congress on Civil Engineering*, University of Tehran, Tehran, Iran, May 6-8, Paper code: 25.